

THESIS FOR THE DEGREE OF DOCTOR OF PHILOSOPHY

Low-temperature carburizing/nitriding of austenitic stainless steels

— Influence of alloy composition on microstructure and properties

Giulio Maistro



Department of Industrial and Materials Science
CHALMERS UNIVERSITY OF TECHNOLOGY
Gothenburg, Sweden 2018

Low-temperature carburizing/nitriding of austenitic stainless steels
— Influence of alloy composition on microstructure and properties
Giulio Maistro

© Giulio Maistro, 2018.

ISBN 978-91-7597-679-2

Series number: 4360

In the series Doktorsavhandlingar vid Chalmers tekniska högskola.

Ny serie (ISSN 0346-718X)

Department of Industrial and Materials Science
Chalmers University of Technology
SE-412 96 Gothenburg
Sweden
Telephone + 46 (0)31-772 1000

Printed by Chalmers Reproservice
Göteborg, Sweden 2018

Low-temperature carburizing/nitriding of austenitic stainless steels – Influence of alloy composition on microstructure and properties

Giulio Maistro

Department of Industrial and Materials Science
Chalmers University of Technology

Abstract

Austenitic stainless steels are among the most used materials in applications where corrosion resistance is important, as the food, pharmaceutical, chemical, oil and gas industries. However, low hardness and poor tribological properties is often an obstacle for their applicability. Conventional surface hardening techniques, such as high-temperature carburizing ($T > 850^{\circ}\text{C}$) and nitriding ($T > 550^{\circ}\text{C}$) are not suitable for these alloys. Rapid precipitation of chromium-rich carbides/nitrides at the grain boundaries would in such cases induce chromium depletion in the alloy and compromise the corrosion resistance. Since the middle of the '80s, low-temperature thermochemical treatments have been developed for surface hardening of austenitic stainless steels, including gas carburizing and plasma nitriding. These processes can induce formation of a precipitate-free interstitially supersaturated metastable expanded austenite, also known as S-phase, having superior hardness and improved wear resistance, while maintaining corrosion resistance.

The aim of this thesis is to increase the understanding of the microstructure-properties relationship of the surface modifications obtained by treating austenitic stainless steels with low-temperature carburizing and nitriding processes. In particular, the research focus is on the influence of alloy composition and surface finish on the microstructural evolution, phase constituents, thermal stability, strain, hardening, wear and corrosion resistance of the expanded austenite layers. The investigations were carried out by means of different analytical techniques, such as XPS, AES, XRD, SEM, GDOES and EBSD among others.

It has been found that alloy composition and surface finish have a paramount influence on the microstructural characteristics and properties of the expanded austenite layers. High molybdenum content and plastic deformation enhances interstitial diffusion and supersaturation, while nickel decreases both. On the other hand, nickel prevents the formation of detrimental nitride/carbide-containing compound layers, enhances the thermal stability of the alloys and directs the expanded austenite decomposition towards a discontinuous route. During thermochemical treatments, precipitates tend to form preferentially at the surface, in correspondence of slip-planes or ferritic/martensitic regions. A hard, expanded austenite layer prevents severe adhesive and abrasive wear during dry sliding tests, improving wear resistance at low load. N-stabilised expanded austenite potentially possesses stronger hardening effects, but is more brittle. The strong interaction between chromium and carbon in expanded austenite alters the iron/chromium ratio within the passive film, making the surface more noble and conductive. When expanded austenite is thermally decomposed, hardening and corrosion resistance are at least partially compromised.

Keywords: Austenitic stainless steel, expanded austenite, S-phase, low-temperature carburizing, plasma nitriding, surface engineering, surface analysis, XPS, XRD, SEM, EBSD, GDOES, thermal stability, tribology, corrosion

Preface

This Doctoral thesis is based on the work performed at the Department of Industrial and Materials Science (previously Materials and Manufacturing Technology), Chalmers University of Technology, from January 2013 to December 2017. Part of the activities in Paper III and paper VI were conducted during a study visit (February-May 2016) at the “Centro de Investigacion en Materiales Avanzados” (CIMAV) in Monterrey, Mexico.

The project has been carried out under the supervision of Associate Professor Yu Cao and Professor Lars Nyborg.

This thesis consists of an introductory part followed by the appended papers:

Paper I: Multi-technique characterization of low-temperature plasma nitrided austenitic AISI 304L and 904L stainless steel

Y. Cao, G. Maistro, M. Norell, S. A. Pérez-García and L. Nyborg
Surface and Interface Analysis, **2014**, 46 (10-11) pp. 856-860

Paper II: Microstructural characterization and layer stability of low-temperature carburized AISI 304L and AISI 904L austenitic stainless steel

G. Maistro, L. Nyborg, S. Vezzù and Y. Cao
La Metallurgia Italiana, **2015**, 11-12 pp. 21-30

Paper III: Thermal decomposition of N-expanded austenite in 304L and 904L steels

G. Maistro, S. A. Pérez-García, M. Norell, L. Nyborg and Y. Cao
Surface Engineering, **2017**, 33 (4) pp. 319-326

Paper IV: Understanding the microstructure-properties relationship of low-temperature carburized austenitic stainless steels through EBSD analysis

G. Maistro, C. Oikonomou, L. Rogström, L. Nyborg and Y. Cao
Surface & Coatings Technology, **2017**, 332 pp. 141-151

Paper V: Low-temperature carburized high-alloyed austenitic stainless steels in PEMFC cathodic environment

G. Maistro, S. Kante, L. Nyborg and Y. Cao
Submitted for publication in International Journal of Hydrogen Energy

Paper VI: Tribological behaviour of low-temperature carburised austenitic stainless steels

G. Maistro, M. Esneider, S.A. Pérez-García, L. Nyborg and Y. Cao
Submitted for publication in Wear

Paper VII: Surface carbides in low-temperature carburized austenitic stainless steels

G. Maistro, S. Kante, Y. Yao, U. Klement, L. Nyborg, Y. Cao
In manuscript

Contribution to the appended papers

- Paper I The author participated in conducting the experimental work, writing the paper and participated in the corrections.
- Paper II The author planned and executed most of the experimental work as well as data analysis. GDOES measurements were performed by Dr. Simone Vezzú. The author wrote the paper.
- Paper III The author planned and executed the experimental work in cooperation with the co-authors. The author performed the data analysis and wrote the paper.
- Paper IV The author planned and executed the work in cooperation with the co-authors. Experimental work was conducted in cooperation with Dr. C. Oikonomou. Nano-indentation measurements were performed by Dr. L. Rogström. The author performed the data analysis and wrote the paper.
- Paper V The author participated in the planning, execution of the experimental work and data analysis in cooperation with the co-authors, in particular with MSc. Stefan Kante. The author wrote the paper.
- Paper VI The author planned and executed the experimental work in cooperation with the co-authors. In particular, the pin-on-disk testing was performed by M. Esneider. The author performed the data analysis and wrote the paper.
- Paper VII The planning, experimental work and data analysis was performed by the author in cooperation with the co-authors. In particular, determination of orientation relationships by EBSD was performed by Dr. Y. Yao. The author wrote the paper.

List of acronyms and abbreviations

Ann: annealed

BCC: body-centred cubic

EBSD: electron backscattered diffraction

EDS: energy dispersed x-ray spectroscopy

FCC: face-centred cubic

GDOES: glow-discharge optical emission spectroscopy

GIXRD: grazing incidence x-ray diffraction

LOM: light optical microscopy

LTC: low-temperature carburizing

LTN: low-temperature nitriding

LTTT: low-temperature thermochemical treatment

K22: low-temperature carburized with Kolsterising K22 process

NP: non-polished

OR: orientation relationship

P: polished

PN: plasma nitriding

PEMFC: polymer electrolyte membrane fuel cell

SEM: scanning electron microscopy

SF: stacking fault

S-phase: expanded austenite

SS: stainless steel

XPS: X-ray photoelectron spectroscopy

XRD: X-ray diffraction

y_N , y_C : nitrogen/carbon interstitial occupancy

γ_N , γ_C : nitrogen/carbon stabilized expanded austenite

Table of contents

1	Introduction	1
1.1	Background.....	1
1.2	Scope and research objectives	2
2	Materials and low-temperature thermochemical treatments	3
2.1	Stainless steels	3
2.2	Materials in this study.....	8
2.3	Low-temperature thermochemical treatments	13
3	Expanded austenite	18
3.1	History	18
3.2	Microstructure and characteristics	19
3.3	Interstitial diffusion mechanisms.....	21
3.4	Thermal stability.....	23
3.5	Mechanical, tribological and corrosion properties	24
3.6	Applications.....	25
4	Experimental techniques	29
4.1	Sample preparation	29
4.2	Optical microscopy studies.....	30
4.3	Scanning electron microscopy (SEM).....	31
4.4	X-ray diffraction (XRD).....	33
4.5	X-ray photoelectron spectroscopy (XPS)	34
4.6	Auger electron spectroscopy (AES)	35
4.7	Glow-discharge optical emission spectroscopy (GDOES).....	36
4.8	Hardness measurements	37
4.9	Pin-on-disc testing	38
4.10	Potentiodynamic and potentiostatic measurements	39
4.11	Interfacial contact resistance (ICR) measurements.....	41
5	Summary of results and discussion.....	43
5.1	Microstructure of low-temperature nitrided/carburized austenitic stainless steels....	44
5.2	Layer thickness of expanded austenite	45
5.3	Phase constituents of surface engineered austenitic stainless steels.....	47
5.4	Interstitial content.....	51
5.5	Thermal stability of expanded austenite	53
5.6	Hardening effect and hardening mechanisms.....	56
5.7	Tribological behaviour of LTC austenitic stainless steels.....	58

5.8	Electrochemical properties of LTC austenitic stainless steels.....	60
6	Conclusions	63
7	Suggestions for future works.....	65
8	Acknowledgements.....	67
9	References	69

1 Introduction

1.1 Background

Austenitic stainless steels are among the most used materials where high corrosion resistance is required. The applications range from pharmaceutical and food industry to offshore oil and gas, passing through biomedical and prosthetics [1]. The presence of chromium (Cr) with concentration above 11% guarantees a stable protective oxide. Anti-corrosion properties are also enhanced by presence of nickel (Ni). As an austenite stabiliser, it gives austenitic stainless steels a face-centred cubic (FCC) structure [1].

The major drawbacks of this class of materials are the low surface hardness and poor wear resistance, leading to high risk of adhesive wear (e.g. galling) [2]. Although it is possible to harden austenitic stainless steels by plastic deformation thanks to the high work-hardenability, this tends to decrease the general corrosion resistance especially in chlorine containing environments, due to high susceptibility to stress corrosion cracking.

Traditional thermochemical treatments used to case-harden steels are not suitable for stainless steels due to the high temperatures involved in the processes. Carburizing and nitriding are commonly carried out at temperatures above 850°C and 550°C respectively. The high affinity between Cr and nitrogen (N)/carbon (C), causes rapid precipitation of Cr-rich carbides/nitrides. The consequent Cr depletion in the matrix leads to a severe decay in corrosion resistance of the materials.

From the mid-80s, low-temperature thermochemical treatments (LTTT) involving both N and C were developed and attracted interest from both academia and industry [3]. Such processes induce the formation of a metastable interstitially super-saturated austenite phase, referred to as *expanded austenite* or *S-phase*. The interest in expanded austenite arises from the high interstitial content, orders of magnitude higher than the thermodynamic equilibrium, and the absence of precipitates [4]. These two factors assure up to a four to five-fold increase in hardness while maintaining or even enhancing the corrosion resistance.

Expanded austenite is an intrinsically complex structure. Being metastable, thermodynamic calculations cannot effectively predict the temperature and compositional ranges of a stable S-phase. Moreover, as a result of the diffusion process, high concentration gradients exist between an often present surface compound layer and the interstitial-free substrate. This generates high residual stresses and stacking faults (SFs) within the layer [5].

These properties, combined with the variegated treatment methods, make a comprehensive understanding of expanded austenite a complicated matter. During the last thirty years a number of research groups and industries have dedicated extensive studies on materials, processes, modelling and characterisation methods [6–9]. However, results are often controversial when not contradictory [6,10].

1.2 Scope and research objectives

The scope of this work is to evaluate how material characteristics (e.g. alloy composition, surface finish and phase stability) influence the microstructure and properties of expanded austenite layers formed by low-temperature thermochemical treatments.

The research objectives of this thesis are summarised as follows:

- To verify how alloy composition and surface finish affect the microstructural characteristics of expanded austenite layers formed during low-temperature nitriding/carburizing.
- To study the chemical interactions between supersaturated interstitial N/C and alloy elements in low-temperature nitrided/carburized materials.
- To identify the thermal stability and decomposition mechanisms of expanded austenite and the relation to alloy composition and surface finish.
- To understand how low-temperature thermochemical treatments influence the properties of the modified surfaces (e.g. hardness and corrosion resistance as well as tribological behaviour).
- To identify the secondary phases formed during low-temperature thermochemical treatment and the formation mechanisms.

Multiple advanced material characterisation techniques have been applied to fulfil the research objectives. This work is focused on C and N stabilised expanded austenite layers formed by industrial plasma nitriding (PN) and carburizing processes (Kolsterising® by Bodycote). These treatments have been used exclusively for benchmarking purposes. The efficiency of the treatments or the details of the process parameters are not within the scope of this thesis. The materials used in this work are all commercially available austenitic stainless steels.

2 Materials and low-temperature thermochemical treatments

2.1 Stainless steels

2.1.1 History

The most common carbon steels, on which the modern industry is largely based upon, generally exhibit poor resistance to environmental interaction. Rust is formed when steels are exposed to air. Corrosion becomes a significant issue especially in wet, marine and acidic environments.

Although the beneficial effects of adding Cr as alloying element to common steel was recognised as early as the 19th century, it is only one hundred years later that the word *stainless* actually became part of the academic and industrial world.

The characteristic corrosion resistance of Cr-alloyed steels is given by the ability to form a thin, continuous, adherent, self-healing, stable and passivating native Cr-rich oxide layer. A steel can be considered *stainless* when containing at least ~ 11 wt% Cr. However, it was early understood that Cr alone does not offer complete protection in every condition. In particular, addition of Ni and Mo are beneficial in Cl⁻ containing environment. These two elements not only modify the chemical composition of the passive oxide, but also change the phase constituents.

It was only after World War II and in particular after the '70s that accurate control of C and N content during processing (argon-oxygen decarburization) [11] allowed maximum flexibility in alloy design without incurring significant technological issues (e.g. embrittlement during welding) [11].

The world of stainless steel (SS) is in constant expansion. In the last decades the world consumption has consistently increased by ~ 6% [12], as given in Fig. 1. Industries are striving to achieve better performances, while keeping an eye on costs and considering price fluctuations of key alloying elements.



Figure 1 Left: the growth rate of major metals. Right: the stainless crude steel production by grade category. Redrawn from *Stainless Steel in Figures 2013 – International Stainless Steel Forum* [12].

2.1.2 Stainless steel grades

The family of SS can be divided into five different types: ferritic, martensitic, precipitation hardening, duplex and austenitic [1].

2.1.2.1 Ferritic grades

Standard ferritic grades contain mainly Cr (11 – 19 wt%) as alloying element, with little or no Ni. This allows the cost connected to raw materials to be stable and low, comparable to that of carbon steels but with significantly improved corrosion resistance. The microstructure is ferritic and therefore this type is magnetic. To prevent the formation of Cr-rich carbides/nitrides at the grain boundaries during welding, small amounts of Nb and/or Ti having higher affinity to C/N than Cr are added. As ferrite stabilizers, Nb and Ti can also be used to prevent formation of martensite.

The field of application usually ranges from room to high temperatures, especially in sulphur-containing atmospheres. Generally, ferritic stainless steels are not used at cryogenic temperature due to high brittleness in the low-temperature range.

2.1.2.2 Martensitic grades

Martensitic grades contain similar amount of Cr to that of ferritic SS, but in order to increase the austenite stability at high temperature, which is necessary for heat treatment, the addition of Ni, N or C is required. The martensitic stainless steels are magnetic and heat-treatable, following the same procedure as for conventional carbon steels (austenitising, quenching and tempering). Stainless steels belonging to this grade are the least corrosion resistant and are normally employed in similar application fields as the corresponding martensitic steels, including surgical equipment, razors, cutlery, bearings, etc.

2.1.2.3 Precipitation hardening grades

Precipitation hardening stainless steel is a highly specialized class, mainly used when higher strength at high temperature is required, although the corrosion resistance is not superior to that of more conventional ferritic stainless alloys. This type of steel can be further classified as martensitic, austenitic or semi-austenitic, depending on the nature of the main constituting phase. Most precipitation hardening stainless steels contain Ti, Al, Cu, Nb and Mo for strengthening purposes.

2.1.2.4 Duplex grades

Duplex stainless steel grades have a multiphase microstructure, typically ferritic-austenitic. High Cr content (17 – 30%) and rather low Ni content (1 – 7%) produce almost equal amount of ferrite and austenite following heat-treatment in the two phase region [13]. Other common alloying elements are Mo and N, which are used for improving strength, corrosion resistance against pitting and to balance the microstructure. Duplex stainless steels usually take advantage of both characteristics of ferritic and austenitic steels, with an additional benefit from the cost perspective due to the limited use of Ni.

2.1.2.5 Austenitic grades

Austenitic grades comprise a large variety of stainless steels, mainly tailored to specific application requirements. The largest kind in terms of production and application flexibility is

the Cr-Ni, also called “18 – 8” (type 304), and with addition of Mo (type 316) for enhanced pitting resistance.

Being austenitic at room temperature because of to the stabilizing effect of Ni (Mn, N as well in some cases), they exhibit high formability in a wide range of temperatures, from cryogenic to high temperatures, where the austenitic grades maintain their strength and formability more than ferritic grades do. The austenitic grades are not heat-treatable, but show excellent work-hardening ability. Carbon-lean variants have been developed (designated with L) to eliminate weldability problems related to carbides precipitation during welding, which lead to both embrittlement and loss of corrosion resistance.

Depending on the overall alloy composition and processing parameters, it is possible that a certain amount of δ -ferrite is retained within the austenitic structure [14,15]. Moreover, several austenitic alloys have tendency to form deformation induced martensite (α'), which has detrimental effect on the corrosion resistance.

An empirical formula for determining the formation temperature (M_d) of deformation induced martensite was proposed by Angel [16]. It relates to the alloy composition as follows (eq. 1).

$$M_d\left(\frac{30}{50}\right)[^\circ\text{C}] = 413 - 13.7(\text{Cr } \%) - 9.5(\text{Ni } \%) - 8.1(\text{Mn } \%) - 18.5(\text{Mo } \%) - 9.2(\text{Si } \%) - 462([\text{C} + \text{N}] \%) + \dots \quad (1)$$

In the equation, $M_d(30/50)$ represents the temperature at which 50 vol% of α' martensite is formed after a true tensile strain of 30%. Notice that the formula does not take into account factors, such as strain rates and pre-existing stress conditions.

Austenitic grades are not free from limitations and drawbacks. The protective Cr-rich oxide tends to spall-off during heating cycles, due to the large thermal expansion coefficient difference between the oxide and the matrix [17]. Moreover, austenitic stainless steels are susceptible to stress corrosion cracking [18] and exhibit low fatigue endurance limit as a consequence of their high work-hardening ability [19]. Furthermore, the low surface hardness and poor wear resistance pose a limit for many applications.

2.1.3 Effects of main alloying elements

2.1.3.1 Ferrite stabilizers

Chromium with a minimum concentration of ~ 11 wt% is the most important alloying element of stainless steels. The higher the Cr content, the higher is the corrosion resistance. This is also true for high temperature applications. As a strong ferrite stabilizer, Mo can significantly increase the strength at high temperature and the resistance to both general and pitting corrosion. However, the high cost and tendency to form unwanted secondary phases make Mo rarely exceed 6% in commercial alloys. Silicon increases resistance to oxidation, even when added in small amounts. Titanium and Nb are strong ferrite and carbide formers. They act as “traps” for C and N, preventing Cr depletion.

2.1.3.2 Austenite stabilizers

Nickel is the main austenite stabilizing element. At least 8 wt% Ni is necessary to assure an austenitic structure. Because of the relatively high cost and health-related concerns (allergies) there is a growing tendency to replace Ni with other austenite stabilizers. Manganese is used to partly replace Ni in biomedical applications. Another austenite stabilizer, Cu, is able to increase the corrosion resistance. Addition of Cu also increases N solubility and improves hot ductility. Carbon is a strong austenite stabilizer and it increases the mechanical strength of the alloys. Although a relatively large amount is used in martensitic stainless steels, C is generally unwanted in other grades because it may combine with Cr to form carbides, lowering the corrosion resistance. In particular, corrosion occurring at grain boundaries can be a major problem. In order to solve this, low-carbon bearing SS have been developed and classified as “L”, e.g. 304L and 316L. Nitrogen has the same effects as C. Both elements are interstitials and provide effective solid solution hardening effect. Nitrogen is more useful in this respect because it has lower tendency to cause intergranular corrosion. It is particularly beneficial for localised (pitting) corrosion resistance [20].

2.1.3.3 Nickel and chromium equivalents

Considering the high amount of alloying elements in SS, alloy design is of paramount importance. First of all, the composition of the alloy determines the chemistry of the native oxide formed at the surface, which is the key of corrosion resistance in SS. Secondly, each alloying element has either ferrite- or austenite-stabilizing effect. The balance has significant impact on the final microstructure of the alloy, which is in turn related to both corrosion and mechanical performances. The current available simulation tools are not always advanced enough to appropriately describe the coupling interaction between so many alloying elements; therefore, empirical rules are still widely used. One of the most used is the Schaeffler-DeLong diagram (Fig. 2), which gives an empirical representation of austenite-ferrite phase stability by calculating “Ni-equivalents” and “Cr-equivalents” (eq. 2 and 3) [1].

$$Ni(eq) = Ni \% + 30 \times (C \% + N \%) + 0.5 \times Mn \% \quad (2)$$

$$Cr(eq) = Cr \% + Mo \% + 1.5 \times Si \% + 0.5 \times Nb \% \quad (3)$$

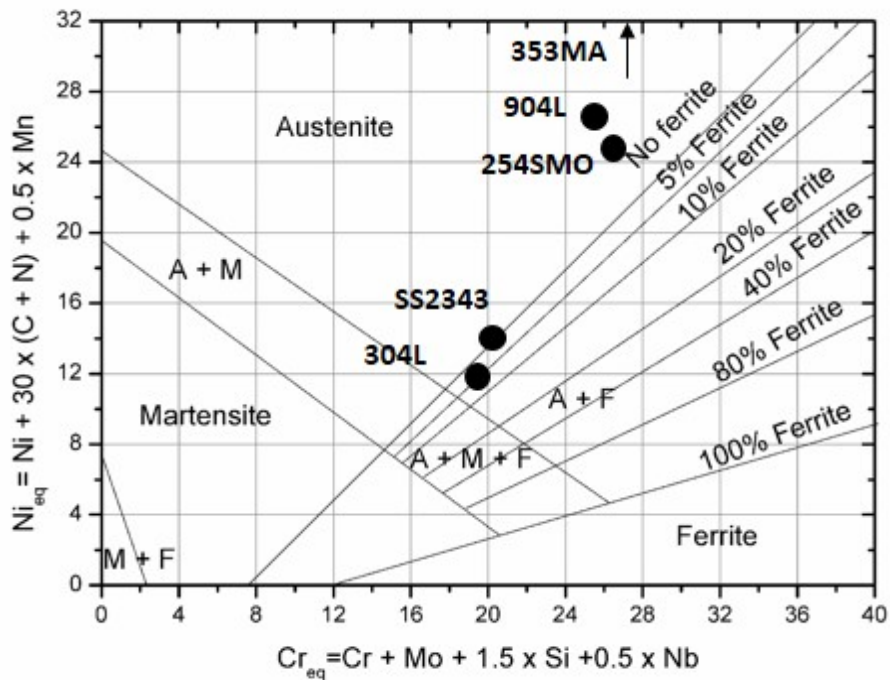


Figure 2 Schaeffler-DeLong diagram with 304L and 904L equivalent Ni and Cr composition, redrawn from reference [1] (A: austenite; F: ferrite and M: martensite).

This is a convenient way to represent the effect of various elements on the microstructure of Cr-Ni stainless steels. It can be seen from Fig. 2 that the high alloyed 254SMO, 904L and 353MA are within single austenite region while 304L and SS2343 may contain a minor amount of δ -ferrite. Several empirical diagrams can be found in the literature, each with varied application ranges and equivalence coefficients. They are routine references for studies on casting and welding. However, such empirical rules do not take into consideration some important factors, e.g. cooling rates.

2.1.4 Surface finishing

Surface finishing is an important operation during production of SS. It is generally accepted that limited maintenance is required for SS products through the whole life cycle. Therefore, the surface finishing is usually carefully chosen by the customer and is likely to be the one for the final product.

Pickling is the routine process for removing the oxide scales formed during annealing, hot-forming and joining operations. This oxide scale differs from the protective passive film typical of SS. It is instead a thick crust of mixed oxides formed during complex thermal cycles in non-controlled atmospheres. Below the oxide scale there is usually a Cr-depleted layer that needs to be removed in order to guarantee self-repairing capabilities of the protective oxide layer. Pickling solutions usually include HNO_3 , H_2SO_4 and HF. The use of HCl should be avoided since it might lead to localised pitting corrosion. When the oxide scale is too thick and exhibits

high chemical resistance, for example in case of high alloyed SS, the pickling phase is preceded by a mechanical descaling, such as shot-peening, sandblasting or brushing [1].

Depending on the required level of roughness fine grinding, polishing or electro-polishing can be applied. High reflectivity, which is directly related to roughness, is often sought after by final users [21].

2.2 Materials in this study

This thesis focuses on five different austenitic stainless steel grades: 304L, SS2343 (only 2343 in Paper V), 904L 254SMO and 353MA. All the materials used in this study were supplied by Outokumpu Stainless AB (Sweden) in form of 3 mm thick plate, except for the SS2343 plate which was supplied by Nyby Uddeholm AB (now Outokumpu AB, Sweden). The nominal chemical compositions as reported by materials suppliers are listed in Table 1. The choice of these alloys was made in order to cover a broad variety of material characteristics, such as Cr- and Ni-equivalents (see Fig. 2), different Mo content and austenitic phase stability. Moreover, the estimated corrosion resistance spans from low (304L) to very high (254SMO) [22] within the austenitic family, while the mechanical properties at room temperature are comparable for all alloys. Furthermore, the low amount of C (< 0.1 wt%) present in the base material is particularly important in order to minimize the presence of intergranular precipitates.

Table 1 Nominal alloy composition from materials suppliers (in wt%, Fe is in balance).

	C	Si	Mn	Cr	Ni	Mo	Cu	N	Ce
304L	0.02	0.3	1.6	18.3	8.1	0.4	0.3	0.07	-
SS2343	0.03	0.6	1.5	17.5	11.8	2.8	0.2	0.04	-
904L	0.01	0.3	1.6	20.3	24.6	4.8	1.4	0.05	-
254SMO	0.01	0.4	0.6	20.0	18.0	6.1	0.3	0.21	-
353MA	0.07	1.6	1.5	25.0	35.0	-	-	0.16	0.05

2.2.1 304L austenitic stainless steel

Type 304L, also known as ASTM/AISI/SAE 304L, UNS S30403, A2 SS or EN 1.4307, is the most versatile and widely used stainless grade available in the market. It is an “all purpose” grade characterised by good corrosion resistance, excellent formability and weldability. Additionally it is among the cheapest grades of austenitic stainless steels, making it the favourite choice of industry. It is particularly suitable for large structures, such as food and beverages containers, pharmaceutical industry, kitchenware, construction material (screws, bolts, etc.) as well as for exhaust systems within automotive industry [23].

As other austenitic stainless steels, 304L is non-magnetic, even though some δ -ferrite (0 – 5%) is commonly found in the form of stringers [24]. Controversial results have been reported

regarding the effects of δ -ferrite, including resistance to stress-corrosion cracking and tendency to cracking during cold work [25,26]. Applying eq. 1, it infers that deformation induced martensite can form at room temperature in 304L. This was experimentally demonstrated by several researchers in a number of experiments including uniaxial tensile tests and cold working [16,27,28]. In this study, the formation of deformation induced martensite due to mechanical polishing was shown by XRD and EBSD measurements, see Fig. 3.

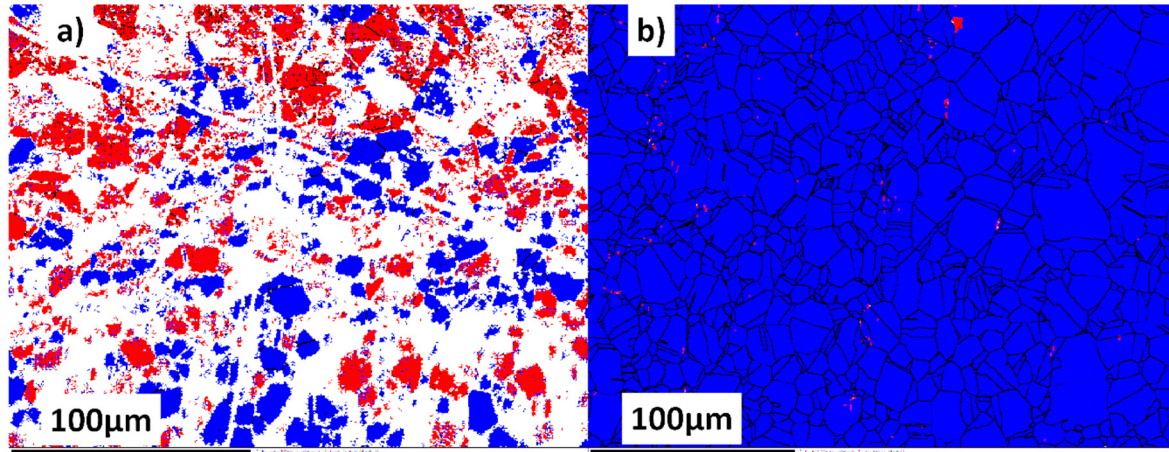


Figure 3 Electron backscatter diffraction maps. Left: Deformation induced martensite (red) on mechanically polished 304L surface (austenite in blue). Right: ferrite stringers (red) in electropolished 304L surface (austenite in blue). White: not determined (from Paper IV).

2.2.2 SS2343 austenitic stainless steel

The SS2343, also known as UNS S31600, ASTM/AISI 316 and EN 1.4307, is an evolution of 304-type, with addition of 2 – 3 wt% Mo to increase the pitting resistance. In fact, the 304-type SS is not sufficient to provide satisfying corrosion resistance in presence of chloride ions. The SS2343 is most commonly used for non-critical applications in marine environments, in food and chemical industry. This class of stainless steels is also the most commonly investigated materials for studies on low-temperature thermochemical treatments, as the application demands and the material price can justify the costs for an additional surface treatment. As seen from Fig. 2, the composition is at the limit to achieve a fully austenitic stainless steel. Therefore, good control on the cooling rate after welding is necessary to avoid presence of residual δ -ferrite, which can be deleterious to the corrosion resistance in acidic environment [29]. However, δ -ferrite was not detected at any stage within the SS2343 plate used in this study. Similarly, deformation induced martensitic transformation by conventional sample preparation was not detected either.

2.2.3 904L austenitic stainless steel

Type 904L, also known as UNS N08904, ASTM/AISI 904L, EN 1.4539, is a high-alloy austenitic stainless steel. It is often referred to as “superaustenitic” owing to the high stability of the austenitic phase (cf. Schaeffler diagram in Fig. 2) and high corrosion resistance. Alloy

904L is not susceptible to deformation induced martensite formation at room temperature, as suggested by eq.1.

The large amount of expensive alloying elements, especially Ni and Mo, make this material suitable only for high performance applications, where superior corrosion resistance is required and cost is not the key issue [30]. The alloying element Cu also offers a decisive improvement on corrosion resistance in specific environments that contain sulphuric acid and reducing agents. In particular, 904L is designed for applications involving concentrated acid solutions and chloride-containing environments, especially at relatively high temperature, where conventional austenitic stainless steels, such as 316L would fail [31]. Therefore, 904L is mainly employed in processing plants, such as pulp and paper industry, for oil and gas applications, and in marine environment.

2.2.4 254SMO austenitic stainless steel

The 254SMO is a high-Mo (6 wt%) superaustenitic stainless steel, also known as UNS S31254 and EN 1.4547. It is intended for use in the most demanding Cl⁻-containing environments, e.g. in offshore oil and gas applications. The 254SMO is alloyed with N in order to stabilise austenite while allowing a relatively low amount of Ni (cf. 904L), characterised by price volatility. Additionally, the resistance to pitting and crevice corrosion could, therefore, be increased.

2.2.5 353MA austenitic stainless steel

The 353MA (UNS S35315 and EN 1.4854) is a high-Ni, high-Cr austenitic stainless steel designed for high-temperature applications, employed in e.g. petrochemical industry. The resistance to high-temperature oxidation is achieved by addition of Si and micro-alloying with Ce [32], while the high temperature creep is enhanced by addition of N and C. The 353MA is also used for hot components in industrial furnaces involving N/C-containing atmospheres, where nitriding/carburizing can lead to premature fail due to embrittlement of grain boundaries, or so-called metal dusting.

2.2.6 Corrosion resistance

“Corrosion” is the deterioration of material-properties due to interaction with the environment, as a consequence of electrochemical processes. In aqueous corrosion, oxidation and dissolution of metallic species, e.g. Fe in steels, causes loss of material and eventually may lead to failure of an engineering component. The presence of Cr in SS, however, promotes the formation of a homogenous, adherent, self-healing and chemically stable Cr-rich oxide which can slow down the rate of material loss by orders of magnitude [33]. This process is called passivation. Stainless steels, however, are not immune to localised corrosion phenomena, where the self-healing capacities of the surface are limited by e.g. lack of oxygen necessary to maintain a stable surface oxide (e.g. crevice corrosion) or by local Cr-depletion (e.g. sensitisation of grain boundaries). Presence of halogen ions (Cl⁻, F⁻ and Br⁻) may also lead to local disruption of the passive film, creating pits, characterised by rapid growth. Some alloying elements have positive influence on the resistance to pitting. Chromium and Mo stabilise the passive film. Nitrogen

suppresses local acidification (buffering effect) in acid-pitting via ammonia formation [34,35]. Therefore, in engineering applications, materials are commonly ranked according to their “pitting resistance equivalent number” (PREN), calculated from the chemical composition of the steel, as shown in eq. 4:

$$PREN = Cr \% + 3.3 Mo \% + 16 N \% \quad (4)$$

The higher is the value of PREN, the better is the pitting resistance. Nitrogen is more effective compared with Cr and Mo. However, the effects of C, which in many other aspects is equivalent to N (e.g. austenite stabilisation) are not considered in PREN. While beneficial effects of C in the passivation behaviour of stainless steels have been shown in previous studies [37–39], the exact chemical pathways are still unclear. To include the effects of C and other alloying elements on the corrosion resistance, the MARC number was introduced (“measure of alloying for resistance of corrosion”) [39–41], as seen in eq.5:

$$MARC = Cr \% + 3.3 Mo \% + 20 C \% + 20 N \% - 0.5 Mn \% - 0.25 Ni \% \quad (5)$$

The PREN and MARC numbers for the materials studied in this work can be calculated as listed in Table 2.

Table 2 Pitting resistance equivalent number (PREN) and measure of alloying for resistance of corrosion (MARC) of the alloys examined in this study.

	PREN	MARC
304L	20.8	18.3
SS2343	27.5	24.4
904L	35.5	28.9
254SMO	43.7	39.1
353MA	27.6	19.5

The addition of large amount of Mo and N makes 254SMO the material in this study having the highest expected aqueous corrosion resistance. Instead, while 353MA contains the most Cr among the studied stainless steels, it does not surpass SS2343 due to the lack of Mo and the counter effect of Ni. It is important to remember, however, that other effects such as, surface finish and amounts of non-metallic inclusions (in particular MnS [42]) may affect significantly the pitting corrosion resistance.

2.2.7 Hardening of austenitic stainless steel

The major weaknesses of austenitic stainless steels are the low surface hardness and unsatisfactory tribological behaviour. It is of a common interest in academia and industry to improve these properties in order to extend the fields of application and to increase the lifetime of components made of these materials, making them more viable and cost-effective.

General hardening mechanisms in metals include work hardening, solid solution hardening, grain refinement, transformation hardening and precipitation hardening, depending on the materials and applied hardening treatment.

As described in previous sections, fully austenitic SS cannot be heat-treated to achieve an effective hardening through martensite formation. It is also not recommended to induce precipitation hardening through formation of Cr-compounds since that would compromise the general corrosion resistance. When alloying elements having higher affinity with interstitials are added, selective precipitation without Cr depletion occurs. We then enter in another class of SS, precipitation hardening stainless steels.

Austenitic stainless steels possess high work-hardenability, making cold-working a viable solution for hardening. However, these types of treatments (e.g. cold-rolling, sandblasting, shot peening) have complex effects on microstructure and corrosion resistance [43,44]. Furthermore, when metastable SS, such as 304L are subjected to severe mechanical deformation, martensitic transformation may occur, decreasing the general corrosion resistance [45]. On the other hand, subsequent controlled annealing followed by quenching might induce sufficient grain refinement by recrystallization. Tribological properties and the general corrosion resistance could be improved because of the increased Cr diffusivity through the grain boundaries created during the process [46].

When discussing solid solution hardening, one has to distinguish between the substitutional solid solution and the interstitial solid solution hardening. The first one is predominantly caused by the different size of atoms constituting the alloy. A lattice strain field is created, hindering dislocation movement and therefore hardening the steel. This is normally present in austenitic stainless steels containing significant amount of alloying elements. In the second case, lattice strain is induced through occupancy of interstitial sites by usually N and/or C (but also B sometimes). It was already mentioned that in stainless grades interstitial content is usually kept as low as possible during production in order to avoid Cr-precipitates. For the same reason, conventional high temperature ($T > 500^{\circ}\text{C}$) thermochemical treatments, such as nitriding, carburizing and carbonitriding aiming at introducing large amounts of interstitials are not suitable, since they generally lead to sensitization of grain boundaries (Fig. 4) [47,48].

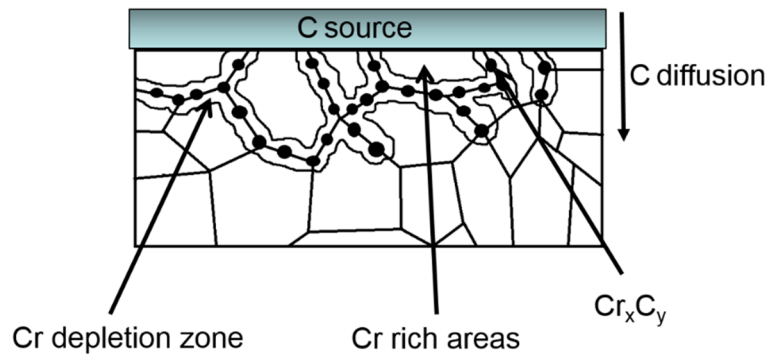


Figure 4 Schematic of sensitization process following traditional high-temperature carburization process. Cr-rich precipitates formed at the grain boundaries lead to Cr-depletion in the neighbouring regions and intergranular corrosion.

2.3 Low-temperature thermochemical treatments

Developing efficient and industrially scalable surface hardening processes for austenitic stainless steels without hindering the corrosion resistance is highly desirable but poses considerable technological challenges. Since the middle of the '80s, thermochemical treatments involving diffusion of C and/or N at low temperature ($T < 450^\circ\text{C}$) provided new possibilities.

In these processes, precipitation of Cr compounds could be delayed, allowing sufficient interstitial diffusion to form a hardened layer having thickness of several tens of micrometres. At such low temperatures, the interstitials not only remain in solid solution, but they can also reach concentrations orders of magnitude higher than in thermodynamic equilibrium. This phenomenon is called "colossal supersaturation" and leads to the formation of a "metastable interstitially supersaturated expanded austenite", simply referred to as "expanded austenite" or "S-phase".

The most common methods for low-temperature thermochemical treatment (LTTT) are nitriding and carburizing, or combinations of the two, both in gas or plasma processes.

Gas processes have the advantage of being highly controllable (gas composition, process parameters) and parameters can be adjusted from "traditional" heat treatment processes. However, it is difficult for interstitials to diffuse through the protective oxide film of austenitic stainless steels. A specific reduction pre-treatment is therefore necessary, which makes the process costly and more complex.

Plasma processes, however, work at low pressures and the total gas consumption is therefore significantly reduced, providing both economic and environmental benefits. Moreover, the passive layer is removed *in situ* by constant sputtering of the material surface. An efficient activation process is thus able to take place under the action of plasma, making the usage of non-hazardous N or C-carrying gases possible. However, plasma techniques suffer from the high costs of the pumping equipment necessary to reach good pre-vacuum and the requirement for optimizing and controlling many parameters. Moreover, depending on the geometry of the

part to be treated and the plasma techniques, inhomogeneity problems can arise due to charging effects, arcing or shading.

In this study we have characterised the expanded austenite layer formed by means of two industrial processes, plasma nitriding and gas carburizing, performed by Bodycote Värmebehandling AB in Stockholm and in Vellinge (Sweden).

2.3.1 Nitriding

2.3.1.1 In general

Nitriding is a surface engineering method which relies on nitride formation within a metal matrix. Compared to other thermochemical treatments, it requires the lowest treatment temperature (from 315°C to 540°C) [49]. Alloys containing significant amount of nitride formers, such as Al, Cr, Ti, Mo are also called “nitriding alloys” and are specifically designed to benefit from such processes.

The typical structure of a nitrided layer includes a gradient of nitride compounds with decreasing stoichiometry, followed by an interstitial diffusion layer and finally the bulk, as shown in Fig. 5.



Figure 5 Schematic structure of a nitrided layer.

The composition and proportion of the compounds present within the layer is highly dependent on both the process parameters and the alloy composition (ϵ -Fe₃₋₂N, γ' -Fe₄N, CrN in stainless steel). Higher temperatures and longer treatment duration lead to an increase in thickness of the compound layer. Compared to low alloyed steels, high alloyed steels exhibit a thinner compound layer [50]. Nitriding of austenitic stainless steel is mainly performed either through gas nitriding or plasma nitriding.

Gas nitriding relies on the use of ammonia or ammonia-hydrogen mixtures (eq. 6) [50], which first requires the removal of the surface oxide layer. This can be performed *ex situ* by electrochemical treatment of the steel, which leads to dissolution of the Cr-rich oxide. Subsequently, a thin Ni or Fe layer is plated to prevent re-passivation [51]. Nickel and Fe also act as catalysts for the decomposition reaction of ammonia during the heat treatment [52].



After the diffusion of atomic N, the catalyst layer is removed by acid and passivation can be restored. The compound layer formed during nitriding can also easily be removed in the post-treatment process by pickling. The disadvantage resides in the number of steps required in this procedure.

Alternatively, de-passivation can be performed *in situ*, during the heat-treatment cycle. The procedure involves flushing with halogen-based compounds (e.g. HCl, NF₃) prior to nitriding process. However, these compounds are aggressive to the furnace. Addition of NO to NH₃ has been proven to be a viable alternative for activation of SS surfaces [53].

2.3.1.2 Plasma nitriding in this study

In plasma nitriding (PN), the part to be treated is placed within the vacuum chamber, which is evacuated until certain vacuum condition is reached (from ~ 1000 Pa to < 10 Pa, depending on the specific plasma technique [55]).

In a generic (direct current) plasma set-up (Fig. 6), a mixture of N₂/H₂ is introduced into the chamber and kept at a pressure in the order of several tens of mbar. Subsequently, a voltage in the range of 100 – 1500 eV is applied between a cathode and the part at anodic potential, generating a glow discharge. At this point, the positively charged species are accelerated towards the part to be treated and impinge, converting their kinetic energy into heat and sputtering atoms from the sample surface. In this way, a layer with high N concentration is created in the near-surface zone and diffusion can start. External heating and temperature monitoring are often required to assure a fast and controlled operating temperature [54].

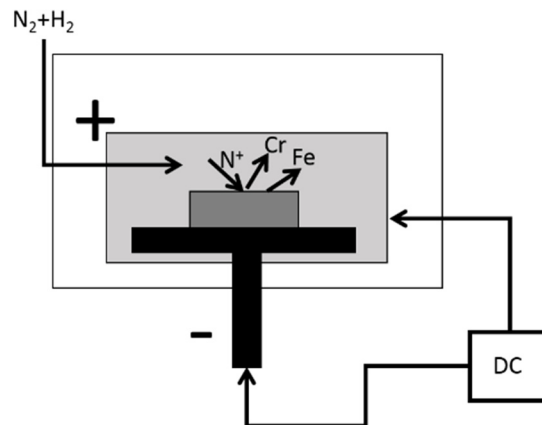


Figure 6 Schematic arrangement of plasma nitriding process.

In this study (Paper I and Paper III), the PN of two austenitic stainless steels 304L and 904L was performed in industrial furnaces at 400°C in N₂/H₂ atmosphere. Two process conditions were used, i.e. low N₂ partial pressure (L, $p_{N_2} = 6\%$) for 24 hours and high N₂ partial pressure (H, $p_{N_2} = 25\%$) for 99 hours, respectively. Details about other process parameters, such as surface activation conditions, total pressure and specific plasma technology used are proprietary and their influence on the nitrided layer microstructure is not within the scope of this study.

As seen in Fig. 7e, the PN process might result in a non-homogeneous treatment of the coupons. The central area exhibited a dull appearance (Area 1), while the rest of the coupon remained mirror-like (Area 2). Occasionally, bright regions could be observed near the edges of the coupon. This effect is probably related to the specific geometrical configuration of the PN equipment employed and/or due to edge effects on the samples.

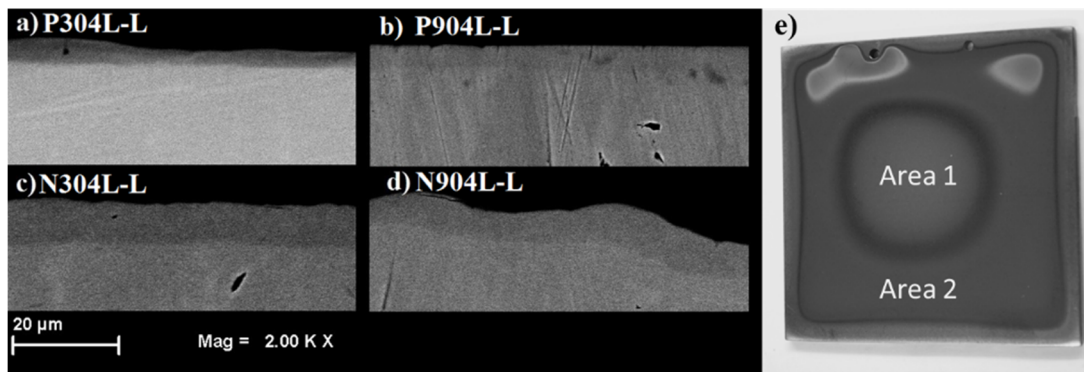


Figure 7 (a–d) Backscattered electrons image of the cross-section from nitrided steels and (e) top view of the polished and nitride P904L-L (from Paper I).

2.3.2 Carburizing

2.3.2.1 In general

Carburizing is a very old process, used for centuries to surface harden steels. Powder carburizing (charcoal), salt bath carburizing (cyanides), gas carburizing and plasma carburizing are among possible carburizing techniques available nowadays. However, only gas and plasma methods are viable options for austenitic stainless steels due to the requirement of low processing temperatures.

Gas carburizing is the most widespread and consolidated technique for surface hardening of SS. Halogen reduction of surface oxide layer using the so called “endothermic gas” mixture of CO/H₂/H₂O is a standard procedure in conventional carburizing treatments, as indicated in Fig. 8 [9].

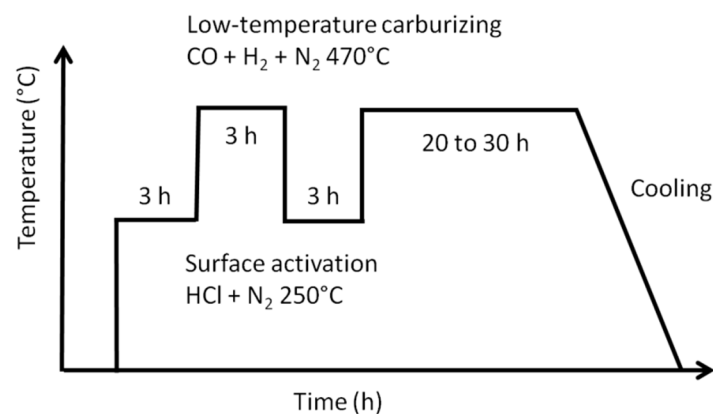


Figure 8 Schematic process of Swagelok low-temperature carburizing treatment (redrawn from reference [9]).

Modern techniques use gas mixtures, which are able to both reduce the passive layer and induce an efficient precipitate-free carburizing layer, simultaneously. The recently patented processes by Swagelok Company and Expanite A/S, for example, include acetylene/hydrogen and acetone among other gases [55,56].

The studies on low-temperature plasma carburizing processes started in the ‘90s and continued through the ‘00s. They are particularly interesting from an industrial prospect because of the

higher efficiency and use inexpensive C-carrying gases (e.g. CH₄, C₃H₈), which are otherwise impossible to thermally decompose using traditional gas carburizing. Hydrogen is added to limit the formation of soot, often formed in low-temperature carburizing (LTC). Unfortunately, important process parameters (temperature regimes, gas mixtures) involved in successful surface hardening of stainless steels are often kept as trade secrets.

2.3.2.2 Gas carburizing in this study: Kolsterising®

In this study, the surface modification induced by Kolsterising® K22 LTC treatment supplied by Bodycote Värmebehandling AB was characterised. This treatment was first presented by Kolster in 1983 with the name HardCorr, which can be considered as the first LTC process ever entering the market [51]. Key process parameters, such as gas composition, time-temperature regimes and surface activation procedures have not been published. It is claimed that this process induces C supersaturation without Cr-containing precipitates [57] in several austenitic stainless steel grades, including 304L, 316L and 904L. A diffusion layer with thickness ranging between 20 µm and 30 µm with surface hardness as high as 1200 HV is commonly reported [9].

3 Expanded austenite

Throughout this thesis and in all the appended papers, “S-phase” and “expanded austenite” are used interchangeably to describe a metastable supersaturated interstitial solid solution of N or C in an austenitic matrix.

3.1 History

It is generally accepted that S-phase was first discovered in 1985 [60]. Beneficial effects of interstitial supersaturation in austenitic stainless steels were demonstrated by independent studies done by Zhang and Bell, at Birmingham University [58], and Ichii from Kansai University [59]. Dedicated works were performed by both groups on PN, a prospective technology for surface hardening of stainless steel while avoiding Cr nitrides precipitation. The characteristic presence of a white-etching layer was the first hint of maintained, or even improved corrosion resistance of the hardened layer.

The first term used when addressing the hardened layer was “S-phase”, referring to the “satellite” peaks appearing at lower angles of the typical X-ray diffraction patterns of the FCC phase from the austenitic substrate (Fig. 9) [6].

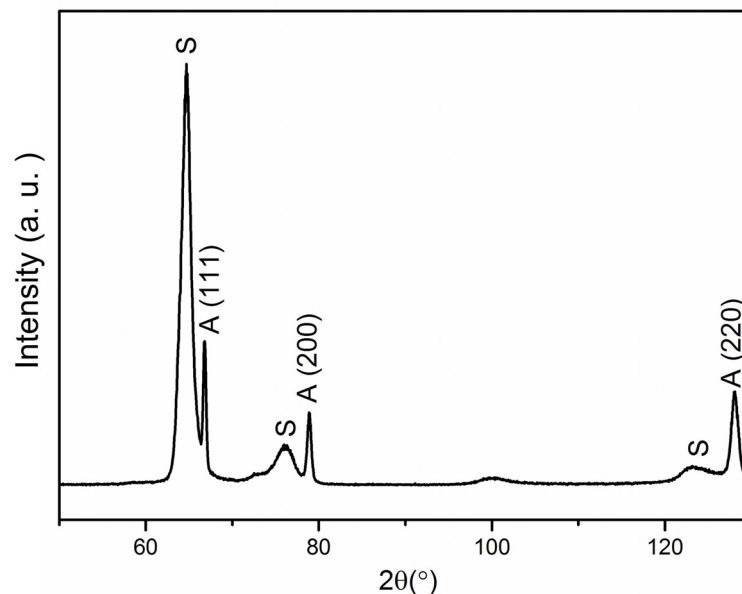


Figure 9 S-phase X-ray diffraction pattern as identified from data collected by the author on plasma nitrided 904L (redrawn from Paper I).

In fact, two years before Zhang, Bell and Ichii, Kolster had already published results of a surface treatment, which provided an outstanding hardening effect on SS, and began commercialization of a low-temperature carburizing process named HardCorr. It was later renamed Kolsterising and it is now property of Bodycote Heat Treatments [8].

It has been speculated that studies performed during the ‘60s on liquid sodium induced corrosion by Litton, Morris, Anderson and Sneesby on stainless steel were the source of inspiration for Kolster [8]. In those studies, C-contaminations in liquid sodium were causing

carburization of SS and loss of corrosion resistance. However, it was observed that an interstitial diffusion zone with high corrosion resistance was present at exposure temperatures below 550°C [8].

3.2 Microstructure and characteristics

3.2.1 Crystal structure

The nature of nitrogen/carbon-induced S-phase has been disputed for many years and several denominations were used to describe what is nowadays most commonly referred to as expanded austenite. This was due to the difficulty in determining the “real” crystal structure of interstitially supersaturated austenite.

Nitrogen containing S-phase was initially described by Ichii, Zhang and Bell as a mixture of γ' compound M_4N ($M = (Cr, Fe, Ni)$) having FCC structure and austenite. However, it was found that the lattice expansion measured by XRD was not isotropic, being more pronounced in (200) diffraction peaks; therefore, some authors believed that expanded austenite has a tetragonal nature and referred to it as ϵ' or M-phase (from “martensite”). Some other authors have even considered an amorphous nature [6]. By TEM studies, Fewell et al. described the nature of expanded austenite as a “substantially” cubic FCC structure [60].

There is ongoing debate about the origin of the anomalous expansion measured by XRD; three of the most commonly accepted explanations are as follows.

- 1) Tetragonal deformation would be the simplest explanation of the XRD patterns. The studies by Martinavicius and Abrasonis on single crystal confirmed the enhanced diffusion in direction perpendicular to $\{100\}$ crystal orientations [61–63], implying anisotropic expansion due to different stress relaxation at the surface. This theory was recently further strengthened using EBSD analysis by Templier et al. [63], who showed the existence of a texture gradient through the expanded austenite layer.
- 2) Alternatively, Fewell et al. proposed a triclinic type of distortion. However, some characteristic diffraction lines (e.g. (100), (221)) have not been detected yet [64].
- 3) The third theory, proposed among others by Christiansen and Somers, ascribes the shift of diffraction peak position to the presence of stacking faults (SFs) induced by the N-supersaturation in a nitriding process [65]. The importance of SFs is generally accepted and a large amount of twins and SFs is observed by TEM analysis [64].

Similar statement is applied to C-stabilised expanded austenite.

The presence of a thin compound layer consisting of CrN and α -Fe is frequently encountered in PN, but it might be thinned or eliminated with appropriate N_2 - H_2 gas mixing. For low-temperature carburizing, a surface compound layer is more rare. However, presence of χ -Hägg (M_5C_2) carbides was reported on LTC of 316L with Kolsterising [66] and Swagelok [67,68] LTC treatment. The same compound was observed on carburized 304L and SS2343 by the author (Papers II, IV and VII).

3.2.2 Supersaturation, stacking faults and residual stresses

Solid solubility of C in austenitic stainless steels, such as AISI 304 or 316, is of maximum ~ 0.015 at% in thermodynamic equilibrium [69], while in expanded austenite up to ~ 14 at% was reported in the literature and was confirmed by the author in Paper IV. Metastable solubility of N is even higher and can reach up to 25 at%, while at thermodynamic equilibrium solubility is < 0.65 at% [6].

At least two reasons can be counted for the higher solubility threshold of N compared to C. First of all, N has smaller atomic radius than C, which allows filling octahedral interstitial sites of austenite with a relatively smaller lattice distortion. Another reason is the higher affinity between N and nitride forming elements (mainly Cr in stainless steels) compared to C for carbides. It has also been shown that presence of strong nitride/carbide formers (in order of Ti, V, Nb, Al, Cr, Mo, Mn) can significantly enhance the solubility of interstitials in austenitic stainless steels, while Ni and Si hinder it [70].

The short range ordering between N and Cr was proven by Oddershede et al. with extended X-ray absorption fine structure (EXAFS), which revealed a different interaction compared to that of a CrN-type of precipitates [71]. A similar study performed on C-containing S-phase showed a smaller ordering compared with N [72].

A linear dependence between austenite lattice parameter (a) and interstitial content has been proposed by Christiansen and Hummelshøj for both N-stabilised (γ_N) [73] and C-stabilised (γ_C) expanded austenite (interstitial lattice expansion coefficient is expressed in nm), as shown in eqs. 7 and 8 [74]:

$$a = a_0 + 0.05987 y_N \quad (7)$$

$$a = a_0 + 0.06029 y_C \quad (8)$$

In these equations, y_N and y_C are octahedral interstitial occupancies of N and C respectively, or in other words, the number of interstitial atoms per one hundred metal atoms. It has to be highlighted that the study by Christiansen and Hummelshøj was performed on highly controlled nitriding/carburizing conditions, which assured homogeneous interstitial content throughout the whole metal thin foil without concentration and stress gradients.

Except for thin foils ($< 100 \mu\text{m}$), through-specimen homogeneous carburization can never be achieved and the lattice expansion is confined by the bulk. The gradient in interstitial concentration, arising from diffusional processes, causes a gradient in compressive residual stresses through the expanded austenite layer. Below the interstitially enriched zone there will be a tensile residual stress state, as schematically shown in Fig. 10. Therefore, very high compressive residual stresses (> 2 GPa) arise in a region below the surface [75].

Strains are directly related to the stresses, through orientation dependent elastic constants (also called X-ray elastic constants). For this reason, X-ray diffraction patterns of expanded austenite, representing diffraction planes having a gradient in spacing, are often significantly broadened when compared to the diffraction patterns of untreated materials.

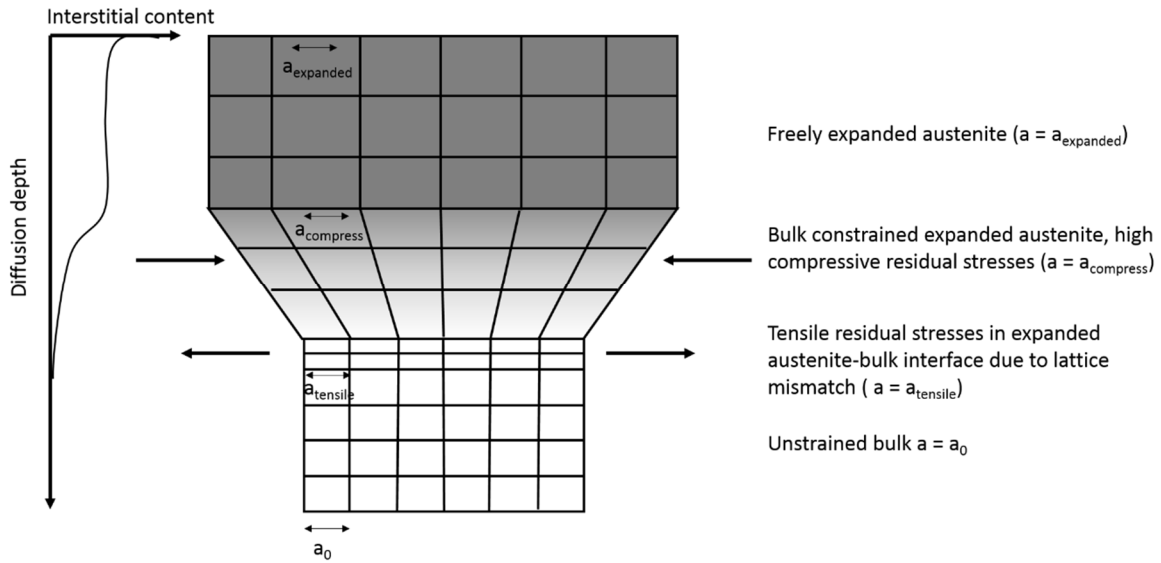


Figure 10 Schematic lattice stress-strain state induced by expanded austenite formation (not in scale).

High residual stresses are, at least partly, released by plastic deformation. In case of expanded austenite, the presence of slip bands and even twinning is commonly observed, as indicated in Fig. 11.

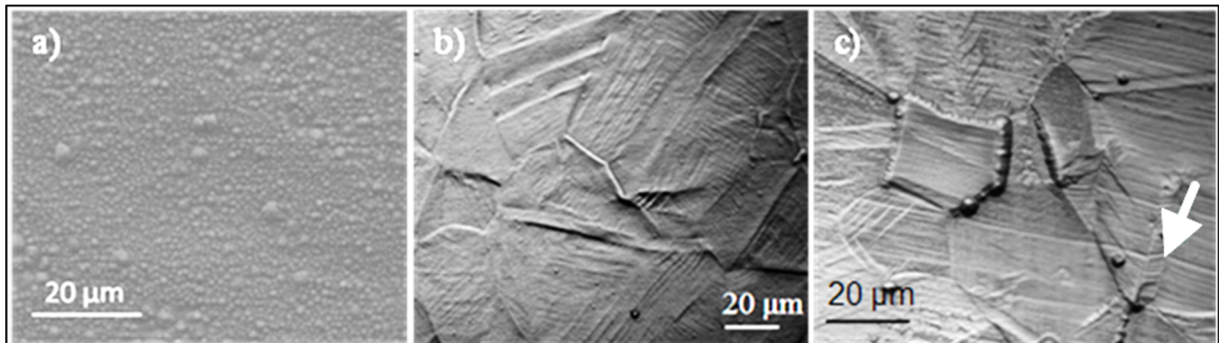


Figure 11 Topography of plasma nitrided (a) P304L-H, (b) P304L-L and (c) P904L-H. Plastic deformation in the form of slip bands and twinning (white arrow) is evident, in particular in 904L. Different protrusion of grains is also observed (from Paper I).

In particular, twins are related to the SF probability and influence both XRD peaks shape and position [76]. The effect of alloying elements in complex austenitic stainless steels is not completely understood, but it is believed that N in LTN materials lower significantly the SF energy, thus promoting twinning [77], as indicated by the arrow in Fig. 11c.

3.3 Interstitial diffusion mechanisms

A precipitate-free interstitially supersaturated case can only be formed if the diffusivity of interstitials at a certain temperature is significantly higher than the diffusivity of reactive substitutional elements, such as Cr for austenitic stainless steels. This is generally true for temperatures below $\sim 450^\circ\text{C}$, where diffusion coefficients of C and N are several orders of magnitude higher than that of Cr.

One of the most interesting characteristics of expanded austenite is the exceptionally high diffusion rate of interstitials. Using a classical diffusion model, Williamson found that the theoretical activation energy for N interstitial diffusion (1.45 eV) in expanded austenite is significantly lower than the one reported for the diffusion of N in FCC phase of stainless steel (1.87 eV) and in Fe (1.74 eV). This explains why interstitials diffuse four to five order of magnitude faster in expanded austenite compared to those in normal austenite [78].

Still, the interstitial concentration profiles cannot be correctly predicted by Fick's second law. A "trapping" mechanism was instead proposed by some researchers who hypothesized that the octahedral "trap sites" adjacent to Cr are progressively saturated before further diffusion of interstitials is allowed [79]. With this model we can explain the observed constant concentration plateau. A subsequent "detrapping" contribution in the model is particularly useful when describing simultaneous or sequential C and N diffusion [80]. C is replaced by N in the traps due to the higher interaction between N and Cr, with C being "pushed-in", generating a double expanded austenite layer. This also explains why LTN materials present a more steep diffusion profile after the concentration plateau region compared to that when introducing C. For the same reason, the γ_N is generally thinner than γ_C for comparable time-temperature regimes. Moller and Parascandola presented a model of interstitial concentration dependence on depth and time $c(x, t)$ for ion implantation plasma nitriding, where interstitial concentration in solute form $c_s(x, t)$ and trapped form $c_T(x, t)$ contribute separately, see eq. 9 below [81].

$$c(x, t) = c_s(x, t) + c_T(x, t) \quad (9)$$

$$\frac{\partial c_s}{\partial t} = D \frac{\partial^2 c_s}{\partial x^2} + j_0 f_R(x) - T(x, t) \quad (10)$$

Equation 10 gives the diffusion equation of interstitial solute. The first term on the right is the contribution of classical concentration gradient diffusion ($D \frac{\partial^2 c_s}{\partial x^2}$). The second term is the incoming flux of ions $j_0 f_R(x)$ and $T(x, t)$ represents the amount of trapping as expressed in eq. 11. This trapping contribution is substantially dependent on the trap radius (R_T), the trap concentration (c_T), the binding energy of the traps (U_T), the coordination number (n_z) and the host atomic density (n_H).

$$T(x, t) = 4 \pi D R_T \left[c_s (c_T - c_t) - z n_H c_t e^{-\frac{U_T}{kT}} \right] \quad (11)$$

The diffusivity is not only dependent on the concentration gradient but also on the concentration itself [82]. Diffusivity is higher at high concentrations, probably due to the lattice expansion which further reduces diffusion activation energy. When interstitial content is above a certain threshold (e.g. $y_N = \sim 0.45$ for 304 and 316) diffusivity decreases again, probably due to an "over-saturation" of interstitial sites, reducing probability of inter-interstitial sites jumps [82].

Original lattice parameter of an austenitic alloy seems to have significant influence on the solubility and diffusivity within S-phase [83]. It was shown that alloying elements with large atomic size, such as Mo and Cu, can enhance diffusion and possibly contribute to the increase in the supersaturation limit [84,85].

Alloy composition is not the only determining factor in diffusivity of interstitial species in forming an expanded austenite layer. It was reported that externally applied tensile stresses can positively enhance the final case thickness [86]. The same effect has been reported for high plastic deformation or grain refinement, which can provide low-energy diffusion paths through grain boundaries and high dislocation density regions [87]. However, presence of ferritic/martensitic phases can significantly delay the growth of S-phase [6]. Consequently, precipitates might be formed instead.

3.4 Thermal stability

Expanded austenite is inherently metastable, with thermodynamic driving force to form nitrides and carbides.

It has been observed that prolonged treatment of LTTT can lead to unwanted Cr compound precipitation. For nitriding of stainless steels, precipitation of CrN and Fe_xN compounds is commonly reported [88–90]; while for carburizing processes precipitation of M₅C₂ (monoclinic χ -Hägg carbides) may occur [66,69].

The formation of carbides and nitride due to thermal decomposition of expanded austenite leads to massive Cr depletion and loss of corrosion resistance. Its kinetic is, thus, of paramount importance for industrial application. Several studies about thermal decomposition in the most common austenitic alloys, e.g., AISI 316L and 304L have been published. Li et al. [6,91] claimed the maximum temperature is about $\sim 500^\circ\text{C}$ for γ_N and $\sim 650^\circ\text{C}$ for γ_C before rapid decomposition (< 1 h) occurs, leading to nitride/carbide formation. However, much lower operating temperatures are admissible in real applications. Bodycote recommends that the application temperature should not exceed $\sim 300^\circ\text{C}$ for materials treated with Kolsterising treatment, while laboratory tests on AISI 316L shows that isothermal decomposition occurs at $\sim 300^\circ\text{C}$ for γ_N and $\sim 350^\circ\text{C}$ for γ_C , giving a few years lifetime to expanded austenite [91–93].

Experiments on isochronal annealing (heating rate 0.417°C/s) by Christiansen on N-supersaturated 304L and 316L demonstrated that alloy composition has an influence on the decomposition temperature and its route [94]. Decomposition of AISI 316L takes place at temperature about 50°C higher compared with that of 304L [94]. When annealing is performed in a reducing atmosphere, denitriding is observed and is more prominent in 316L. The reason is supposed to be the presence of Si in 304L, which might form silicon nitrides and “trap” more N within the material. Further analysis also proved different decomposition routes based on the decomposition products. Expanded austenite in 304L evolves through a eutectoid decomposition route (eq. 12), leading to the formation of ferrite and nitrides. A discontinuous process is instead hypothesised for 316L, where nitrides are accompanied by austenite phase (eq. 13 [94]).



The different alloy composition might influence the decomposition route by shifting the ferrite-austenite transformation temperature, giving rise to larger range of stable austenite in 316L

[94]. The same phenomenon was observed in Paper III and Paper IV comparing 304L and 904L. Both N- and C-stabilised expanded austenite 304L thermally decomposed via eutectoid decomposition route, while 904L via discontinuous decomposition.

Thermodynamic calculations suggest that the stability of precipitate species in carburized austenitic stainless steels is highly dependent on the C-supersaturation levels. The higher the C-content, the higher the “order” of the carbide ($M_3C_2 > M_7C_3 > M_{23}C_6$) [8].

3.5 Mechanical, tribological and corrosion properties

3.5.1 Mechanical properties

One of the main characteristics of expanded austenite is the extremely high surface hardness, even higher than that of martensitic stainless steels. It is not unusual to achieve hardness of 800-1000 HV from γ_C and 1200 – 1500 HV from γ_N , respectively. The generic explanation is the presence of high amount of interstitials, accounting for solid solution hardening and tetragonal lattice distortion due to the strain field created in the material. Larger hardening effects are normally achieved by LTN treatments owing to the higher interstitial occupancy and consequently higher residual stresses.

It is important to remember that measured hardness on materials subjected to LTTT are extremely dependent on the applied loads. Expanded austenite is usually rather thin (few tens of μm), with a hardness gradient towards the bulk. Hardness measurements performed perpendicularly to the case-hardened surface with low-load will show higher hardness compared to that at higher loads. The reason is the gradient in interstitial concentration and compressive residual stresses. For the same reason, measurements performed on cross-sections systematically give lower hardness compared to the one performed on the surface with the same load.

Another important property to be taken into consideration is toughness. From micro-tensile test it was observed that γ_N significantly reduces the ductility of the austenite, while γ_C does not show that [97]. Hardness and toughness are often competing properties. The higher dislocation density and more twins induced in γ_N are likely to be responsible for this “N-embrittlement”. Cracks have been observed extensively in heavily nitrided 904L stainless steels (Paper I).

Fatigue resistance is also considerably improved ($\sim 20 - 50\%$) both by LTN and LTC, because of the high hardness and compressive stresses [95,96]. It was observed that failure cracks develop mainly at the interface between expanded austenite and bulk material [97].

3.5.2 Tribological properties

Improvement of tribological properties of austenitic stainless steels is one of the main driving forces for understanding and optimising expanded austenite. Similar to hardness, wear measurements are highly dependent on the method. For low applied loads of the order of ~ 10 N, reduced wear rate of even two orders of magnitude is reported and it is generally accepted that expanded austenite provides wear resistance [98,99].

When high loads are applied, however, the so called “thin ice” phenomenon might occur and wear resistance might actually be reduced. Due to the relatively small thickness of expanded austenite layer, in the case of high applied load, stress concentration in the bulk region gives rise to a “ploughing” effect, causing the loss of the hard layer [100].

The same problem arises in terms of load bearing capacity. When the applied load is high enough to be concentrated in the proximity of the case-bulk interface, cracking may occur there [100]. This can be an issue for applications, such as bearings or joints under compressive stresses.

3.5.3 Corrosion properties

Precipitate-free expanded austenite conventionally appears on metallographic cross-sections as a white etching layer. This suggests that wet corrosion resistance is enhanced or at least not decreased [101].

Controversial reports are presented in case of γ_N . On one hand, in the corrosion test performed in NaCl-containing acidic environments, higher resistance to acid pitting corrosion is observed [102]. This is probably due to the release of reactive N in the solution where quadrivalent N combines with four hydrogen ions to form ammonium ions, thus reducing the acidity of the solution near the surface and increasing the stability of the passive film (buffering effect) [34]. The same beneficial effect is observed with γ_C , even though no mechanism has yet been established [6].

On the other hand, corrosion resistance of γ_N in Cl⁻-free environment appears to be slightly reduced. Expanded austenite induces microstructural defects and high energy surfaces, such as slip planes, twins and SFs, which tend to dissolve quickly in an acid environment. It can be assumed that γ_C would suffer less from this problem given the lower extent of internal stress-strain generated [103].

3.6 Applications

Austenitic stainless steels are often employed in industry mainly because of their high corrosion resistance. However, their poor tribological properties often limit the range of application or impose high maintenance costs. For these reasons, in several applications it is certainly worthwhile for industry to invest in LTTT and form the expanded austenite case at the surface.

3.6.1 Nuclear industry

One of these examples is in the nuclear industry, where raw materials are not the main source of costs, but downtimes for safety maintenance are extremely costly [104].

Control-rod cluster tubes are manufactured using austenitic stainless steel and their function is to hold neutron absorbing material to moderate nuclear reactions. The tubes tend to suffer from wear with their guide tubes due to repeated insertion-removal cycles and vibrations induced by hydraulic flow.

The whole control-rod cluster tubes can be plasma nitrided in large pit furnaces, with precise temperature control in order to assure a homogeneous heating throughout the tube and avoid charring and arcing defects. The treated tubes are not only superior to untreated SS, but also able to compete with those having anti-wear coatings such as Cr-plating and Cr-carbide plasma spraying. Low-temperature nitriding treatment completely eliminated the necessary yearly replacement of the tubes [104].

3.6.2 Tube fittings and fasteners

Chemical, pharmaceutical, food and petrochemical industries employ austenitic stainless steel in the majority of their piping systems. Tube fittings are necessary to connect pipes and withstand high pressure. One of the key elements is the “back ferrule”, which has the role of gripping and sealing the tube [105]. To achieve that, it has to be plastically deformed in a controlled manner to adhere on the pipe. Toughness, hardness, corrosion and galling resistance are desirable properties for such purpose.

Low-temperature carburizing treatment provides possibilities to meet these requirement. Kolsterising and Swagelok represent viable commercial processes and standard practice for these applications nowadays.

3.6.3 Other applications

3.6.3.1 Ultraclean-sterile environments

Other applications include screws and nuts for high-purity gas fittings. The use of lubricants which might induce contaminations is avoided. At the same time galling is prevented. Avoiding lubricant residuals is of paramount importance for pharmaceutical and food industry. Dosing pumps for example are conventionally designed using rubber seals between cylinder lines and pistons to prevent adhesion wear. However, they naturally degrade and might contaminate the final product [2]. Periodical replacement is required with consequent maintenance downtime. New pump-design can be achieved by applying a LTTT on both surfaces, reducing friction coefficient by several order of magnitude and considerably minimising the operative costs of a plant.

3.6.3.2 Jewellery

Austenitic stainless steels are also growingly employed in jewellery and for consumer goods applications. For example the majority of watch cases and wristbands are made of austenitic stainless steels. In this case, the main purpose of a surface hardening treatment is aesthetic, by enhancing the scratch resistance. Low-temperature thermochemical treatments can also be used as a pre-treatment for a coating with low-friction coefficient such as diamond-like carbon (DLC), increasing adhesion and load bearing capacity.

3.6.3.3 Biomedical

Prosthesis in biomedical applications are often made of austenitic stainless steel. With a growing trend of replacing Ni with Mn for biocompatibility reasons, or Co-Cr alloys, SS are cheaper alternatives to Ti-alloys [106,107]. Decreased wear rates through expanded austenite

formation can significantly reduce risk of metal ions release into the human bodies, thus reducing potentially toxic effects. At the same time, improved wear resistance decreases the necessity of implant replacement.

4 Experimental techniques

4.1 Sample preparation

4.1.1 Sample preparation prior to thermochemical surface treatment

Prior to nitriding (Paper I and Paper III), 304L and 904L plates were initially cut into $65 \times 65 \times 3$ mm coupons. One side of the coupons was ground and polished until $3 \mu\text{m}$ diamond paste to obtain a mirror-like surface. Another surface was left with the original surface finish, which was named 2B (cold rolled, heat treated, pickled and skin passed) for 304L and 2E (cold rolled, heat treated and mechanically descaled) for 904L [108]. For plasma nitriding (PN) it is generally more convenient to treat “large” parts (e.g. shafts), since they have to be electrically connected to the power supply and should not be in contact with each other in order to achieve a homogeneous treatment on the surface. Treating larger samples also minimises “edge effects”, by decreasing the risk of electric arcs. However, several analytical instruments used in this thesis study (e.g. SEM, XRD, XPS, GDOES) require a relative small sample size; specimens were, therefore, cut afterwards from the larger nitrided coupons.

Two sets of samples were prepared prior to the low-temperature carburizing (LTC). In Paper II and Paper IV, 304L and 904L coupons were cut into $10 \times 10 \times 3$ mm and one face was subsequently ground and polished until mirror-like using $1 \mu\text{m}$ diamond suspension. For Paper V, VI, VII, all materials (304L, SS2343, 904L, 254SMO and 353MA) were initially cut into $60 \times 60 \times 3$ mm coupons. All the samples were ground and polished on one side until mirror finish, with $1 \mu\text{m}$ diamond paste as the final step. A thorough plain grinding step was critical to ensure the removal of surface deformation layer from the materials, especially those having a 2B surface finish (904L and 353MA). Gas carburizing techniques do not have particular size constraints, and small parts (e.g. springs) can also easily be treated. The smaller carburized samples could therefore be used without further preparation for most of the subsequent characterisations.

4.1.2 Sample preparation after thermochemical surface treatment

Preparation of cross-sectioned samples was necessary to assess the thickness of expanded austenite by means of either light optical microscopy (LOM) or backscattered electron imaging using scanning electron microscopy (SEM). In all cases, cross-sections were mounted on conductive resin and polished until mirror finish using SiC papers, followed by three steps of diamond suspension ($9 \mu\text{m}$, $3 \mu\text{m}$ and $1 \mu\text{m}$ particle size) and colloidal silica suspension as the final step (OP-S or OP-U).

4.1.2.1 Preparation of cross-sections for EBSD

Nickel plating was performed before the preparation of cross-sections from carburized coupons in Paper IV, in order to retain a sharp edge. In particular, this was required for material characterisation with EBSD, since the polishing step using extended silica suspension (OP-U) could have compromised the edge sharpness. Electroplating was performed by immersing the coupons in a 20-25% NiSO_4 -10% NiCl_2 electrolytic solution for 60 min at a controlled

temperature of 48°C and a constant voltage of 2.9 V between the substrate and the Ni plate used as the anode.

4.1.2.2 Chemical etching

No additional chemical etching was used for the preparation of cross-sections of PN samples in Paper I and Paper III. A 1 µm diamond paste and silica suspension (OP-S) polishing step were sufficient to reveal the expanded austenite-bulk interface by electron and optical microscopy, respectively.

On LTC materials (Papers II, IV, V, VI and VII), however, the contrast between expanded austenite and substrate on cross-sections was not sufficient to effectively reveal the carburized layer by optical microscopy or SEM. Electrochemical etching (Paper II) with 10% oxalic acid stirred solution was then used. A platinum electrode acted as a cathode and 8 V potential was applied for one minute. However, electrochemical etching was too aggressive in removing secondary phases, such as δ-ferrite, MnS or carbides, whenever present. Therefore, in Papers IV, V and VII, Marble solution (25 mL H₂O, 25 mL HCl and 5 g CuSO₄) was applied by dipping the mounted samples at room temperature for 5 to 40 s. To identify the surface carbides in Paper VII, colour etching by Groesbeck solution (25 mL H₂O, 1 g NaOH, 1 g KMnO₄) was also performed by immersing the samples for 3 to 10 minutes in the solution at ~ 60°C.

4.1.3 Sample preparation for electrochemical studies

Materials for electrochemical studies in Paper V were cut into circular samples with 11 mm diameter by waterjet cutting from 60 × 60 × 3 mm as-received and carburized plates, protected with a plastic film. Slight polishing with 1 µm diamond suspension was performed afterwards in order to reduce the surface roughness and remove possible carbides present at the surface. The backside of the samples was also ground and polished until 1200# grit using SiC abrasive paper to assure the same contact condition with the connecting electrode. After electrochemical tests, the samples were rinsed with ethanol and dried with hot-air.

4.1.4 Sample preparation for pin-on-disc testing

As-received and carburized 30 × 30 × 3 mm plates were used for tribological testing in Paper VI. The untreated samples were ground and polished prior to testing to achieve a similar surface roughness of the carburized ones ($S_a < 0.3 \mu\text{m}$). Finally, all the samples were cleaned by acetone.

4.2 Optical microscopy studies

Light optical microscopy (LOM) is a primary technique for studying the microstructure of steels. In this work, Leica, LEITZ DMRX and Olympus GX51 (Paper III) microscopes were used in order to investigate the effects of LTTT on the topography and microstructure of all investigate materials (e.g. Fig. 11).

LOM was also used to measure the thickness of γ_C and γ_N layer on cross-sections. Optical profiler WYKO Rough Surface Tester Light Interferometer was used to evaluate the change in surface roughness caused by lattice expansion due to the formation of expanded austenite.

4.3 Scanning electron microscopy (SEM)

Scanning electron microscopy (SEM) has been of paramount importance in materials science thanks to the small wavelength of the electron beam, which offers significantly higher spatial resolution compared with LOM. In addition, backscattered electron imaging provides composition contrast on different phases present in the material without etching procedure.

In SEM, electrons are generated by a source (tungsten, LaB₆ or field emission gun) and accelerated through apertures at potential of several keV. The electron beam is then collimated and focused by means of several electromagnetic lenses and is scanned on the specimen. High vacuum is necessary to increase electron mean free path, allowing high resolution [109].

The electron beam interacts with matter producing a number of signals that can be detected by different detectors. Secondary electrons are generated by ionization of the atoms composing the material. Having low kinetic energy, they can only escape from the depths in the order of ~ 100 nm (Fig. 12), providing valuable information on the topography. Backscattered electrons, instead, result from the elastic scattering of the primary electron beam, being highly energetic. The information volume is therefore larger and corresponds to $\sim 1 \mu\text{m}$. The backscatter yield is dependent on the atomic number of the elements present in the material. Heavy elements backscatter electrons more strongly than light elements, therefore providing composition contrast. This effect was used in this study to measure the thickness of N-stabilized expanded austenite.

X-rays are generated as a consequence of electrons decaying to fundamental state after ionization, characteristic for each element and dependent on primary electron beam energy. These X-rays come from an interaction volume that provides the lateral resolution of $\sim 1 - 10 \mu\text{m}$, depending on the energy of the incident beam. Energy-dispersive X-ray spectroscopy (EDS) uses such X-ray signal for chemical composition analysis.

A significant part of the characterisations in this study was performed using a FEG-SEM Leo Gemini 1550 for high resolution imaging, with Oxford Inca and Aztec (EDS) systems for chemical analysis and electron backscatter diffraction (EBSD) using Oxford Nordlys. In Paper III, however, another analytical microscope (JEOL JSM-6010 PLUS/LA) was also used for imaging and EDS analysis.

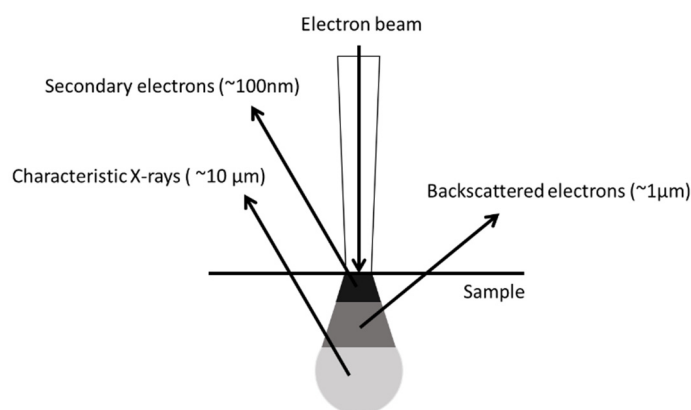


Figure 12 Schematic electron beam-sample interaction volume and signals generated in SEM.

4.3.1 Electron backscattered diffraction (EBSD)

Electron backscattered diffraction (EBSD) is a powerful characterisation technique integrated on SEM systems that gives both crystallographic and microstructural information with high spatial resolution. The backscattered electron beam (see section 4.4) interacts with a crystalline material and diffraction cones are generated, which is detected by a fluorescent screen and recorded with a camera. Analysis of cone arcs (Kikuchi lines) patterns allows for example to identify the crystal structure, orientation, presence of texturing in the material and study the grain boundaries [110].

Among the many applications of EBSD, in this work we focused on phase identification, strain analysis through average local misorientation maps [111] (Paper IV) and determination of orientation relationship (OR) between phases (Paper VII) [112]. Electron beam accelerating voltage was chosen between 10kV and 20kV, while the step-size was varied between 50 nm and 250 nm, depending on the size of the features to be analysed. The downside of decreasing accelerating voltage and step-size is the increase in acquisition time for each map. Phase identification (Table 3) was performed using the AZtecHKL (Oxford Instruments) and Inorganic Crystal Structure Database (ICSD) databases. Note that the lattice constants for Fe_5C_2 were slightly refined to improve the mean angular deviation.

Table 3 Lattice constants of the phases used for EBSD identification in Paper IV and Paper VII.

	a (Å)	b (Å)	c (Å)	α (°)	β (°)	γ (°)	Group
bcc	2.8660	2.8660	2.8660	90.0	90.0	90.0	$\text{Im}\bar{3}\text{m}$
fcc	3.6599	3.6599	3.6599	90.0	90.0	90.0	$\text{Fm}\bar{3}\text{m}$
Fe_5C_2	11.5630	4.5730	5.0580	90.0	97.7	90.0	C2/c
Cr_7C_3	4.5265	7.0105	12.1425	90.0	90.0	90.0	Pnma
Cr_{23}C_6	10.6595	10.6595	10.6595	90.0	90.0	90.0	$\text{Fm}\bar{3}\text{m}$

4.4 X-ray diffraction (XRD)

X-ray diffraction is probably the most commonly used analytical technique for phase identification. The working principle is based on diffraction of X-rays (Fig. 13) as described by the Bragg's law (eq. 14):

$$n\lambda = 2d \sin \theta \quad (14)$$

Where n is the diffraction order, λ is the wavelength of the X-ray source, d is the diffraction interplanar distance and θ is the diffraction angle [113].

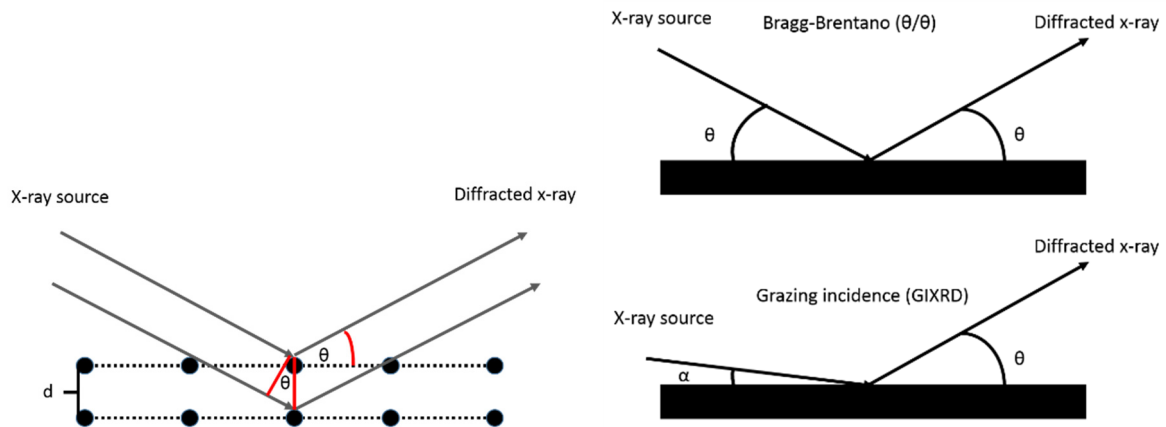


Figure 13 Left: schematic x-ray diffraction principle. Right: schematic θ/θ and grazing incidence XRD configurations.

Phase identification is performed by measuring the angles where constructive interference of X-rays is located and then converting into interplanar distance. Sets of diffracting planes are then matched with those from the standard database (Powder Diffraction Files from the International Centre for Diffraction Data).

From sets of interplanar distances it is then possible to calculate the lattice constants, which for cubic systems is a (eq. 15):

$$\frac{1}{d^2} = \frac{h^2+k^2+l^2}{a^2} \quad (15)$$

Where hkl are the Miller indexes.

The instrument employed in this work is a Bruker AXS D8 Advance system equipped with a CrK_α radiation source ($\lambda = 2.29 \text{ \AA}$) and a Göbel mirror (only in Papers I, II, III and IV). Both Bragg-Brentano θ/θ and grazing incidence (GIXRD) configuration were used. Analysis step size was chosen to be 0.05° with 5 s acquisition time. The X-ray source was operated at 35 kV acceleration voltage and 40 mA current. For Paper VII, where 1° and 3° GIXRD investigation was conducted without Göbel mirror, analysis parameters were $0.03^\circ/\text{step}$ with 15 s acquisition time.

In θ/θ configuration both source and detector move along an arc with the same angular speed, while in GIXRD the incident beam is at a fixed angle α while the detector scans along the diffraction arc (see Fig. 13). The main difference of these two techniques is the depth of information, which is limited to $\sim 1 \mu\text{m}$ for GIXRD depending on the incident angle and the material analysed. It is useful for determination of phase constituents in the near surface region at the expenses of lower counts, especially at high diffraction angles. The θ/θ configuration has to be considered as a "bulk" analysis techniques since it probes several μm in depth and the information depth varies significantly from low to high diffraction angles (90% absorption is $\sim 5 \mu\text{m}$ at $2\theta = 60^\circ$ and $\sim 10 \mu\text{m}$ at $2\theta = 130^\circ$ as calculated by AbsorbDX software using the chemical composition of 904L).

4.5 X-ray photoelectron spectroscopy (XPS)

X-ray photoelectron spectroscopy is a surface sensitive technique for chemical analysis having a depth of information up to about 10 nm below the materials' surface. It is also known as "electron spectroscopy for chemical analysis" (ESCA). When used in combination with an Ar ion gun, it is possible to perform elemental concentration depth profiling. Among its advantages is the possibility of quantitative detection of almost every elements in the periodic table (excluding H and He), including light elements such as O, C or N in a metal matrix. It is also commonly used to identify the chemical state of the species present in the sample material.

The working principle of this technique is based on ionization through X-ray irradiation (Fig. 14). Photoelectrons are emitted from the core or valence levels of the atoms after interaction with X-ray photons. The kinetic energy and the intensity of the photoelectrons are measured in a spectrometer and then recorded by a detector. The binding energy, specific for each element, can be calculated using the following equation (eq. 16):

$$E_B = h\nu - E_K - \phi \quad (16)$$

Where E_B is the binding energy, $h\nu$ photon energy, E_K kinetic energy and ϕ work function of the instrument [114].

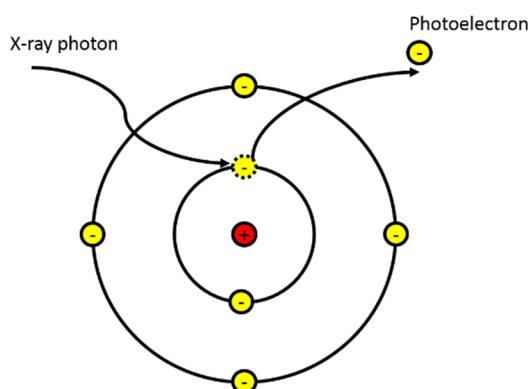


Figure 14 Schematic of X-ray photoemission process.

XPS analysis must be performed under ultra-high vacuum conditions ($< 10^{-8}$ mbar) in order to minimize the scatter of photoelectrons and avoid contamination of the analysed surface. Survey spectra acquisition with large pass energy are used for general chemical composition analysis.

High energy resolution spectra of specific core levels from elements of interest using relatively small pass energy allow identification of chemical state.

Notably, argon ion etching necessary for depth profiling may induce a progressive chemical and structural damage on the material. Preferential etching (usually of light species), increased micro-roughness and even change of chemical state are common artefacts and need to be considered when performing depth profiles.

In this study, the analyses were done using a PHI5500 spectrometer (Paper I and Paper II), having a monochromatic AlK_{α} X-ray source ($h\nu = 1,486.6$ eV). Experimental conditions were 93.9 eV pass energy with step size 0.4 eV/step for survey spectra, while the pass energy was 23.5 eV for high resolution spectra with 0.1 eV/step. Additionally, a Versaprobe III from Physical Electronics was used in Paper V and Paper VI, with 55.0 eV pass energy for high-resolution spectra. In all cases the take-off angle was 45° .

The XPS was used to determine the chemical composition in the near-surface regions (Paper VI) and the thickness of passive layers (Paper V). It was also applied for determining different chemical-bonding characteristics of Cr-N interactions in Paper I. In these cases, to remove surface contamination without altering the chemical nature of the species significantly, short time etching using a low energy argon ion beam (1 or 2 keV) was applied.

4.6 Auger electron spectroscopy (AES)

Auger electron spectroscopy is a surface sensitive chemical analysis technique, characterised by high spatial resolution and high chemical sensitivity to light elements [115]. The working principle is similar to that of an SEM with EDS, where an electron beam is shined on the sample in order to eject secondary electrons from the core levels. The atoms are, therefore, in an excited state. Subsequently, the de-excitation process via demotion of an electron from a higher energy state occurs. The excess of energy is released in form of X-ray emission (EDS) or ejection of Auger electrons (Fig. 15). The kinetic energy (E_K) of Auger electron which can be expressed approximately in the following equation (Eq. 17):

$$E_K = E_{B1} - E_{B2} - E_{B3} - \phi \quad (17)$$

Where E_{B1} and E_{B2} are the binding energies of the secondary electron and of the demoted electron, respectively, E_{B3} is the binding energy of the Auger electron and ϕ is the work function of the instrument. As observed from Eq. 17, E_K is not dependent on the energy of the incident electron beam. Instead, it is specific for a certain de-excitation process of the element.

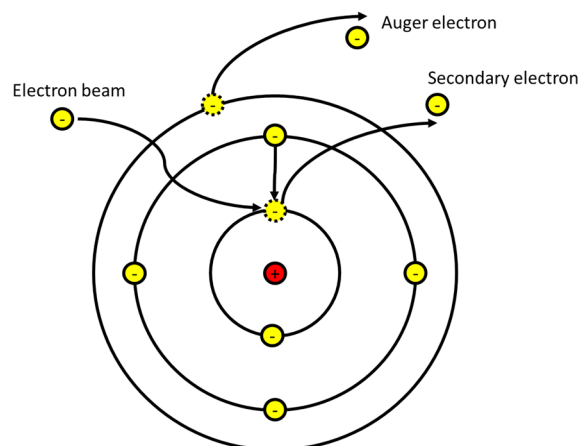


Figure 15 Schematic of Auger electron emission process.

The high spatial resolution is given by the possibility to focus the incident electron beam to small spot sizes via electromagnetic lenses, conferring a lateral resolution in the order of ten nanometre. At the same time, the mean-free path of emitted electrons is in the order of a few nanometres. The drawbacks of this technique when compared with XPS are the low emission yield of Auger electrons (being result of three electronic transitions) and lower chemical-state sensitivity [116]. On the other hand, it is possible to obtain electron micrographs with high spatial resolution by means of a secondary electron detector, thus combining imaging and chemical analysis. Additionally, depth profiling can be performed by alternating argon etching and collection of spectra.

In this study, a PHI 700 Scanning Auger electron spectroscopy (AES) instrument was used in Paper V and VII to characterise the chemical composition of small carbides particles ($< 1 \mu\text{m}$). The used electron accelerating voltage was 10 kV, with 10 nA beam current. Argon ion sputtering was used for surface cleaning and depth profiling.

4.7 Glow-discharge optical emission spectroscopy (GDOES)

Glow-discharge optical emission spectroscopy (GDOES) is a destructive chemical analysis technique routinely used for time efficient concentration depth profiling of relatively thick layers or coatings (several tenths of μm). Another advantage of GDOES is the high sensitivity to both light and heavy elements.

A voltage is applied between an electrode and the sample (cathode) in order to trigger a plasma discharge in an inert gas (usually Ar) at low pressure, as shown in Fig. 16. Sputtering processes progressively remove atoms from the sample. Atoms ejected interact with the plasma and then emit characteristic X-photons which pass through a monochromator and finally are collected by photomultipliers. By analysing the electric signal generated, quantitative information of material composition is obtained.

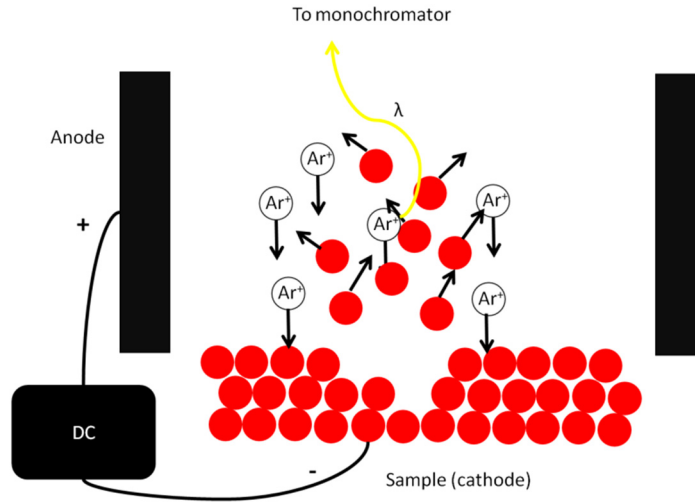


Figure 16 Schematic working principle of glow-discharge optical emission spectroscopy (GDOES).

The instrument used in this work is a Spectruma GDA750HP equipped with a DC source and a 2.5 mm diameter brass anode. The glow was obtained in Ar (5.0 purity) with an average pressure of 500 Pa. The average erosion rate was 0.0875 $\mu\text{m/s}$, which was determined experimentally by measuring the crater depth using a stylus profilometry (KLA-Tencor Alpha step profilometer). Optimized depth resolution was confirmed by the flat crater which had small roughness ($R_a < 1 \mu\text{m}$ at depth of 35 μm).

Semi-quantitative depth profiles were obtained assuming a constant elemental emission yield and a linear relationship between concentration and emission intensity. Atomic concentration of C measured by XPS after contamination removal on carburized 904L in our Paper II was taken as the reference for the quantification.

4.8 Hardness measurements

Hardness is not an intrinsic material property but is dependent on a series of factors such as stiffness, ductility, strength, toughness and viscoelasticity. A large variety of hardness measurements techniques are available. For characterization of metallic materials, the most widespread are the so called “indentation techniques”.

In general, indentation techniques measure the resistance of a material to local plastic deformation induced by an indenter, having a known geometry at a specific applied load (L) kept for certain time. For Vickers hardness, a squared base pyramid indenter having angle of 136° is employed and the hardness is calculated by dividing the load with the area of indentation as follows (eq. 18):

$$HV = \frac{L}{A} = \frac{2 \sin\left(\frac{136^\circ}{2}\right) L}{d^2} \quad (18)$$

Where d is the average diagonal of the indentation.

While hardness measurements are conventionally performed on the surface of the specimen, this is not recommended for LTTT austenitic stainless steels for several reasons. First of all,

after low-temperature carburizing/nitriding procedure, surface roughness increases to the point that indentations have an irregular shape thus compromising the quality and repeatability of the measurement. Secondly, it is very likely that a certain contribution of the substrate will emerge since strain field extends in average about ten times the depth of the actual indentation. Moreover, this contribution will be dependent on the applied load and on the holding time. Hardness was measured directly on the surface of carburized specimens only in Paper VI, the purpose then was to evaluate the material response during pin on disc tests at different loads.

To further reduce the strain-field volume and achieve higher spatial resolution, nanoindentation is a promising technique. In this case the applied load can be much lower (nN) and hardness is calculated in real time from the load-displacement curve recorded by the instrument.

For the reasons mentioned above, together with the relatively small thickness of hardened case layer (20 – 30 μm), hardness profiles from both microhardness testing and nanoindentation were obtained on polished cross-sections. The distance between indentations ($> 3d$) follows ASTM E384/ISO 6507-1 standards, in order to avoid interaction of deformation field. However, the distance from the edge of the sample could not always be assured owing to the geometry limitation of the samples. The nanoindentation measurements together with local misorientation maps, which represent strain levels in the material, helped to identify the hardening mechanisms in Paper IV.

The microhardness was measured for γ_c both on top surface (Paper VI) and on cross-section at different depth (Paper II) using a Shimadzu HMV-2000 ($L = 10 \text{ gf}$, $t = 10 \text{ s}$). The size of the indentation was measured using an optical microscope. The nanoindentation depth profiling in Paper IV was performed with a CSIRO UMIS equipped with a Berkovich tip ($L = 5 \text{ mN}$, $t = 10 \text{ s}$). In paper III, Knoop hardness (asymmetric pyramid indenter) was obtained on the cross-sections of the nitrided layers using a Matsuzawa MMT-X7 ($L = 10 \text{ gf}$, $t = 10 \text{ s}$).

4.9 Pin-on-disc testing

Pin-on-disc tests in Paper VI were performed on a CSM Instruments compliant to ASTM G99 standard in order to evaluate the tribological behaviour, coefficient of friction and wear modes, of as-received and LTC materials (see Fig. 17). The coefficient of friction (CoF or μ) is defined as the ratio between applied load (N) and frictional force (F), as shown in Eq. 19.

$$CoF = \frac{F}{N} \quad (19)$$

The tribometer is composed of an electric motor coupled to a sample holder and a stiff cantilever connected to a rod where the counter material is mounted. On top of the cantilever, a weight is added to set the specific load. The instrument records the friction coefficient between the sample and the counter-material in real-time, by constantly measuring the deflection of the cantilever, which is proportional to the frictional force. Pin-on-disc tests are not directly representative of real applications but are commonly used to compare the tribological behaviour of materials. For a higher technological relevance, the actual environmental conditions should be controlled and replicated.

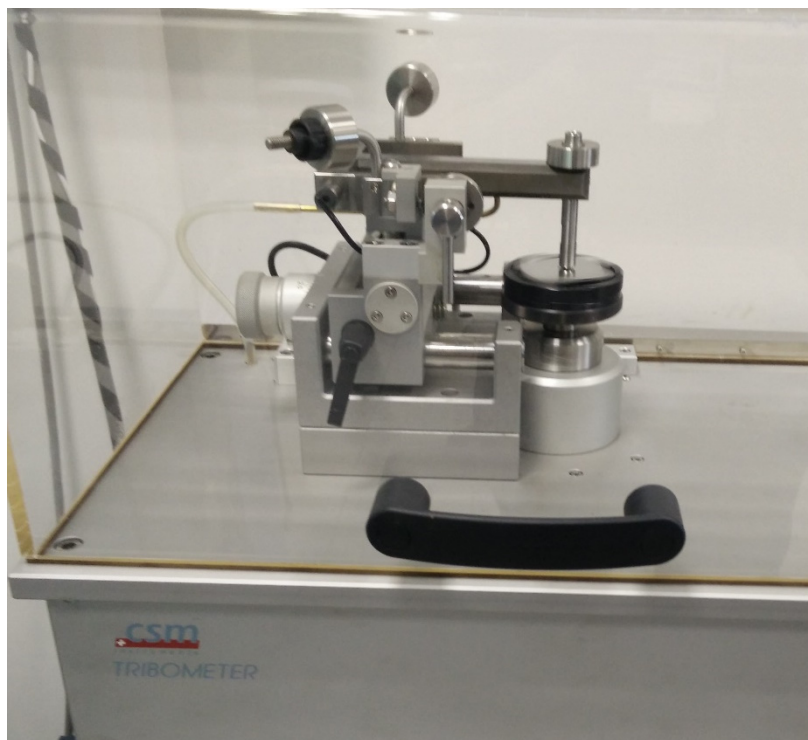


Figure 17 CSM Instruments tribometer used in Paper VI.

The counter-material used for the tests was an Al_2O_3 ball of 6 mm diameter and all the tests were run at a constant linear speed of 0.05 m/s at load of 0.5 N, 1.5 N and 3.0 N with an increasing radius of 2 mm, 6 mm and 10 mm. Such low loads were chosen in order not to incur in “thin ice” effects. The total worn volume for each wear test was calculated by integrating the area delimited by the crater profile measured by a stylus profiler (Surfscan 3D, Somicronic) over the track length. Pin-on-disc tests were performed in dry-sliding condition and in simulated sea-water environment (60 mL of 3.5 wt% NaCl solution).

4.10 Potentiodynamic and potentiostatic measurements

Potentiodynamic and potentiostatic measurements are conventional electrochemical tests for evaluating the corrosion behaviour of materials in a certain environment. The set-ups typically consist of three electrodes: the working electrode (material to be tested), the counter electrode and the reference electrode. All the electrodes are immersed in a solution representing the real environment of application (e.g. 3.5 wt% NaCl to simulate sea-water). In potentiostatic measurements, a determined potential is applied between the working electrode and the reference electrode, which is electrically insulated by a salt bridge. The electrical current is allowed to flow between the working electrode and the counter electrode, and is recorded over time.

In potentiodynamic testing, instead, the applied potential is usually swept between a range of values below and above the open-circuit potential (OCP, also called corrosion potential, E_{corr}) and a polarisation diagram is drawn (Fig. 18). This type of diagrams is particularly useful for evaluating the corrosion behaviour of passivating materials, such as stainless steels. Some important electrochemical characteristics are the corrosion current (I_{corr}), the corrosion potential

(E_{corr}), the critical corrosion current (I_{crit}), the passivation potential (E_{pass}), the passivation current (I_{pass}) and the transpassive potential (E_{trans}), as shown in Fig. 18.

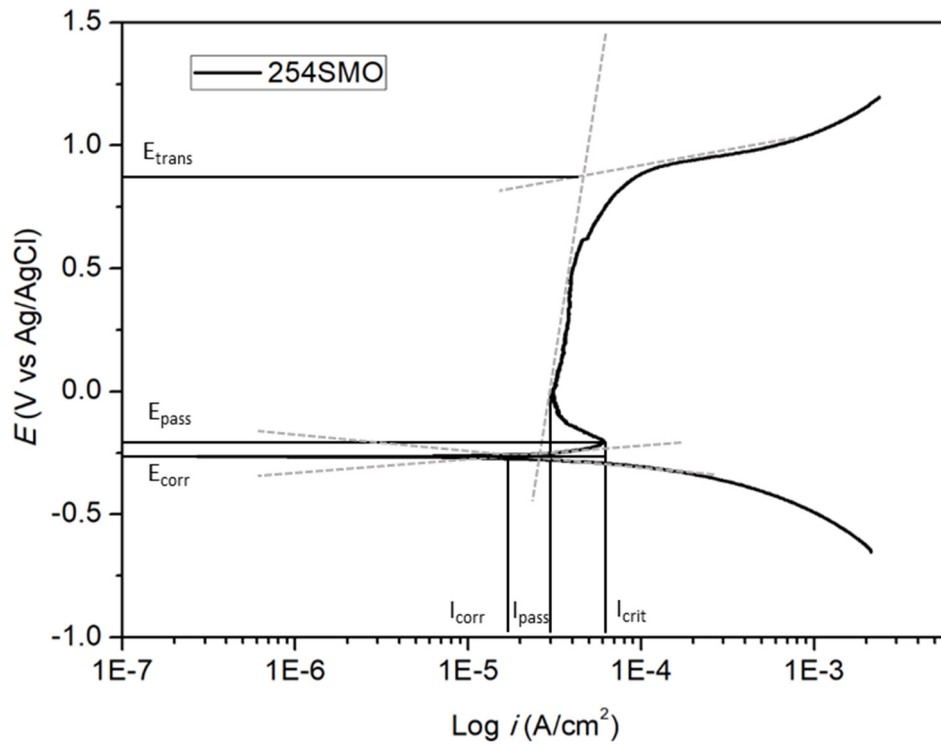


Figure 18 Polarisation diagram of a material exhibiting passivation (254SMO) with highlighted electrochemical characteristics (from Paper V).

In Paper V, the corrosion behaviour of as-received and LTC materials was tested in a 0.1 M H_2SO_4 with 2 ppm of NaF at $75 \pm 5^\circ C$ to simulate the cathodic environment of a used polymer electrolyte membrane fuel cell (PEMFC). A schematic set-up used in this study is given in Fig. 19. The specimens were prepared according to section 4.1.3 and only the top-surface was exposed for corrosion testing. For potentiodynamic testing, the potential was set with a Solartron Electrochemical Interface (SI 1287) between -0.7 V to 1.2 V with respect to Ag/AgCl standard reference electrode to cover both the anodic and cathodic side of the polarisation curve. The sweeping speed was 10 mV/s. For potentiostatic testing, a voltage was set at 0.630 mV vs Ag/AgCl and the current was recorded for 5000 s. All measurements were performed in three replicates to assure consistency of the results.

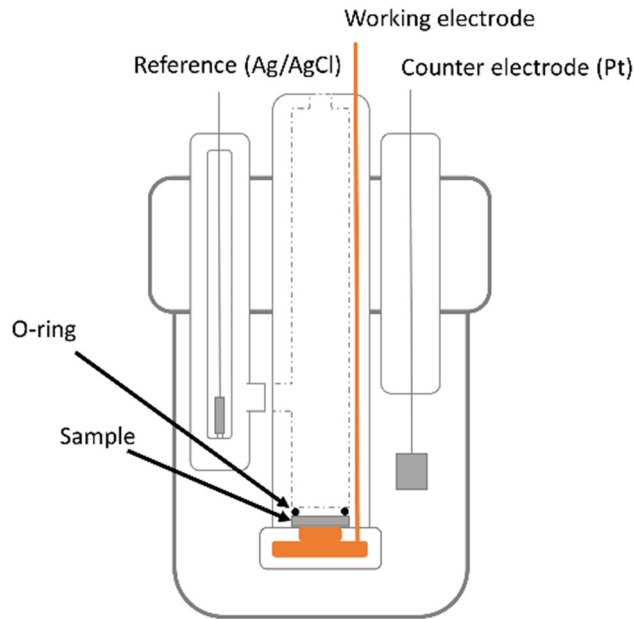


Figure 19 Schematic of three-electrode set-up for polarisation measurements (from Paper V).

4.11 Interfacial contact resistance (ICR) measurements

Interfacial contact resistance (ICR) refers to the out-of-plane electrical resistance across two different materials and is related to the morphological and chemical nature of the interface between them. In Paper V, we evaluated the change in ICR between austenitic stainless steels and a carbon-paper, in as-received and LTC conditions, before and after a potentiostatic polarisation (to simulate a “chemical ageing” of the surface). As ICR is dependent on the compaction pressure [117], a testing rig was constructed adapting a Zwick Z2.5 universal testing machine (2 kN load cell) to replicate Wang’s method [118] as schematically drawn in Fig. 20.

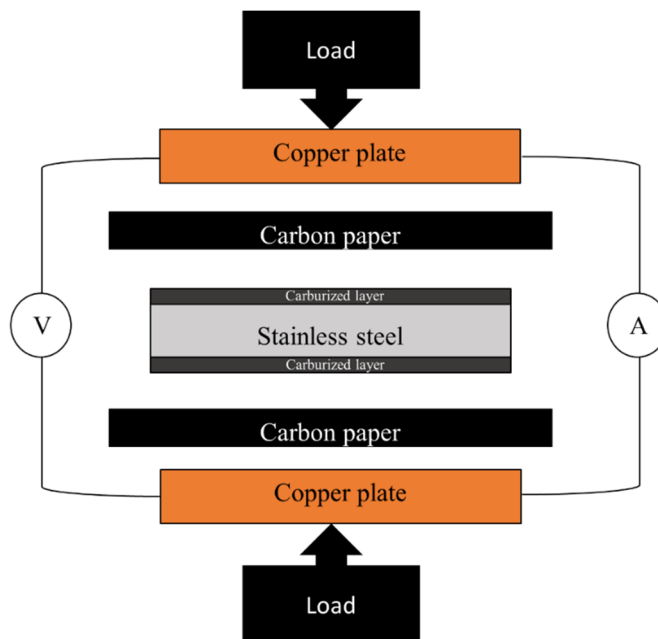


Figure 20 Schematic of interfacial contact resistance (ICR) testing rig (from Paper V).

A direct current (I) of 1.0 A was applied through the stack. Assuming all the bulk resistances are negligible compared with the contributions from the interfaces [118], ICR can be calculated by measuring the potential drop V , as indicated in Eq. 20, where R is the measured resistance and A is the surface area. Subtracting the interfacial resistance between two copper plates and a carbon-paper (“calibration resistance”, R_{CAL}) from R , ICR between the stainless steel samples and the carbon-paper ($ICR_{SS/C(new)}$) is obtained, as shown in Eq. 21.

$$R = \frac{VA}{I} \quad (20)$$

$$ICR_{SS/C(new)} = \frac{R - R_{CAL}}{2} \quad (21)$$

The ICR of the chemically aged surface ($ICR_{SS/C(aged)}$) was calculated similarly, by subtracting the contribution from the “new” (non-aged) surface from measured R , as exhibited in Eq. 22. The same procedure was applied for the LTC materials.

$$ICR_{SS/C(aged)} = R - (R_{CAL} + ICR_{SS/C(new)}) \quad (22)$$

The compaction pressure was varied between 200 and 10 N/cm² after an initial conditioning of the carbon-paper at 250 N/cm² to simulate the typical compaction pressure of a PEMFC.

5 Summary of results and discussion

This thesis is the result of the work carried out in the last five years, which led to the seven appended papers. Each paper has its own research focus which contributes to the research objectives listed in section 1.2.

- In Paper I, the nitrified layer formed by industrial low-temperature plasma nitriding on 304L and 904L austenitic stainless steels was examined. How surface finishing prior to nitriding, alloying elements and nitriding conditions affect the microstructure of the nitrified layers was focused. The chemical bonding characteristics of Cr 2p_{3/2} and N 1s was also investigated.
- In Paper II, 304L and 904L stainless steels were subjected to Kolsterising low-temperature carburizing treatment. The resulted microstructure, phase constitution, surface chemistry and thermal stability as well as hardening effect were investigated by means of a broad spectrum of characterisation techniques.
- In Paper III, the thermal stability of N-expanded austenite in 304L and 904L during isothermal annealing in protective argon atmosphere at temperatures between 450 and 600°C was assessed. The related phase evolution, the decomposition mechanisms of expanded austenite as well as the hardening behaviour of γ_N in 304L and 904L were evaluated and discussed.
- In Paper IV, EBSD was used, together with other techniques, to characterise the microstructure and to determine the hardening mechanisms in low-temperature carburized 304L and 904L. The influence of surface finish was also investigated. Additionally, the thermal decomposition mechanisms/route of γ_C as a function of composition of the steels and their surface finish were identified. Redistribution of C and precipitation of carbide were examined as well.
- In Paper V, the effects of alloy composition on the formation and electrochemical properties of γ_C were evaluated. In particular, the roles of Ni and Mo were systematically studied through microstructural characterisation of five LTC austenitic stainless steels (304L, SS2343, 904L, 254SMO and 353MA). Additionally, the potential applicability of LTC in materials for energy-applications was explored.
- In Paper VI, the effects of LTC treatment on the tribological properties of metastable 304L and superaustenitic 904L were investigated. The main wear mechanisms were determined in dry and simulated sea-water environment. The effects of LTC treatment on the surface chemistry of the wear track were analysed.
- In Paper VII, metallographic, electron microscopic and spectroscopic techniques were used to identify the surface carbides found on carburized AISI 304L and SS2343. Orientation relationships between carbides and expanded austenite matrix were confirmed. A mechanism for precipitation of surface carbides during LTC was proposed.

5.1 Microstructure of low-temperature nitrided/carburized austenitic stainless steels

The surface morphology of all materials changed as a consequence of LTTTs. Firstly, surface roughness was increased. Secondly, the microstructure of the original mirror-polished surface (austenite grain structure) was revealed without need of etching in both carburized (Fig. 21) and nitrided (Fig. 11) steels. An exception was the highly nitrided P304L-H, where massive nitride formation at the surface occurred during the nitriding process (Paper I) and possibly due to thermal decomposition of the γ_N .

There are two fundamental causes for the increase in surface roughness. Firstly, in case of PN-treated materials, the anisotropic sputtering effect of the plasma increases the surface roughness [88]. Secondly, the interstitial diffusion is anisotropic, leading to anisotropic stresses which in turn gives rise to asynchronous and non-uniform plastic deformation. Consequently, the grain structure was revealed and surface roughness was increased.

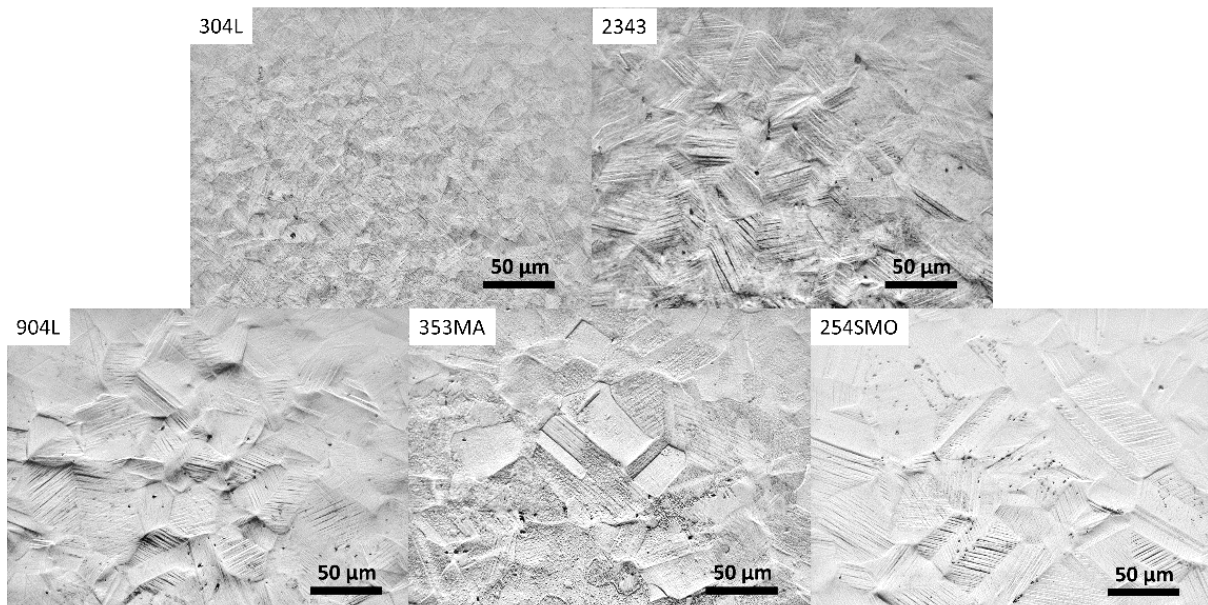


Figure 21 Surface morphology of all materials investigated in this study after LTC treatment (from Paper V).

This theory was confirmed by EBSD misorientation analysis in Paper IV (Fig. 22). The large lattice expansion induced by LTC in 904L made it possible for this technique to identify the anisotropic plastic deformation at the surface. In 304L, however, the smaller lattice expansion made the misorientation analysis less applicable. In fact, γ_C induced almost double increase in roughness as a consequence of different lattice expansion in 904L compared to that in 304L (Paper II).

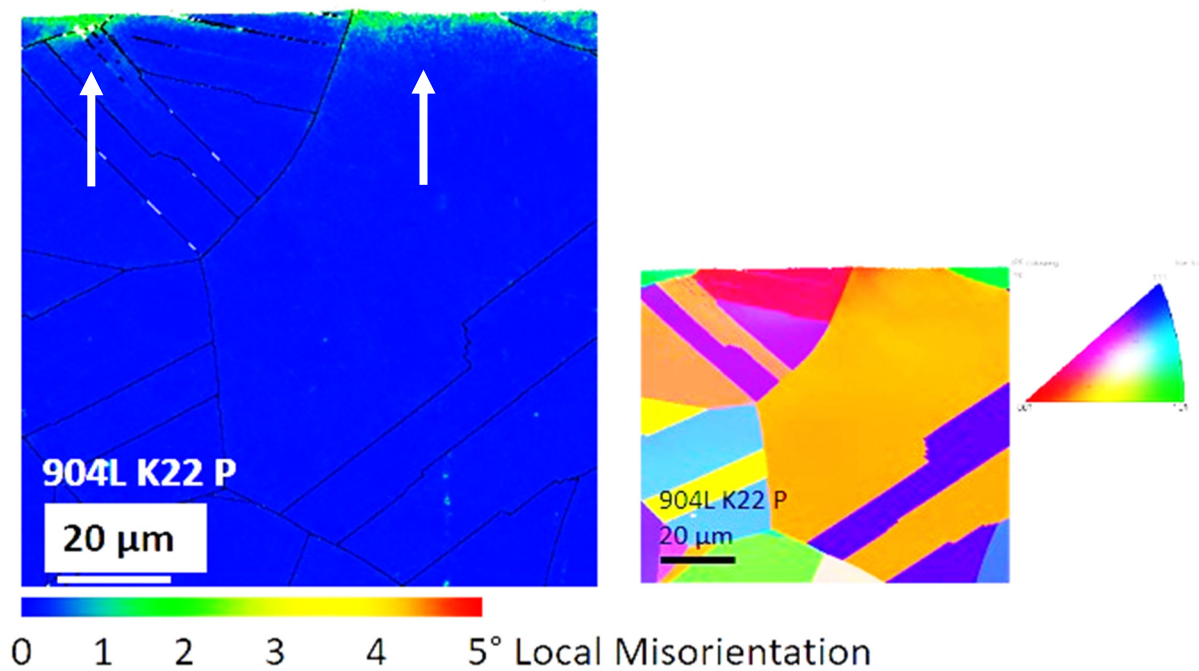


Figure 22 Left: local misorientation map in rainbow colours. Right: inverse pole figure map. EBSD measurement performed on cross-section of 904L after LTC treatment showing anisotropic deformation at the surface. The white arrows point at grains with higher surface misorientation (from Paper IV).

Moreover, in all examined steels (except again for P304L-H), slip bands and twins were observed at the surface, indicating that plastic deformation occurred by slipping or even twinning (see Papers I, II, V and VII). The effect of N on lowering stacking fault energy in austenitic stainless steel has been well known and C is supposed to have similar effects. Nitrided 904L also exhibited cracking due to high internal stresses and embrittlement of the surface caused by incorporation of large amount of N atoms (Paper I and III). None of the carburized materials showed clear signs of surface embrittlement.

5.2 Layer thickness of expanded austenite

The thickness of case hardened layer reflects the diffusion depth of interstitial species and is of great importance for applications involving load bearing. Table 4 summarizes the layer thickness of expanded austenite for PN (Paper I) and LTC (Paper II and Paper V) materials. Measurements were performed on cross-sections by means of SEM and OM. Chemical etching was used in case of LTC materials.

The thickness of expanded austenite was less uniform within PN samples (L condition) compared to that of LTC ones, probably due to inhomogeneous plasma intensity. For this reason, the relative standard deviation of average case thickness is significantly higher for γ_N compared to γ_C .

Table 4 Summary of case layer thickness for plasma nitrided (from Paper I) and carburized (from Paper II, Paper V and reference [119]*) 304L and 904L. P = polished, N/NP = non-polished. Surface concentration of interstitial atoms was measured using XPS for nitrided samples and GDOES for carburized samples.

Material and surface	Process type	Layer thickness (μm)	Surface at%
P304L-L	LTN	4.4 ± 2.0	18-21
P304L-H	LTN	39.6 ± 3.9	18-20
N304L-L	LTN	8.0 ± 0.5	14-15
N304L-H	LTN	44.1 ± 4.1	n.d.
304L K22 P	LTC	24.3 ± 1.9	11
304L K22 NP	LTC	26.9 ± 1.4	13
P904L-L	LTN	4.3 ± 0.6	9-10
P904L-H	LTN	18.9 ± 2.0	18-20
N904L-L	LTN	5.8 ± 1.0	n.d.
N904L-H	LTN	25.9 ± 3.7	n.d.
904L K22 P	LTC	24.0 ± 1.0	18
904L K22 NP	LTC	25.2 ± 1.0	21
SS2343 K22 P*	LTC	31.1 ± 0.9	13
SS2343 K22 NP*	LTC	34.0 ± 1.0	n.d.
254SMO K22 P*	LTC	30.3 ± 0.8	14
254SMO K22 NP*	LTC	30.5 ± 1.1	n.d.
353MA K22 P*	LTC	13.6 ± 0.6	11
353MA K22 NP*	LTC	12.6 ± 1.8	n.d.

For both low-temperature nitriding and carburizing, the case layer thickness and the influence of original surface finishing (rolled or sandblasted) followed similar trend. In general, larger plastic deformation leads to accelerated diffusion owing to the increased crystallographic defects, translating into thicker layers. This effect appears more prominent in PN materials. However, this was not the case for carburized 254SMO and 353MA. Kante [122] found a ~ 3 wt% Cr depletion within the first 2 μm below the non-polished surface of these two steels (the Cr depletion was not observed in other materials). This Cr depletion, possibly originating from the finishing operation of the original plate, can explain the lower interstitial mobility due to the loss of “trapping” effect (cf. Section 3.3).

Nickel and Mo, in addition to Cr, are two important elements affecting the formation of expanded austenite. A thicker expanded austenite layer is formed with increasing amount of Mo. On the contrary, a thinner expanded austenite layer is obtained with increasing amount of Ni. It is believed that Mo has an important role in facilitating interstitial diffusion through lattice expansion of the metal matrix [123], while Ni has the opposite effect due to its low affinity to N and C, acting as a hinder for interstitial diffusion [6]. Therefore, the rank of layer thickness in ascending order is 904L, 254SMO and SS2343. Interestingly, 353MA showed the thinnest layer despite large amount of Cr. Evidently, the presence of high Ni concentration counterbalances this.

5.3 Phase constituents of surface engineered austenitic stainless steels

5.3.1 Low-temperature nitriding

Plasma nitriding induced the formation of a complex compound layer on 304L surfaces (Fig. 23). Large amounts of CrN-like compounds, Fe₄N and Fe₃N were found on highly nitrated 304L (H condition), which suggests the formation of a compound layer during the nitriding process and the possible decomposition of expanded austenite throughout the layer. For the less severe nitriding condition (L), the expanded austenite surface was more stable, with a thinner compound layer. The XRD pattern of P-surface suggested the presence of expanded austenite and Fe₁₆N₂ (α'), a precursor of Fe₄N [121], within the Area 1 in Fig. 7e having thicker expanded austenite layer. Chromium nitride and “zero” lattice expansion were identified in Area 2. In case of the non-polished surface, however, no precipitate could be observed and only S-phase was clearly identified by XRD. This behaviour can be explained by the fact that the supersaturation threshold is not reached for the N-condition, owing to the fast interstitial diffusion. Moreover, deformation induced martensite formed during the sample preparation prior to nitriding (polishing) potentially acted as a preferential site for nitride formation [122].

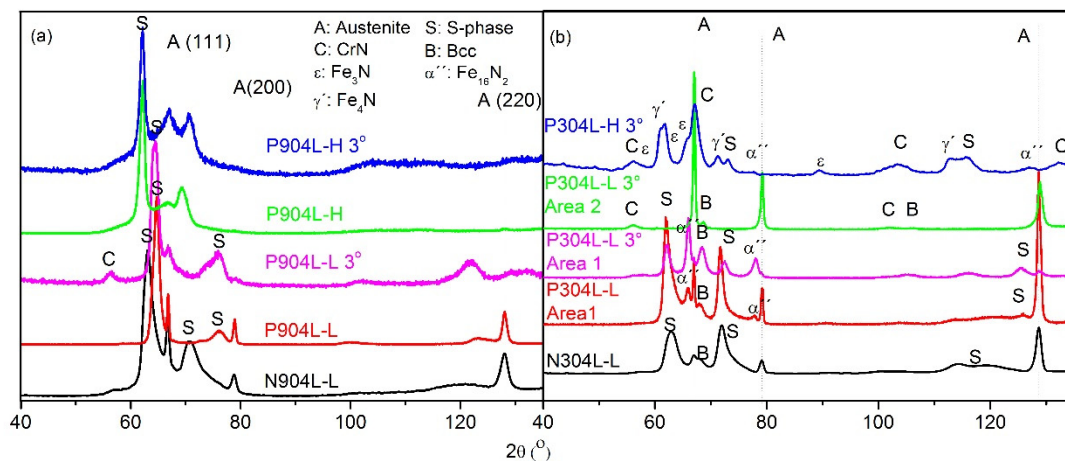


Figure 23 XRD patterns for plasma nitrided (a) 904L and (b) 304L, in high (H) and low (L) nitriding condition, for polished (P) and as-received (N) surface finish (from Paper 1).

On contrary, high alloyed 904L showed the dominant presence of expanded austenite. A very thin superficial CrN compound was detected in L condition by GIXRD analysis and in H condition by XPS depth profiling. These results confirm the theory that the thickness of the compound layer is reduced in higher alloyed steels [50].

By selectively removing the thin compound layers it was possible to evaluate the chemical bonding of Cr and N within the S-phase. The binding energies of Cr 2p_{3/2} and N 1s from expanded austenite were located at 574.5 eV and 397.3 eV respectively. With respect to CrN, Cr 2p_{3/2} and N 1s XPS peaks shift about - 0.3 eV and + 0.3 eV respectively (Fig. 24).

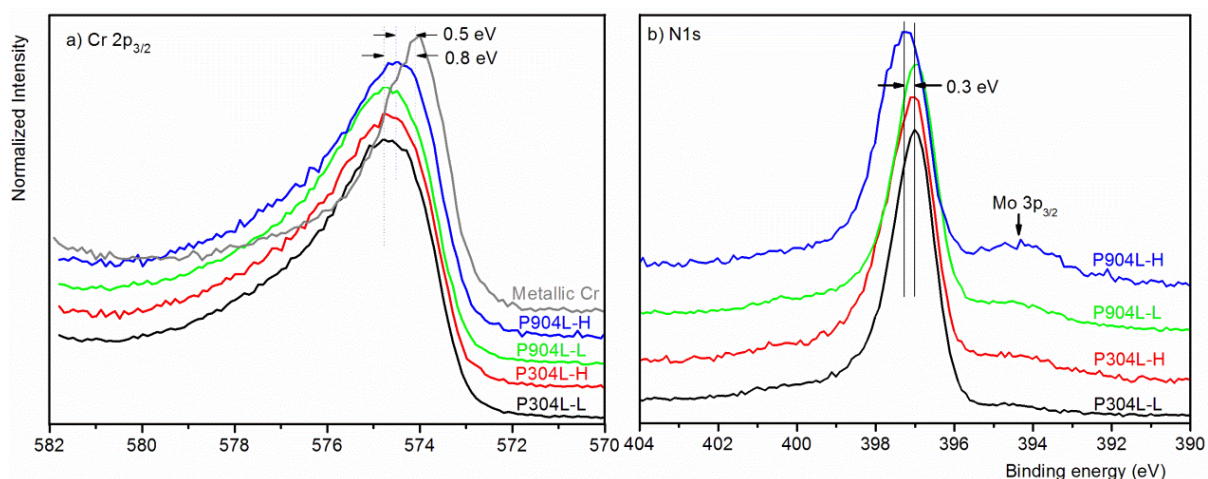


Figure 24 XPS (a) Cr $2p_{3/2}$ and (b) N 1s peaks from as-nitrided materials (from Paper I)

These results are in partial agreement with those reported by Riviere et al. [123] who found that the binding energy of Cr in S-phase was smaller than that characteristic of CrN. However, they could not distinguish between S-phase and CrN by considering N1s core level. These authors, however, used 5 keV Xe⁺ ion sputtering to remove surface contamination. Such highly energetic ions might have caused chemical modification at the surface (e.g. nitride formation during sputtering). The controlled polishing followed by 1 keV Ar⁺ sputtering, as reported in Paper I, is much more “gentle” and should have maintained the original chemical state of the species. Varied XPS peak position for both Cr $2p_{3/2}$ and N1s peak from our results confirms a different short range ordering compared to that of pure nitrides, as suggested by Oddershede et al. using EXAFS measurements [71].

5.3.2 Low-temperature carburizing

XRD studies performed on carburized steels (Paper II, IV, V, VI, VII) revealed the presence of carbides in the near-surface region of 304L and SS2343 (Fig. 25) in addition to γ_C , while only γ_C was found on 904L, 254SMO and 353MA. The χ -Hägg carbide (isomorph of Fe₅C₂) which is considered as “unusual” in austenitic stainless steels was previously reported by Cao et al. on 316L stainless steel treated by “Swagelok” process [69]. The authors initially associated its formation with the stabilizing role of Mn present in 316L. Nevertheless, Mn is present in all the studied steels with similar amount and it should be less important in this respect. Hägg carbide has been reported to be part of the catalytic reaction product when forming hydrocarbides by reacting Fe with CO + H₂ at temperatures between 200°C [116] and 420°C [117]. This is the temperature range similar to those of LTC treatments. In addition, M₇C₃ type carbides were found to form at higher temperature (T > 450°C) or longer treatment [125,126]. Although Christiansen et al. [125] claim the Hägg-carbide has the same composition as the surrounding matrix, this study (Paper VII) gave different results, which are in agreement with those of Ernst et al. [68]. In fact, Cr-enrichment and Ni-rejection were shown in all carbides precipitated during LTC treatment, even if the low-treatment temperature should limit the substitutional diffusion distance.

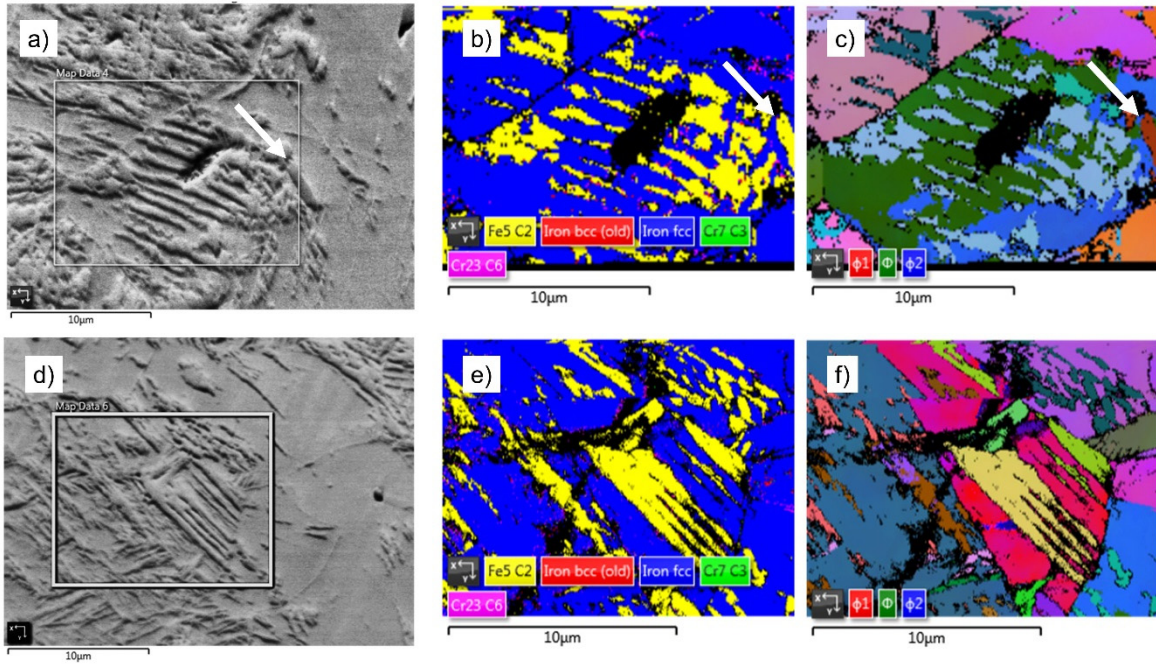


Figure 26 Forward scattered electron micrographs (a, d), EBSD phase maps (b, e) and EBSD orientation maps in Euler angle representation (c, f) of two locations at the surface of LTC 304L. All maps are presented without data refinement. The white arrows in (a, b and c) point at pre-carburizing δ -ferrite stringers (from Paper VII).

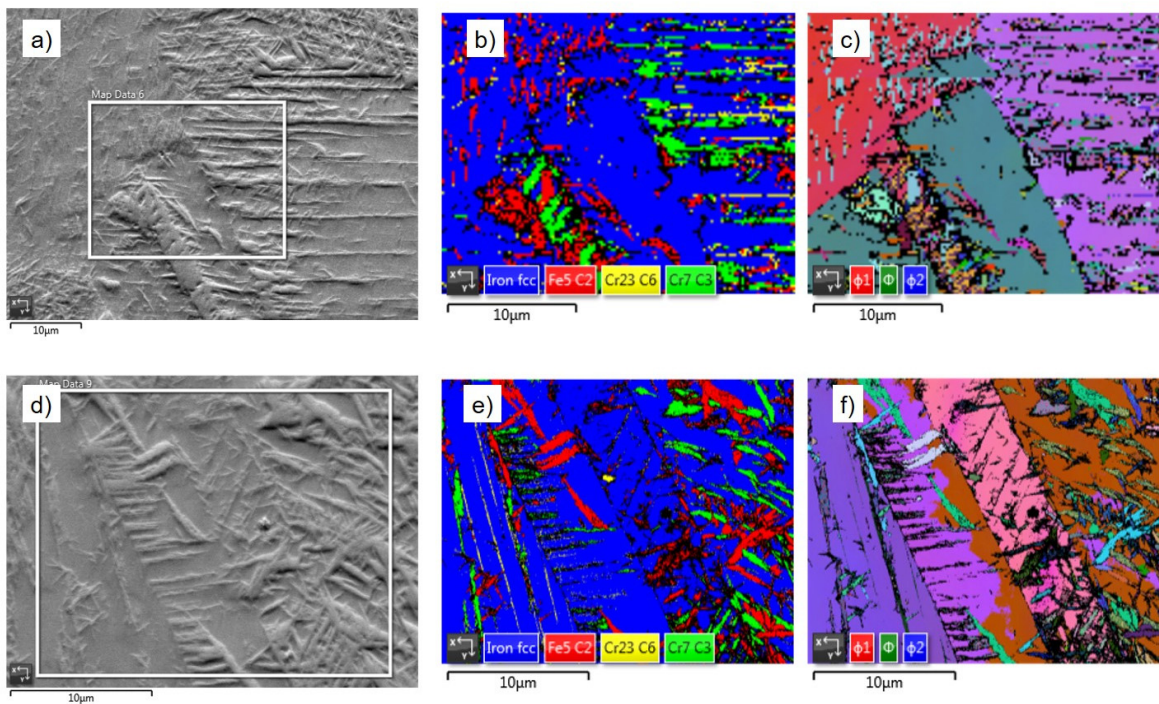


Figure 27 FSD electron micrographs (a, d), EBSD phase maps (b, e) and Euler angles orientation maps (c, f) of two locations at the surface of LTC SS2343 (from Paper VII).

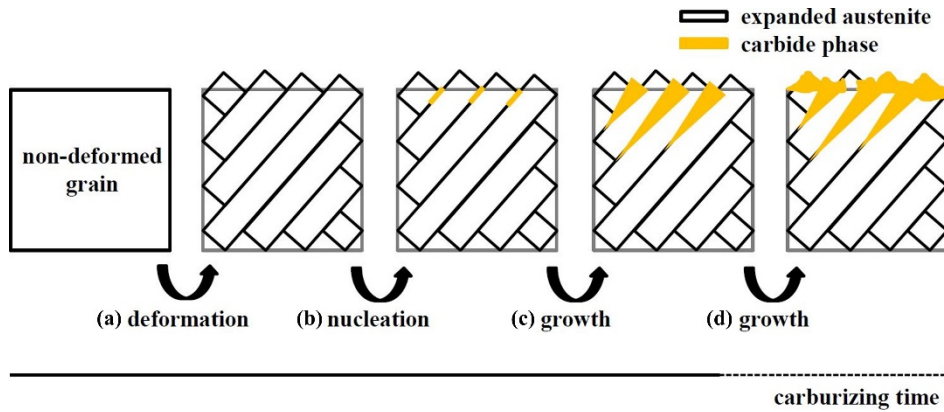


Figure 28 Hypothetic carbide precipitation mechanism during LTC in austenitic stainless steels (from Paper VII).

5.4 Interstitial content

The interstitial content in the near surface region for nitrided steels was quantified by means of XPS analysis. The concentration of N and Cr in depth profile also allowed the estimate of the thickness of the compound layer present on the surfaces. This layer can be as thick as 160 nm for 304L, while it is only a few tens of nm for 904L. Lower nitriding potential and shorter nitriding time in the L-condition caused generally lower intake of N in the austenitic stainless steel. The values of interstitial content calculated from eq. 7 and reported in Table 4 correlate well with EDS measurements (Paper III).

Carbon concentration in austenitic stainless steels treated with Kolsterising was estimated both directly and indirectly from the XRD peak shift (Paper V) and the GDOES depth profile calibrated with XPS quantification results (Paper IV in Fig. 29a and ref. [119] in Table 4). Narrow XRD peaks in 304L and SS2343 suggest a rather homogeneous carburizing within the probed depth, while 904L, 254SMO and 353MA exhibit significant broadening and asymmetry of XRD peaks. When treated in the same conditions, 904L shows a saturation threshold almost 8 at% higher compared to 304L. Non-polished surfaces consistently dissolve more interstitials due to larger pre-existing plastic deformation and consequently higher dislocation density which are supposed to increase the solubility and diffusivity [128,129,122]. Higher maximum supersaturation was found near the surface, as shown in Fig. 29a. However, in the case of carburized 904L, a steeper gradient is observed in the C concentration profile for NP condition, i.e., C concentration at larger depth is lower than that of the P condition. This can be explained as follows. Higher maximum supersaturation at the surface region lowers the probability of finding empty octahedral sites necessary for interstitial diffusion, making the further diffusion towards deeper region difficult.

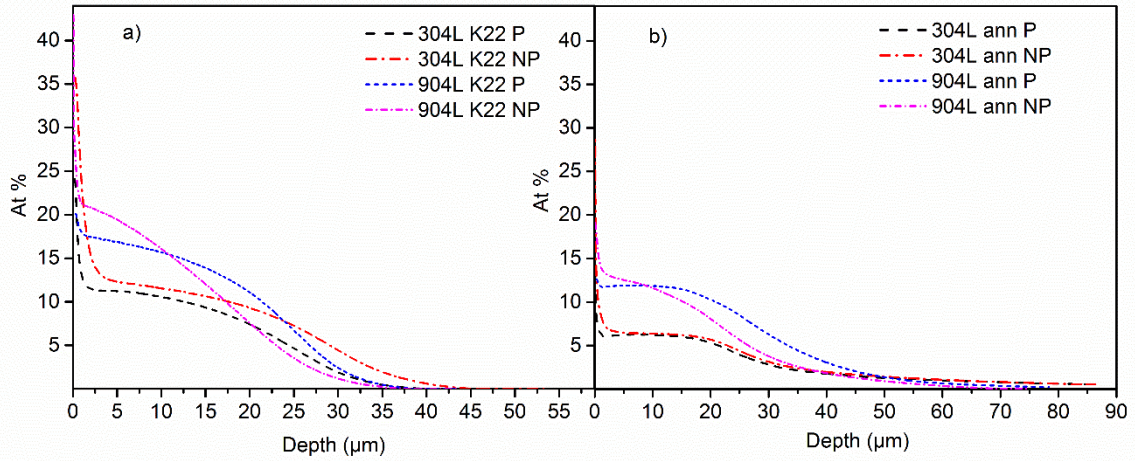


Figure 29 GDOES C-concentration profiles of (a) low-temperature carburized 304L and 904L, (b) after vacuum annealing at 600°C for 150 hours (Paper IV).

The estimation of the interstitial concentration by measuring the position of XRD diffraction lines (Fig. 30) from eq. 8 using lattice expansion constant $\alpha = 0.68 \text{ \AA}$ [130] does not always provide satisfying results. Interstitial occupancy y_C is largely overestimated in high-Mo containing materials (Table 5). One possible explanation is that interstitial lattice expansion coefficient α is not universal and cannot be used for materials with a substantially different initial lattice parameter and/or with different X-ray elastic constants. However, it holds well for the low-Mo containing steels 304L, SS2343 and 353MA (cf. Table 4).

Moreover, it is interesting to notice that the layer thickness of expanded austenite measured by means of LOM does not correspond to the one measured by GDOES depth profile. An effective threshold of interstitials seems to be necessary to cause etching contrast.

Table 5 Lattice expansion and interstitial content in LTC materials (data from Paper V)

	Lattice parameter $a_{\gamma 0}$ (Å) for raw materials	Lattice parameter $a_{\gamma C}$ (Å) for LTC materials	Lattice expansion (%)	Estimated concentration (X_C)	Interstitial occupancy (y_C)
304L	3.59 ± 0.01	3.67 ± 0.03	2.2 ± 0.8	0.12 ± 0.04	0.13 ± 0.04
SS2343	3.60 ± 0.01	3.70 ± 0.03	3.0 ± 0.8	0.16 ± 0.04	0.19 ± 0.05
904L	3.60 ± 0.01	3.79 ± 0.06	5.2 ± 1.7	0.28 ± 0.09	0.38 ± 0.12
254SMO	3.61 ± 0.01	3.82 ± 0.05	5.8 ± 1.4	0.31 ± 0.07	0.45 ± 0.10
353MA	3.59 ± 0.01	3.67 ± 0.01	2.2 ± 0.1	0.12 ± 0.01	0.13 ± 0.01

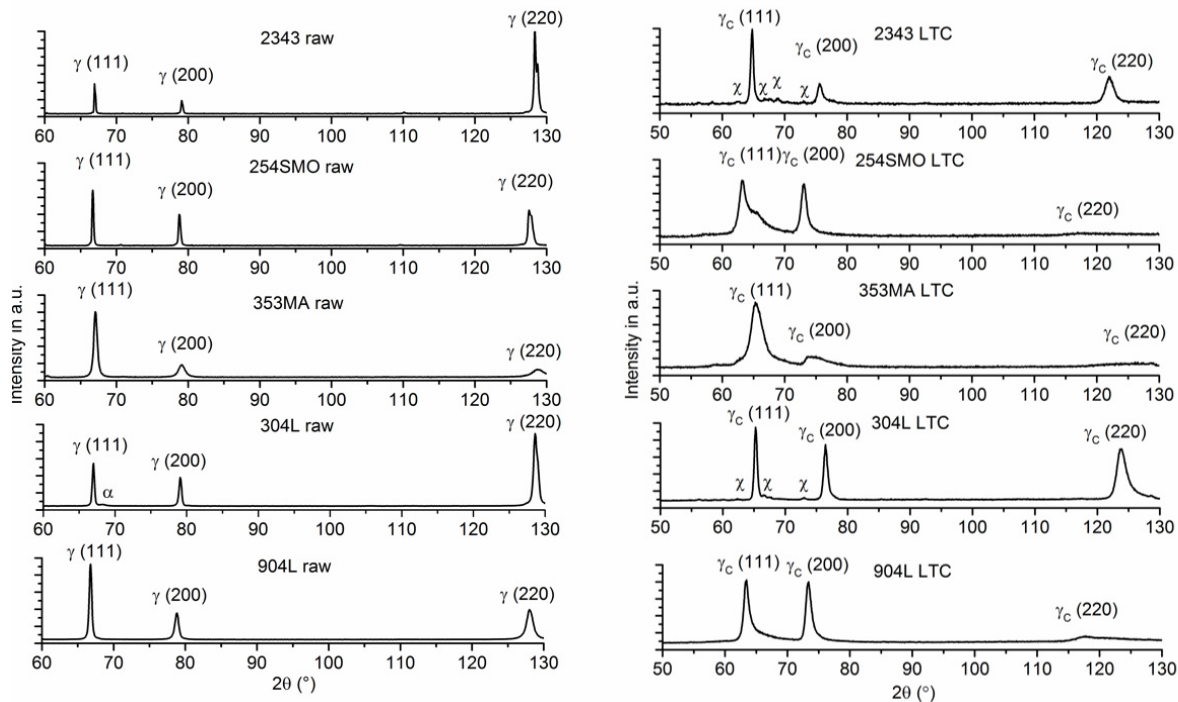


Figure 30 X-ray diffraction patterns of raw and low-temperature carburized austenitic stainless steels. γ : austenite. α : ferrite. γ_c : expanded austenite. χ : Hägg-carbide (from Paper V).

5.5 Thermal stability of expanded austenite

From all the experiments performed, it can be generalised that γ_N and γ_C are more stable in high-alloyed austenitic stainless steels. The lower alloyed 304L could not form or maintain a γ_N structure at 400°C for 99 hours (Paper I). Moreover, the complete decomposition temperature (defined as 90% reduction of lattice expansion) of γ_N during isothermal annealing is about 100°C higher for 904L than that for 304L (Paper III) (Fig. 31).

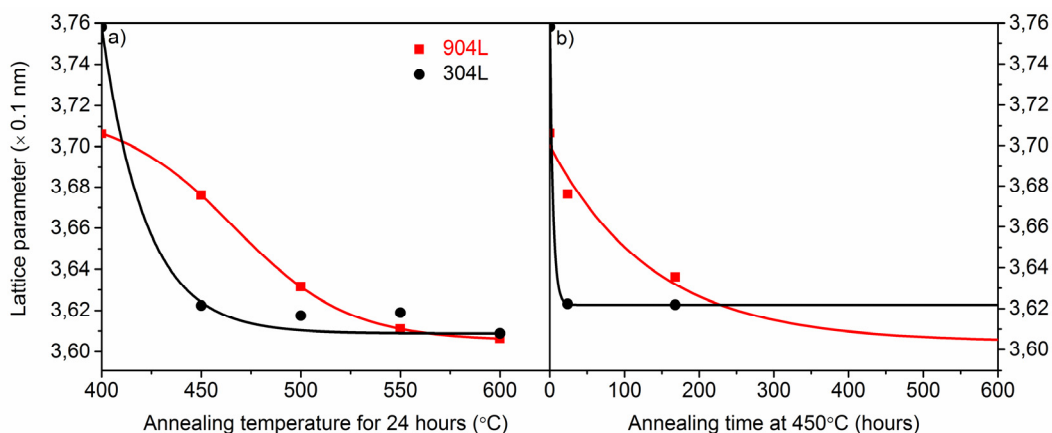


Figure 31 Lattice parameter of expanded austenite in 304L (black circles) and 904L (red squares) measured from (111) peak position of XRD pattern (a) as a function of temperature and (b) as a function of annealing time (from Paper III).

As reported in Paper III and Paper IV, expanded austenite in 304L is more prone to eutectoid decomposition (eq. 12). In particular, the presence of pre-existing ferrite/martensite phase could preferentially steer towards decomposition of γ_C towards the eutectoid route (Fig. 32). Mechanical polishing causes deformation induced martensitic transformation, which possibly provides nucleation sites for ferrite and carbides [134] during eutectoid decomposition. The final microstructure is a thick layer of ferrite with finely dispersed Cr-rich carbides and a small amount of residual austenite phase. It should be noticed that the grain size of newly formed ferrite is significantly smaller than that of austenite. Carbides are mainly located at grain boundaries of ferrite, but they also can be found within the grains. The non-polished side, instead, shows a mixed decomposition route, i.e. eutectoid and discontinuous. Highly alloyed 904L, on the other hand, shows a typical discontinuous precipitation mechanism (eq. 13), with progressive loss of interstitials and precipitation and growth of intergranular nitrides/carbides. Lamellae-like structures containing alternating carbides and austenite plates with thickness in the range of ~ 100 nm have been observed, as shown in Fig. 33. Deformation marks and twin boundaries are also preferential precipitation sites of $M_{23}C_6$ [131].

When annealing in vacuum (Paper IV) or in a protective atmosphere (Paper III, possibly slightly oxidising), three separated phenomena compete during the decomposition of expanded austenite: a) decarburization/denitriding (dominating at low-temperatures), b) inward diffusion of interstitials, as confirmed by means of GDOES in Paper IV and c) formation of carbides. Complete decomposition of expanded austenite is accompanied by relaxation of lattice strain, suggesting removal of most of the C/N from interstitial solid solution and recovery of the initial austenitic microstructure. In a recent study by Wang et al. [136], good thermal stability of a LTC 316L was confirmed after annealing at low-temperature ($< 375^\circ\text{C}$) in air for eight months, where inward diffusion over time was also observed. However, the possible precipitation of carbide (small size/small weight fraction) and decarburization were not assessed.

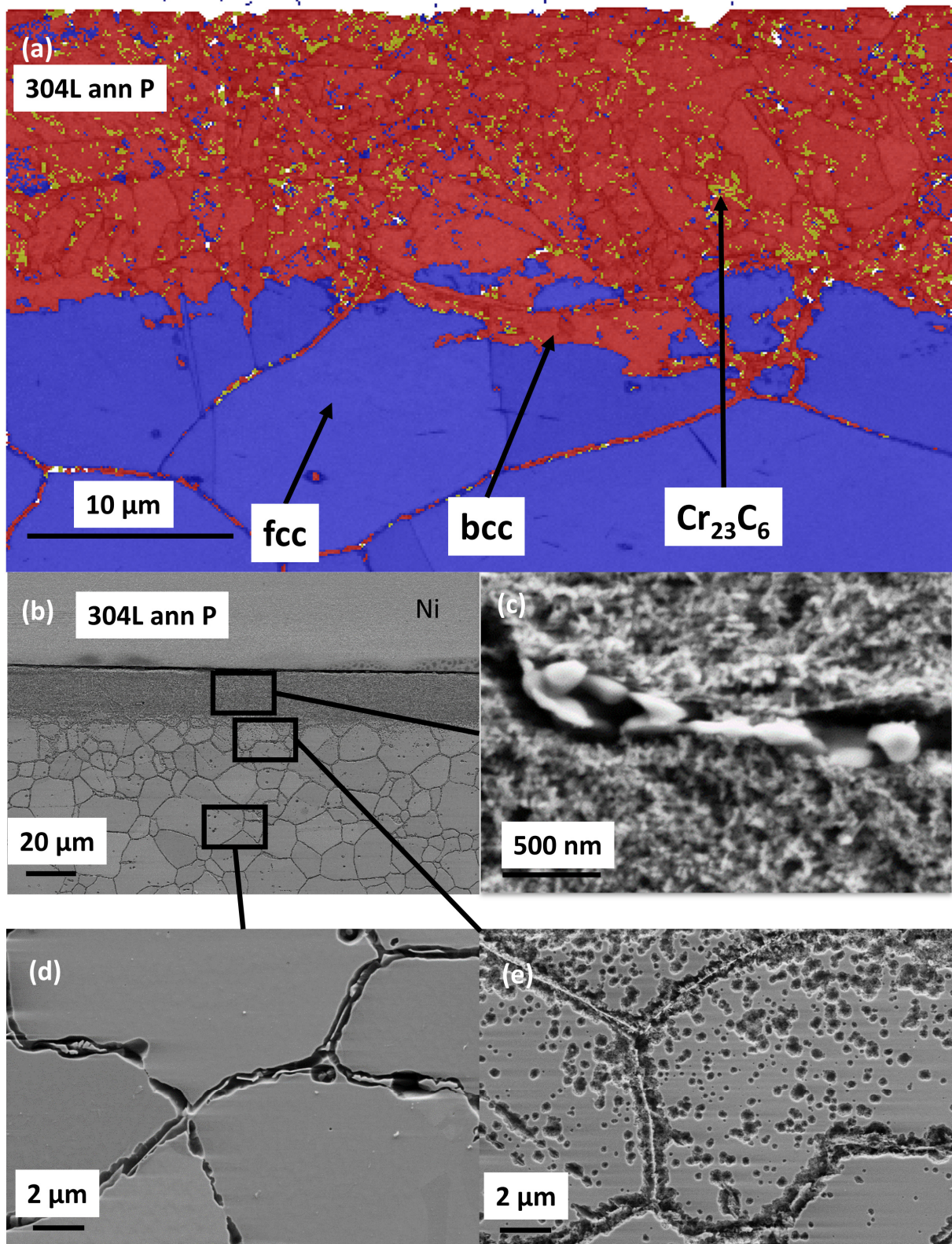


Figure 32 (a) EBSD phase map from cross-sections of annealed 304L, polished surface and (b, c, d, e) SEM images of the same cross-section (from Paper IV).

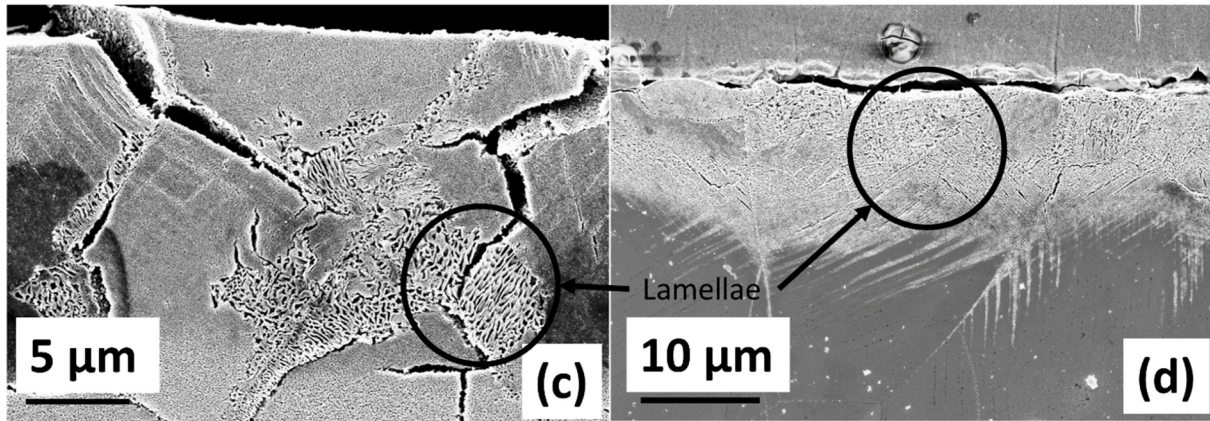


Figure 33 SEM micrograph of etched cross-sectioned from annealed LTC 904L. Left: polished surface. Right: sandblasted surface (from Paper IV).

5.6 Hardening effect and hardening mechanisms

The low-temperature nitriding and carburizing treatment investigated in this study enhanced the surface hardness by a factor of three to five. It is difficult to compare the hardening effect from different studies, as the measured hardness is strongly dependent on the treatment, the alloy composition, the material finish and the measuring method. This can be exemplified by comparing the hardness obtained on the cross-section and on the top surface using micro-indentation in Paper II and Paper VI. A low-load hardness testing performed on cross-section in proximity of the surface gives a significantly lower hardness compared to the hardness measured on the top-surface. The reason is the lack of “material” on the exposed surface, which allows easier deformation/relaxation in the first case, while in the second case the shallow hardness-probing is affected by the compressive stresses within the material below, thus showing higher hardness.

For nitrided and carburized surfaces, the major contribution to hardening was from interstitial solid solution and “work hardening” (Papers II, III and IV). Work hardening, in this context, means increase of dislocation density due to deformation resulted from internal stresses. The extent of interstitial supersaturation dictates the final resulting hardness. Carburized 904L was always harder than carburized 304L (Papers II, IV and VI) as the lattice strain and associated compressive stresses [5] were higher. Similarly, PN 304L was harder than 904L (Paper III, see Fig. 34).

However, while the original non-polished surfaces, with higher roughness, exhibited a deeper strained region from the surface finishing (skin pass or sandblasting) and larger interstitial supersaturation (see Fig. 29), the surface hardness was lower than that of the polished surfaces. It is proposed that the compressive stresses are relieved to a larger extent in e.g. sandblasted surfaces, due to a larger surface area.

Partial hardening effect is maintained in most cases even after thermal decomposition, except when mainly intergranular precipitation occurs (Fig. 34, top-right). The decrease in surface hardness in close proximity to the surface in Fig. 34 is a consequence of de-carburizing occurring at the surface after vacuum annealing. In some cases, hardness can even be enhanced

by precipitation hardening. As shown in Fig. 35, a peak hardness is observed at $\sim 450^{\circ}\text{C}$ in nitrated 304L and 904L. After prolonged annealing with growth of precipitates, however, this effect is reduced. It should be remembered, nevertheless, that even small and finely distributed Cr-carbides are expected to have detrimental effects on corrosion resistance and should, therefore, be avoided.

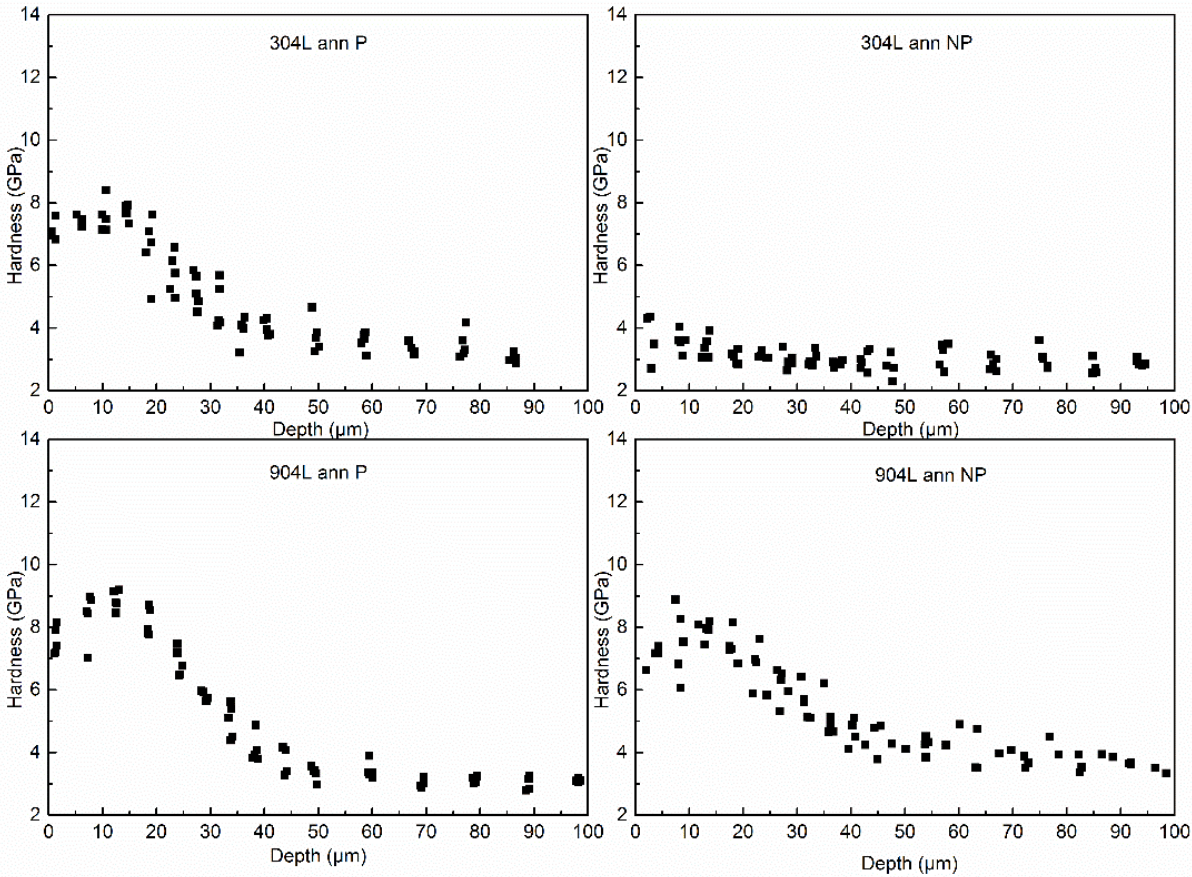


Figure 34 Hardness as a function of depth from nanoindentation on cross-section of carburized AISI 304L and 904L followed by isothermal vacuum annealing at 600°C for 150h. P and NP represent polished and non-polished surfaces, respectively (from Paper IV).

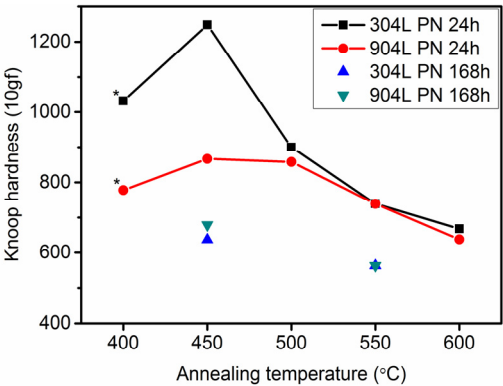


Figure 35 Hardness at the layer centre on the cross-section of nitrated 304L and 904L after isothermal annealing. Hardness values marked with * refer to the as-nitrated condition (from Paper III).

5.7 Tribological behaviour of LTC austenitic stainless steels

The tribological tests conducted in dry-sliding regime confirmed the poor performance of as-received austenitic stainless steels (Fig. 36a and Fig. 36c). Even at the low-load testing conditions, exponential increase in wear as a function of applied load was observed in 904L (Fig. 36a), where severe adhesion craters (galling) and gross abrasion grooves were observed already at load of 0.5 N (Fig. 37). Metastable 304L, however, behaved significantly better due to surface hardening given by the formation of deformation-induced martensite. In this case, oxidation wear and consequent spalling were the main wear mechanisms (Fig. 37), with a minor contribution from abrasive wear. Interestingly, there was a relative reduction of worn volume at increased loads that was supposedly due to an increased martensite formation. It is expected that oxide will break off when the underlying material is too soft to sustain the mechanical load. Indeed, at the highest load in the test condition, the surface oxide of 904L is completely fractured, leading to the severe wear via three-body abrasion.

After LTC, both materials showed a virtually negligible wear (Fig. 36d). Adhesion and abrasion were completely eliminated owing to the increase in hardness, while the coefficient of friction decreased by up to ~10%. Expanded austenite was stable under the test conditions without any thermo-mechanical decomposition, as confirmed by XRD analysis. Also, no “thin ice” effect was observed due to the low-loads involved in the testing, given the maximum shear stresses were within the expanded austenite layer.

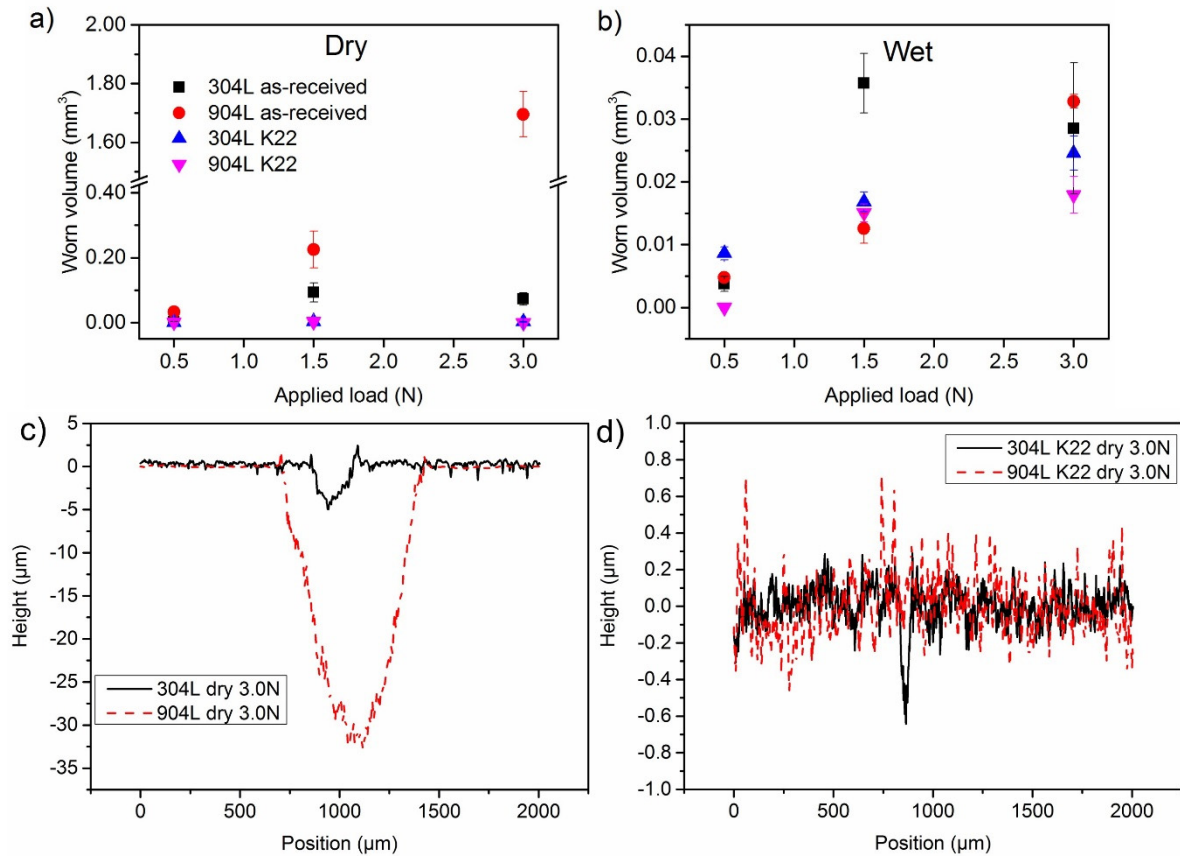


Figure 36 Worn volume after pin-on-disc tests performed in (a) dry and (b) wet sliding condition on 304L and 904L plates. Wear track profile measured by stylus profilometry after pin-on-disc test on (c) untreated 304L and 904L and (d) low-temperature carburized (K22) 304L and 904L in dry sliding condition at 3.0 N load (from Paper VI).

The surface oxide was in this case significantly more adherent in 904L, while more cracking and spalling were observed in 304L (Fig. 38). The reason is thought to be the lower surface hardness achieved in 304L compared to 904L due to lower interstitial supersaturation.

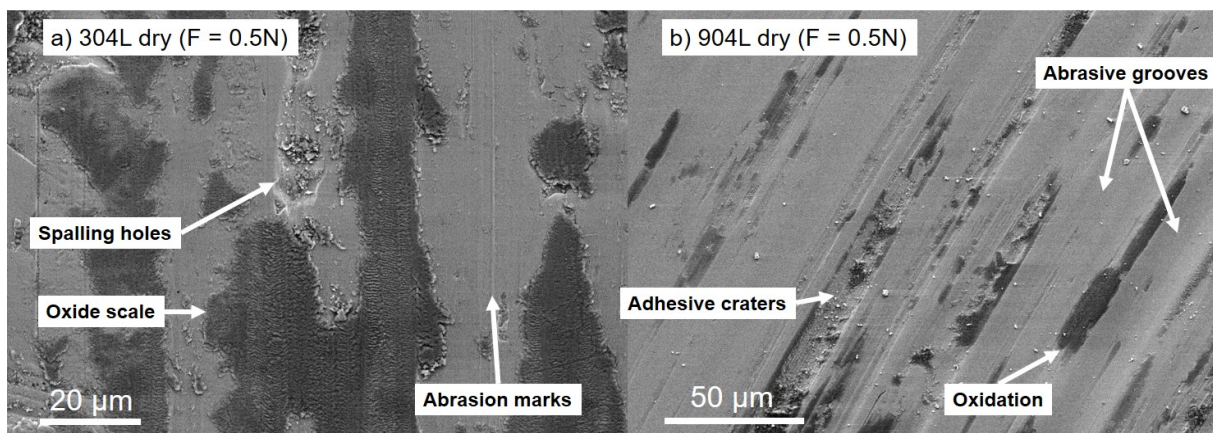


Figure 37 Secondary electron micrographs of wear tracks in (a) 304L and (b) 904L after dry sliding with 0.5 N load (from Paper VI).

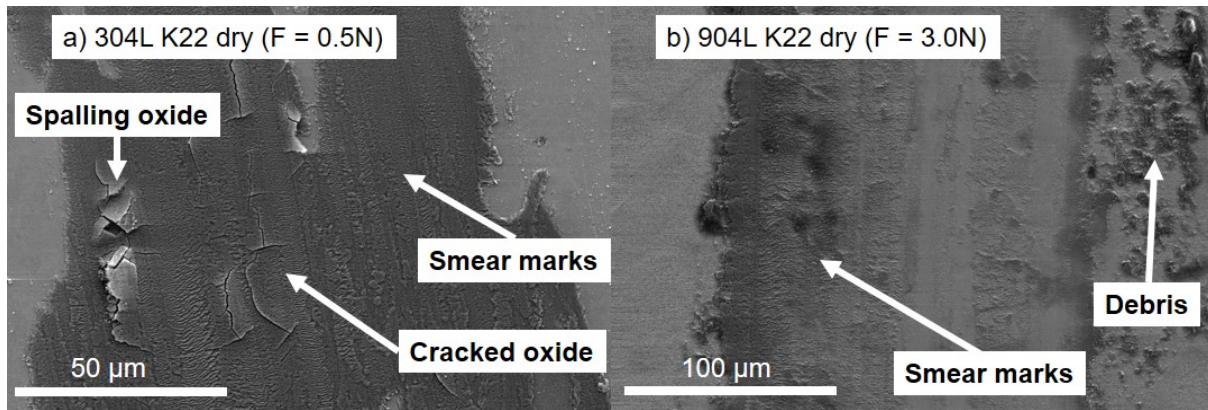


Figure 38 Secondary electron micrographs of wear tracks in carburized (a) 304L after dry sliding with 0.5 N load and (b) 904L after dry sliding with 3.0 N load (from Paper VI).

In wet-testing condition, compared with untreated steels, the enhancement given by LTC treatment was still present, but considerably reduced (Fig. 36b). As the coefficient of friction becomes significantly lower due to the hydrodynamic lubrication effect of the solution, adhesion wear is not an issue even with untreated materials. Moreover, the oxidised debris were removed by the turbulent action of the liquid instead of depositing within the wear track. As a result, mainly mild abrasive wear (mostly two-body) and a small contribution from oxidation and pitting (only in 304L) is present in the untreated materials.

5.8 Electrochemical properties of LTC austenitic stainless steels

Expanded austenite surface layers are known to be “white-etching layers” when subjected to metallographic preparation. Therefore, it is expected that the corrosion resistance is somewhat enhanced as a consequence of LTTT. In this study, the electrochemical behaviour of LTC austenitic stainless steels was evaluated in acidic environment (pH = 1) with addition of 2 ppm of F⁻ ions to test the applicability of LTC materials for bipolar plates in PEMFC applications. The presence of surface carbides had a detrimental effect on the corrosion resistance of the tested material, with a marked increase in I_{crit} and I_{pass} , as shown by the polarisation diagram reported in Fig. 39. As stated in the previous sections, all the carbides formed during LTC treatment presented an enrichment in Cr, thus depleting the main passivating element from the matrix. However, mechanical removal of the surface carbide layer by polishing produced a precipitate-free surface, which showed improved corrosion characteristics compared to the as-carburized material.

A general nobilitation of the steels by LTC was observed, provided that carbide formation was avoided, as reflected by an increase in E_{corr} , accompanied by lower I_{corr} . The LTC condition is also associated with lower I_{pass} , while the E_{trans} did not show significant improvement. The interesting change in polarisation behaviour was at the E_{pass} , where a transient passivation was found at anodic polarisation values equivalent to the passivation potential of the untreated steels. Moreover, a second stable passivating stage was present at 0.16 – 0.29 V higher than the E_{pass} of the original material.

The change in passivation potential is a reflection of a change in chemical composition of the passivating oxide. In LTC materials, the surface oxide was enriched in Fe, having a cationic

ratio similar the one of the original steels. This is believed to be related to the interaction between Cr and C, which partly prevents Cr from preferentially accumulating within the surface oxide. This does not appear to affect negatively the passive current even after potentiostatic experiments in the test environment. However, a reduction of the oxide layer thickness was observed.

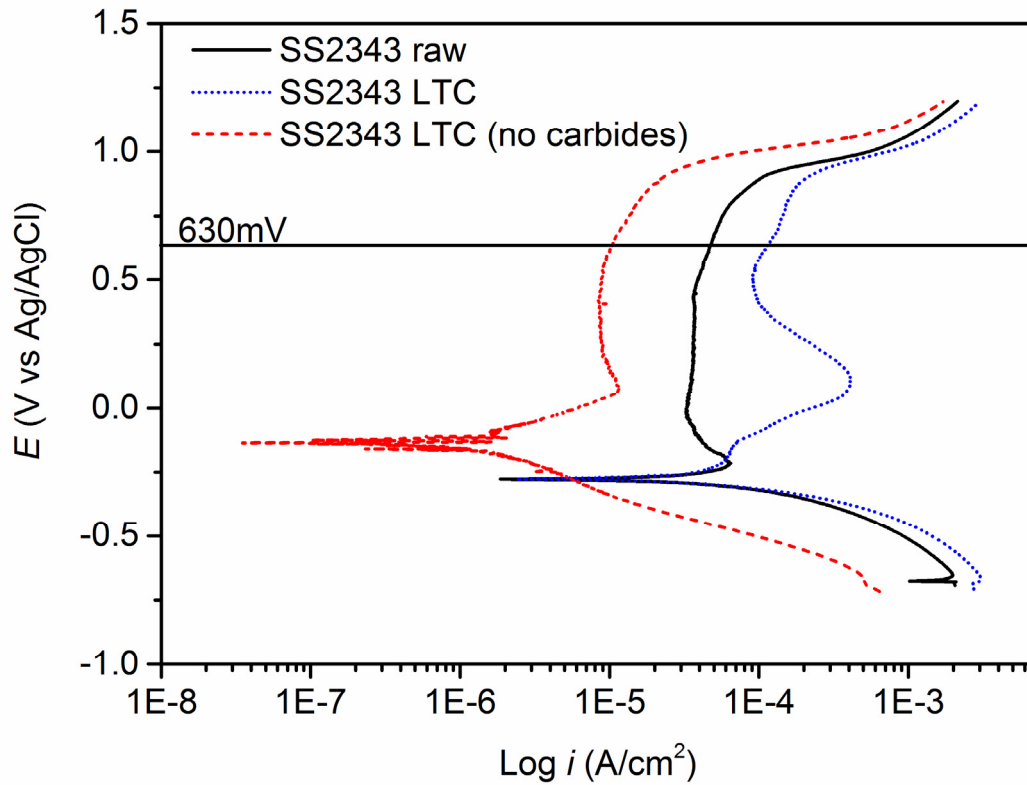


Figure 39 Example of polarisation diagram of SS2343 austenitic stainless steel in simulated cathodic PEMFC environment (from Paper V).

The oxide film thinning, together with the change in chemical composition, translated into a lower ICR when an LTC material tested in contact with carbon paper (Fig. 40a). The interfacial contact resistance with carbon-paper decreased by a factor up to four, reaching resistance values close to the DoE guidelines for application as bipolar plates in PEMFC [133].

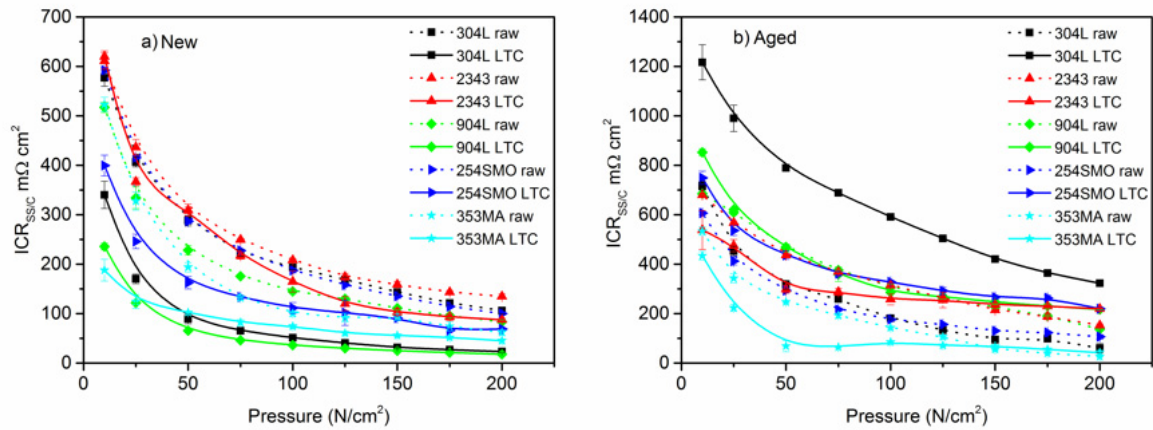


Figure 40 (a) Interfacial contact resistance (ICR) between carbon-paper and stainless steel discs in as-received (raw) and carburized state (LTC). (b) ICR after potentiostatic ageing in $0.1 \text{ H}_2\text{SO}_4 + 2 \text{ ppm NaF}$. Dotted lines represent the trend of raw materials while continuous lines represent the LTC materials (from Paper V).

However, repeating the ICR measurements after potentiostatic “ageing”, the LTC materials exhibited reduced performance compared with the corresponding “new” as-carburized materials (Fig. 40b). While the average oxide thickness was not significantly different, localised corrosion was observed in the aged condition. In particular, pits and S-enriched areas were found in proximity of Cr-C enriched areas and could be connected to a worsening of the electrical conductivity across the surface. This hypothesis is in good agreement with other studies on corrosion testing of LTC materials in sulphur-containing environments [42,103].

6 Conclusions

- Effects of alloy composition and surface finish on microstructure of expanded austenite

Highly deformed surfaces can increase the diffusion depth of interstitial species at low temperature through pipe-diffusion. This is more prominent in nitrided materials, where the diffusivity of N in austenitic stainless steels is naturally smaller than that of C. Surface deformation can also increase the solid solubility limit. Too high plastic deformation, however, can lead to over-saturation of traps and consequently decrease the diffusivity due to lowered concentration-dependent atomic jumping probability.

Presence of deformation induced martensite/ferrite at the surface may hinder the formation of expanded austenite in austenitic stainless steels by promoting nitride/carbide precipitation.

Increase in roughness, as a consequence of interstitial supersaturation, is caused by anisotropic strain and preferential slipping on closely packed planes. A larger supersaturation (for an equivalent case depth) leads to a corresponding increase in roughness. Anisotropic strains generated internally can be observed experimentally by EBSD analysis, if large enough.

Presence of elements with large atomic radius (e.g. Mo) can increase the thickness of diffusion layer and the maximum solubility of interstitials via volumetric expansion of the original austenitic lattice. Nickel, on the other hand, has the opposite effect.

- Chemical interactions between supersaturated interstitial N/C and alloying elements

Unique binding energies for both Cr 2p_{3/2} and N 1s core levels were determined via XPS for Cr-N interaction in expanded austenite. They are different from those of CrN. The same could not be done for Cr-C interaction, where the difference of Cr 2p_{3/2} between Cr_xC_y and Cr in C-stabilised expanded austenite could not be distinguished by conventional XPS analysis. The chemistry of other alloying elements (e.g. Fe) does not appear to be affected by interstitial supersaturation.

- Electrochemical properties of γ_C

The formation of expanded austenite affects the corrosion resistance by shifting both the E_{corr} the effective E_{pass} to more noble values (by 0.16 – 0.29 V). The passive film is thinner than the original one and is preferentially enriched in Fe, with cationic ratio close to that of the bulk material. The interfacial contact resistance is consequently decreased. The passivity characteristics are not significantly affected in the short term, but localised pitting and a complex S-Cr-C interaction could be deleterious for certain applications.

- Thermal decomposition mechanisms in γ_C and γ_N

In both γ_C and γ_N eutectoid and discontinuous decomposition could be identified upon isothermal annealing. It is the alloy composition and the relative austenite stability that determines the mode of decomposition. A mixed eutectoid/discontinuous decomposition was identified for γ_C in metastable 304L steel. The presence of deformation induced martensite acts as preferential nucleation point for ferrite and carbides, facilitating eutectoid decomposition. While, in case of 904L, exclusively discontinuous decomposition was observed.

Nickel in particular has a fundamental capacity of stabilising expanded austenite by kinetically hindering carbide precipitation. Consequently, the thermal stability of expanded austenite is increased in superaustenitic stainless steels. Expanded austenite (γ_N) formed on AISI 904L shows the best resistance to thermal decomposition ever reported up to date.

- Enhancement of surface hardness and tribological properties by LTTT austenitic stainless steels

Hardness is enhanced by a factor of three to five. Compared to C-stabilized expanded austenite, N-stabilized one possesses stronger hardening effect, but with higher tendency to embrittlement and lower load-bearing capacity due to comparatively thinner layer.

The main hardening mechanism of expanded austenite is interstitial supersaturation and related compressive stresses. Presence of plastic deformation increases the solubility limit and provides an external strain-hardening, contributing to further hardness enhancement.

After high-temperature annealing, hardening can be partially maintained if carbide/nitride precipitates on intragranular sites by eutectoid decomposition or on pre-existing high energy locations such as slip planes or twins by discontinuous decomposition. Denitriding/decarburizing may occur if heating is performed in vacuum or in a protective atmosphere, with a consequent softening of the first few micrometres below the surface. Further interstitial diffusion towards the bulk can extend the effective layer thickness even without nitriding/carburizing atmosphere.

In dry sliding conditions, low-temperature thermochemical treatment is able to increase the low-load wear resistance significantly in austenitic and superaustenitic stainless steels, with mild oxidation wear as the main mechanism. The beneficial effect is somewhat less evident in the metastable stainless steel 304L, due to the formation of deformation induced martensite. In case of proper lubrication and low-load conditions, the difference in wear resistance between untreated and carburized steels becomes smaller.

- Nature of surface carbides/nitrides in LTTT austenitic stainless steels

For 304L and SS2343, precipitation of carbides/nitrides during LTTT treatments occurs in proximity of the surface, where the interstitial concentration is maximal and so are the internal stresses. Carbides seem to form preferentially along the easy-to-slip $\{111\}\gamma$ planes when a critical level of supersaturation is reached. This is accompanied by elemental partitioning (Cr-enrichment and Ni-rejection). Coherent nature of the interface between $\chi/\omega/M_{23}C_6$ and γ_C , as well as between the carbides themselves, makes the grain boundaries less preferred for precipitation. In 304L, only χ -carbides were observed at the surface of Kolsterised materials, while in SS2343 χ , ω , and $M_{23}C_6$ carbides having different morphologies were observed.

7 Suggestions for future works

Further studies on the thermal stability of N/C expanded austenite on austenitic stainless steels

- Expanded austenite is not suitable for the application where a sustained decomposition takes place. However, it can be applied in the conditions where decomposition is hindered or slowed down for long time. For example, in case of Al high-pressure die casting, the material used for die is constantly cooled despite the surface is subjected to high temperature flashes. The thermal stability in such situation is of great interest.
- It is known that V, Ti, Al have higher affinity to C/N than Cr. Addition of these elements to the steel would be beneficial to the corrosion resistance even after thermal decomposition of expanded austenite because Cr should remain within the austenitic matrix. Preferential precipitation of carbides/nitrides containing these elements could compensate for the loss of hardness as a consequence of less supersaturation.
- Considering that surface oxide may act as a barrier for interstitial diffusion, it would be interesting to control denitriding/decarburizing by applying a capping layer which is not reactive with C or N.
- The research on optimisation of low-temperature thermochemical treatment for austenitic stainless steels should continue. Though high-Ni, high-Mo may lead to a good compromise between layer thickness and resistance to carbide precipitation, the cost of the alloy should be taken into consideration for a real technological breakthrough. High Mn-containing materials, with addition of Mo-substitutes (e.g. Cu) could be attempted.

Further studies on microstructure of expanded austenite

- More high-diffusivity paths could increase the effective layer thickness of expanded austenite layers. Though in austenitic stainless steels this would also lead to an increased amount of precipitates. A balance could be reached by tailoring the process temperature for treatment optimisation.
- Low-temperature thermochemical treatment of highly porous austenitic stainless steels, obtained, for example, by additive manufacturing, could be performed in order to obtain a 3-dimensional network of expanded austenite, aiming at a novel type of reinforcement.
- *In situ* studies could be performed to determine the precipitation sequence in 316L. Whether χ -carbides can transform into ω -carbides before turning into $M_{23}C_6$ or if they form exclusively due to high-carburizing potential is of interest. Additionally, the reason for the exclusive presence of χ -carbides in 304L could be further investigated.

8 Acknowledgements

First and foremost I would like to thank my supervisors, Associate Professor Yu Cao and Professor Lars Nyborg, for their constant support and guidance in the last five years. Their knowledge and commitment were fundamental for the development of this thesis work and for my growth as a researcher.

Heinz Kaiser and Bodycote Värmebehandling AB (Sweden) are highly acknowledged for providing the surface treatments on which the current thesis is based upon. In particular, special thanks go to Fredrik Carlsson who introduced us to Kolsterising and Dr. Andreas Karl for the support.

National School of Materials Science, Area of Advance Materials Science and National Swedish Energy Administration are acknowledged for financial support of this PhD project. Jernkontoret and Chalmersska Forskningsfonden are also to be thanked for providing financial support.

I would like to thank “our” research engineers: Urban Jelvestam, Dr. Eric Tam, Dr. Yiming Yao, Roger Sagdahl and Håkan Millqvist for all the practical assistance and for standing my rather frequent “Just a small question...” and “I think we have a problem with...”. I believe you deserve a statue for your patience and kindness!

Many thanks to all the co-authors of the papers included in this thesis, starting from Dr. Mats Norell and Prof. Uta Klement for the thorough discussions, Dr. Simone Vezzù and Dr. Alfonso Pérez-García, Miguel Esnaider, for their efforts in long-distance cooperation, Dr. Lina Rogström for the interest in my research, MSc. Stefan Kante for being such a dedicated student. A special mention to Cammy and Kenny, for trying to improve my English.

I would like to express my sincere gratitude to all the members and colleagues working in the ex-Department of Materials and Manufacturing Technology. In particular I would like to thank the colleagues and friends who already left: Dr. Christos Oikonomou, Dr. Seshendra Karamchedu, Dr. Amir Malakizadi, Dr. Erik Stenvall, Dr. Kumar Babu Surreddi, Dr. Stefan Cedergren, Dr. Ruth Ariño Marine for being so friendly from the day of my arrival in this department.

Continuing with colleagues and friends, I would like to thank Dinesh Mallipeddi, Kristina Karlsson, Johan Wendel, Casey Jessop, Antonio Mulone, Johanna Ekberg, Philipp Hoier, Sakari Tolvanen, Maheswaran Vattur Sundaram, Dimitris Nikas, Elanghovan Natesan, Abhijit Venkatesh, Ceena Joseph, Saad Sheik, Simon Isakson, Alexander Leicht, Eric Bojestig, Dmitri Riabov, Camille Pauzon, Swathi Kiranmayee Manchili, Adrianna Lozinko. For the discussions, fika breaks, innebandy and teaching (me skiing!).

I would like to thank my Family and the friends of a lifetime, who never lack in making me feel as if I was always there with them.

Dulcis in fundo, a great thank you to Giedre: without you I would not even be here (in Sweden) in the first place! Not to mention the loving understanding and ENORMOUS patience you had with me, especially in the past year...

The final dedication is to my parents, you are always in my mind and in my heart.

9 References

- [1] M.F. McGuire, *Stainless Steels for Design Engineers*, ASM International, 2008. doi:10.1016/B0-08-043152-6/00081-4.
- [2] M.J. Bos, *Case Hardening of Austenitic Stainless Steel Pump Components*, *World Pumps*. (1998) 30–34.
- [3] T. Christiansen, M. a J. Somers, Low temperature gaseous surface hardening of stainless steel, *Proc. Eur. Conf. Heat Treat. 2010 Nitriding Nitrocarburising*. 21 (2010) 160–167. doi:10.1533/9780857096524.4.557.
- [4] G.M. Michal, F. Ernst, H. Kahn, Y. Cao, F. Oba, N. Agarwal, A.H. Heuer, Carbon supersaturation due to paraequilibrium carburization: Stainless steels with greatly improved mechanical properties, *Acta Mater.* 54 (2006) 1597–1606. doi:10.1016/j.actamat.2005.11.029.
- [5] T.L. Christiansen, T.S. Hummelshøj, M.A.J. Somers, Expanded austenite, crystallography and residual stress, *Surf. Eng.* 26 (2010) 242–247. doi:10.1179/026708410X12506870724316.
- [6] H. Dong, S-phase surface engineering of Fe-Cr, Co-Cr and Ni-Cr alloys, *Int. Mater. Rev.* 55 (2010) 65–98. doi:10.1179/095066009X12572530170589.
- [7] J. Buhagiar, 25 years of S-phase, *Surf. Eng.* 26 (2010) 229–232. doi:10.1179/026708410X12687356948751.
- [8] T.L. Christiansen, M.A.J. Somers, Low temperature surface hardening of stainless steel, in: E.J. Mittemeijer, M.A.J. Somers (Eds.), *Thermochem. Surf. Eng. Steels*, Woodhead Publishing Limited, Cambridge, 2015: pp. 557–579. doi:10.1533/9780857096524.4.557.
- [9] S.R. Collins, P.C. Williams, S.V. Marx, A.H. Heuer, F. Ernst, H. Kahn, *Low-Temperature Carburization of Austenitic Stainless Steels*, *ASM Handbook*, Vol. 4D. 4 (2014) 451–460.
- [10] B.K. Brink, K. Ståhl, T.L. Christiansen, J. Oddershede, G. Winther, M.A.J. Somers, *Scripta Materialia On the elusive crystal structure of expanded austenite*, *Scr. Mater.* 131 (2017) 59–62. doi:10.1016/j.scriptamat.2017.01.006.
- [11] W. Krivsky, The linde argon-oxygen process for stainless steel; A case study of major innovation in a basic industry, *Metall. Mater. Trans. B.* 4 (1973) 1439–1447. doi:10.1007/BF02667991.
- [12] Outokumpu Oyj, *Handbook of Stainless Steel*, (2013).
- [13] Issf, *Stainless steel in figures 2013*, (2013) 5–7. http://www.worldstainless.org/Files/ISSF/non-image-files/PDF/ISSF_Stainless_Steel_in_Figures_2013.pdf.
- [14] G.S. Reis, A.M. Jorge Jr., O. Balancin, Influence of the microstructure of duplex stainless steels on their failure characteristics during hot deformation, *Mater. Res.* 3 (2000) 31–35. doi:10.1590/S1516-14392000000200006.
- [15] B.D. Miller, Precipitation Behavior of M 23 C 6 Carbides in Type 304 Stainless Steel Containing Delta Ferrite, *Microsc. Microanal.* 1 (2012) 1352–1353. doi:10.1017/S14319276.
- [16] A.F. Padilha, C.F. Tavares, M.A. Martorano, Delta Ferrite Content in Stainless Steel Castings, *Adv. Mater. Forum VI.* 52 (2013) 733–738. doi:10.2355/isijinternational.52.1054.
- [17] A.F. Padilha, P.R. Rios, Decomposition of Austenite in Austenitic Stainless Steels, *ISIJ Int.* 42 (2002) 325–327. doi:10.2355/isijinternational.42.325.
- [18] R.P. Pascale Sotto Vangeli, Bo Ivarsson, *Comparative Behaviour of Speciality Austenitic Stainless Steels in High Temperature Environments*, *Acom.* (2012).
- [19] S. Jani, M. Marek, R.F. Hochman, E.I. Meletis, A Mechanistic Study of Transgranular Stress Corrosion Cracking of Type 304 Stainless Steel, *Metall. Trans.* 22A (1991).

- [20] R.W. Swindeman, *Fatigue of Austenitic Stainless Steels in the Low and Intermediate Cycle Range*, 1966.
- [21] A.G. Hartline, The effect of nitrogen additions upon the pitting resistance of 18 pct Cr, 18 pct Mn Stainless Steel, *Metall. Trans.* 5 (1974) 2271–2276. doi:10.1007/BF02644006.
- [22] Outokumpu Oyj, *Outokumpu Surface Finishes*, (2014). <http://www.outokumpu.com/sitecollectiondocuments/outokumpu-surface-finishes-brochure.pdf>.
- [23] Outokumpu Oyj, *Stainless steels for extremely corrosive environments*, (2015) 1–8. <https://www.outokumpu.com/SiteCollectionDocuments/Outokumpu-Ultra-Range-stainless-steel-datasheet.pdf>.
- [24] Outokumpu, *Standard Cr-Ni Stainless Steels*, 2006. www.outokumpu.com/stainless.
- [25] G.F. Vander Voort, *ASM Handbook: Metallography and Microstructures*, 2004. doi:10.1361/asmhba0003771.
- [26] S. Ghosh, V. Kain, Microstructural changes in AISI 304L stainless steel due to surface machining: Effect on its susceptibility to chloride stress corrosion cracking, *J. Nucl. Mater.* 403 (2010) 62–67. doi:10.1016/j.jnucmat.2010.05.028.
- [27] P.E. Manning, D.J. Duquette, W.F. Savage, Technical Note: The Effect of Retained Ferrite on Localized Corrosion in Duplex 304L Stainless Steel, *Weld. Res. Suppl.* (1980) 260–262.
- [28] M. Zandrahimi, M.R. Bateni, a. Poladi, J. a. Szpunar, The formation of martensite during wear of AISI 304 stainless steel, *Wear.* 263 (2007) 674–678. doi:10.1016/j.wear.2007.01.107.
- [29] A.K. De, D.C. Murdock, M.C. Mataya, J.G. Speer, D.K. Matlock, Quantitative measurement of deformation-induced martensite in 304 stainless steel by X-ray diffraction, *Scr. Mater.* 50 (2004) 1445–1449. doi:10.1016/j.scriptamat.2004.03.011.
- [30] S. Kim, H. Kwon, H. Kim, Effect of delta ferrite on Corrosion Resistance of Type 316L Stainless Steel in Acidic Chloride Solution by Micro-droplet Cell, 126 (2007) 1533–1536. doi:10.4028/www.scientific.net/SSP.124-126.1533.
- [31] Outokumpu, *High Performance Austenitic Stainless Steel*, (2015) 1–12.
- [32] Outokumpu, *Ultra 904L*, (2015) 1–7.
- [33] J. Piekoszewski, B. Sartowska, M. Barlak, P. Konarski, L. D, W. Starosta, L. Walis, *Surface & Coatings Technology Improvement of high temperature oxidation resistance of AISI 316L stainless steel by incorporation of Ce – La elements using intense pulsed plasma beams*, 206 (2011) 854–858. doi:10.1016/j.surfcoat.2011.03.104.
- [34] A. Iversen, B. Leffer, *Aqueous Corrosion of Stainless Steels*, in: T.J.A. Richardson (Ed.), *Shreir's Corros.*, Elsevier B.V., 2010: pp. 1806–1877. doi:10.1016/C2009-1-28357-2.
- [35] M.K. Lei, X.M. Zhu, Role of nitrogen in pitting corrosion resistance of a high-nitrogen face-centered-cubic phase formed on austenitic stainless steel, *J. Electrochem. Soc.* 152 (2005) B291–B295. doi:10.1149/1.1939245.
- [36] F.M. Bayoumi, W.A. Ghanem, Effect of nitrogen on the corrosion behavior of austenitic stainless steel in chloride solutions, *Mater. Lett.* 59 (2005) 3311–3314. doi:10.1016/j.matlet.2005.05.063.
- [37] A. Chiba, S. Shibukawa, I. Muto, T. Doi, K. Kawano, Y. Sugawara, N. Hara, Microelectrochemical Aspects of Interstitial Carbon in Type 304 Stainless Steel: Improving Pitting Resistance at MnS Inclusion, *J. Electrochem. Soc.* 162 (2015) C270–C278. doi:10.1149/2.0851506jes.
- [38] F.J. Martin, E.J. Lemieux, T.M. Newbauer, R.A. Bayles, P.M. Natishan, H. Kahn, G.M. Michal, F. Ernst, A.H. Heuer, Carburation-Induced Passivity of 316 L Austenitic Stainless Steel, *Electrochem. Solid-State Lett.* 10 (2007) C76. doi:10.1149/1.2794282.

- [39] A.H. Heuer, H. Kahn, L.J. O'Donnell, F. Ernst, G.M. Michal, R.J. Rayne, F.J. Martin, P.M. Natishan, Carburization-Enhanced Passivity of PH13-8 Mo: A Precipitation-Hardened Martensitic Stainless Steel, *Electrochem. Solid-State Lett.* 13 (2010) C37–C39. doi:10.1149/1.3491468.
- [40] R. Ritzenhoff, A. Hahn, Corrosion Resistance, *InTech*, 2012. doi:10.5772/1844.
- [41] H. Li, Z. Jiang, Y. Yang, Y. Cao, Z. Zhang, Pitting corrosion and crevice corrosion behaviors of high nitrogen austenitic stainless steels, *Int. J. Miner. Metall. Mater.* 16 (2009) 517–524. doi:10.1016/S1674-4799(09)60090-X.
- [42] P. Niederhofer, L. Richrath, S. Huth, W. Theisen, Influence of conventional and powder-metallurgical manufacturing on the cavitation erosion and corrosion of high interstitial CrMnCN austenitic stainless steels, *Wear.* 360–361 (2016) 67–76. doi:10.1016/j.wear.2016.04.017.
- [43] D. Formosa, R. Hunger, A. Spiteri, H. Dong, E. Sinagra, J. Buhagiar, Corrosion behaviour of carbon S-phase created on Ni-free biomedical stainless steel, *Surf. Coatings Technol.* 206 (2012) 3479–3487. doi:10.1016/j.surfcoat.2012.02.020.
- [44] B.N. Mordyuk, G.I. Prokopenko, M.A. Vasylyev, M.O. Iefimov, Effect of structure evolution induced by ultrasonic peening on the corrosion behavior of AISI-321 stainless steel, *Mater. Sci. Eng. A.* 458 (2007) 253–261. doi:10.1016/j.msea.2006.12.049.
- [45] T. Wang, J. Yu, B. Dong, Surface nanocrystallization induced by shot peening and its effect on corrosion resistance of 1Cr18Ni9Ti stainless steel, *Surf. Coatings Technol.* 200 (2006) 4777–4781. doi:10.1016/j.surfcoat.2005.04.046.
- [46] H.F.G. de Abreu, S.S. de Carvalho, P. de Lima Neto, R.P. dos Santos, V.N. Freire, P.M. de O. Silva, S.S.M. Tavares, Deformation induced martensite in an AISI 301LN stainless steel: characterization and influence on pitting corrosion resistance, *Mater. Res.* 10 (2007) 359–366. doi:10.1590/S1516-14392007000400007.
- [47] X. Wang, D. Li, Mechanical and electrochemical behavior of nanocrystalline surface of 304 stainless steel, *Electrochim. Acta.* 47 (2002) 3939–3947. doi:10.1016/S0013-4686(02)00365-1.
- [48] A.S. Lima, A.M. Nascimento, H.F.G. Abreu, P. De Lima-Neto, Sensitization evaluation of the austenitic stainless steel AISI 304L, 316L, 321 and 347, *J. Mater. Sci.* 40 (2005) 139–144. doi:10.1007/s10853-005-5699-9.
- [49] T.M. Devine, The mechanism of sensitization of austenitic stainless steel, *Corros.Sci.* 30 (1990) 135–151. doi:10.1016/0010-938X(90)90068-G.
- [50] D. Pye, *Steel Heat Treatment Metallurgy and Technologies*, in: *Steel Heat Treat. Metall. Technol.*, CRC Press, Boca Raton (FL), 2006.
- [51] P. Weymer, Principles of Gas Nitriding, *Heat Treat. Prog.* (2009) 12–13. doi:10.1016/B978-1-85617-803-7.50022-5.
- [52] M.A.J. Somers, T.L. Christiansen, *Gaseous processes for low temperature surface hardening of stainless steel*, Woodhead Publishing Limited, 2015. doi:10.1533/9780857096524.4.581.
- [53] T. Christiansen, M.A.J. Somers, Characterisation of low temperature surface hardened stainless steel, *Struers J. Mater.* (2006) 1–17.
- [54] E.J. Mittemeijer, Fundamentals of Nitriding and Nitrocarburizing, in: *ASM Handbook, Vol. 4, Heat Treat. Fundam. Process.*, ASM International, n.d.
- [55] T. Czerwiec, H. Michel, E. Bergmann, Low-pressure, high-density plasma nitriding: mechanisms, technology and results, *Surf. Coatings Technol.* 108–109 (1998) 182–190. doi:10.1016/S0257-8972(98)00555-6.
- [56] J. Elwart, R. Hunger, Plasma (Ion) Nitriding and Nitrocarburizing of Steels, in: *ASM Handbook, Vol. 4A, Steel Heat Treat. Fundam. Process.*, 2013: pp. 690–703.
- [57] P.C. Williams, S.R. Collins, S. V Marx, *Low Temperature Carburization Under Soft*

- Vacuum, US 2011/0030849 A1, 2011.
- [58] T.L. Christiansen, M.A.J. Somers, Low-Temperature Surface Hardening of Stainless Steel, *Adv. Mater. Process.* 171 (2013) 52–53. doi:10.1007/s11661-009-9904-3.
- [59] Bodycote, Specialty Stainless Steel Processes (S3P), (n.d.). <http://www.bodycote.com/en/services/heat-treatment/specialty-stainless-steel-processes.aspx>.
- [60] Z.L. Zhang, T. Bell, Structure and Corrosion Resistance of Plasma Nitrided Stainless Steel, *Surf. Eng.* 1 (1985) 131–136. doi:10.1179/sur.1985.1.2.131.
- [61] K. Ichii, K. Fugimura, T. Takese, Structure of the Ion-Nitrided Layer of 18-8 Stainless Steel, *Technol. Reports Kansai Univ.* 27 (1986) 135–144.
- [62] M.P. Fewell, D.R.G. Mitchell, J.M. Priest, K.T. Short, G.A. Collins, The nature of expanded austenite, *Surf. Coatings Technol.* 131 (2000) 300–306. doi:10.1016/S0257-8972(00)00804-5.
- [63] A. Martinavičius, G. Abrasonis, W. Möller, Influence of crystal orientation and ion bombardment on the nitrogen diffusivity in single-crystalline austenitic stainless steel, *J. Appl. Phys.* 110 (2011) 74907. doi:10.1063/1.3646493.
- [64] G. Abrasonis, J.P. Rivière, C. Templier, A. Declémy, S. Muzard, L. Pranevicius, A comparative study of ion beam nitriding of single-crystalline and polycrystalline 316L austenitic stainless steel, *Surf. Coatings Technol.* 196 (2005) 262–266. doi:10.1016/j.surfcoat.2004.08.099.
- [65] C. Templier, J.C. Stinville, P.O. Renault, G. Abrasonis, P. Villechaise, J.P. Rivière, M. Drouet, Nitrogen interstitial induced texture depth gradient in stainless steel, *Scr. Mater.* 63 (2010) 496–499. doi:10.1016/j.scriptamat.2010.05.012.
- [66] M.P. Fewell, J.M. Priest, High-order diffractometry of expanded austenite using synchrotron radiation, *Surf. Coatings Technol.* 202 (2008) 1802–1815. doi:10.1016/j.surfcoat.2007.07.062.
- [67] T. Christiansen, M. a J. Somers, On the crystallographic structure of S-phase, *Scr. Mater.* 50 (2004) 35–37. doi:10.1016/j.scriptamat.2003.09.042.
- [68] K. Farrell, E.D. Specht, J. Pang, L.R. Walker, A. Rar, J.R. Mayotte, Characterization of a carburized surface layer on an austenitic stainless steel, *J. Nucl. Mater.* 343 (2005) 123–133. doi:10.1016/j.jnucmat.2004.10.169.
- [69] F. Ernst, Y. Cao, G.M. Michal, Carbides in low-temperature-carburized stainless steels, *Acta Mater.* 52 (2004) 1469–1477. doi:10.1016/j.actamat.2003.11.027.
- [70] F. Ernst, Y. Cao, G.M. Michal, A.H. Heuer, Carbide precipitation in austenitic stainless steel carburized at low temperature, *Acta Mater.* 55 (2007) 1895–1906. doi:10.1016/j.actamat.2006.09.049.
- [71] Y. Cao, F. Ernst, G.M. Michal, Colossal carbon supersaturation in austenitic stainless steels carburized at low temperature, *Acta Mater.* 51 (2003) 4171–4181. doi:10.1016/S1359-6454(03)00235-0.
- [72] G.M. Michal, F. Ernst, A.H. Heuer, Carbon paraequilibrium in austenitic stainless steel, *Metall. Mater. Trans. A.* 37 (2006) 1819–1824. doi:10.1007/s11661-006-0124-9.
- [73] J. Oddershede, T.L. Christiansen, K. Ståhl, M. a J. Somers, Extended X-ray absorption fine structure investigation of nitrogen stabilized expanded austenite, *Scr. Mater.* 62 (2010) 290–293. doi:10.1016/j.scriptamat.2009.11.021.
- [74] J. Oddershede, T.L. Christiansen, K. Ståhl, M. a J. Somers, Extended X-Ray absorption fine structure investigation of carbon stabilized expanded austenite and carbides in stainless steel AISI 316, *Steel Res. Int.* 82 (2011) 1248–1254. doi:10.1002/srin.201100113.
- [75] T. Christiansen, M. a J. Somers, Controlled dissolution of colossal quantities of nitrogen in stainless steel, *Metall. Mater. Trans. A.* 37 (2006) 675–682. doi:10.1007/s11661-006-

- 0039-5.
- [76] T.S. Hummelshøj, T.L. Christiansen, M. a J. Somers, Lattice expansion of carbon-stabilized expanded austenite, *Scr. Mater.* 63 (2010) 761–763. doi:10.1016/j.scriptamat.2010.05.031.
 - [77] T.L. Christiansen, M.A.J. Somers, Stress and Composition of Carbon Stabilized Expanded Austenite on Stainless Steel, *Metall. Mater. Trans. a-Physical Metall. Mater. Sci.* 40A (2009) 1791–1798. doi:10.1007/s11661-008-9717-9.
 - [78] S. Jegou, T.L. Christiansen, M. Klaus, C. Genzel, M. a J. Somers, Determination of composition, residual stress and stacking fault depth profiles in expanded austenite with energy-dispersive diffraction, *Thin Solid Films.* 530 (2013) 71–76. doi:10.1016/j.tsf.2012.06.029.
 - [79] J. Liu, P. Han, M. Dong, G. Fan, G. Qiao, J. Yang, Influence of Ni and N on generalized stacking-fault energies in FeCrNi alloy: A first principle study, *Phys. B Condens. Matter.* 407 (2012) 891–895. doi:10.1016/j.physb.2011.12.111.
 - [80] D.L. Williamson, O. Ozturk, R. Wei, P.J. Wilbur, Metastable phase formation and enhanced diffusion in f.c.c. alloys under high dose, high flux nitrogen implantation at high and low ion energies, *Surf. Coatings Technol.* 65 (1994) 15–23. doi:10.1016/S0257-8972(94)80003-0.
 - [81] S. Parascandola, W. Möller, D.L. Williamson, The nitrogen transport in austenitic stainless steel at moderate temperatures, *Appl. Phys. Lett.* 76 (2000) 2194. doi:10.1063/1.126294.
 - [82] C. Blawert, B.L. Mordike, G.A. Collins, K.T. Short, Y. Jiraskova, O. Schneeweiss, V. Perina, Characterisation of duplex layer structures produced by simultaneous implantation of nitrogen and carbon into austenitic stainless steel X5CrNi189, *Surf. Coatings Technol.* 128–129 (2000) 219–225.
 - [83] W. Möller, S. Parascandola, T. Telbizova, R. Günzel, E. Richter, Surface processes and diffusion mechanisms of ion nitriding of stainless steel and aluminum, *Surf. Coatings Technol.* 136 (2001) 73–79. doi:10.1016/S0257-8972(00)01015-X.
 - [84] T.L. Christiansen, M. a J. Somers, Determination of the concentration dependent diffusion coefficient of nitrogen in expanded austenite, *Int. J. Mater. Res.* 99 (2008) 999–1005. doi:10.3139/146.101729.
 - [85] T. Moskalioviene, A. Galdikas, Stress induced and concentration dependent diffusion of nitrogen in plasma nitrided austenitic stainless steel, *Vacuum.* 86 (2012) 1552–1557. doi:10.1016/j.vacuum.2012.03.026.
 - [86] G. Ubertalli, G.M.M. Mortarino, F. Rosalbino, D. Firrao, Indurimento superficiale di acciai inossidabili austenitici mediante tin-pvd e kolsterizzazione e loro caratterizzazione, *La Metall. Ital.* 100 (2008) 15–20.
 - [87] M. Tsujikawa, S. Noguchi, N. Yamauchi, N. Ueda, T. Sone, Effect of molybdenum on hardness of low-temperature plasma carburized austenitic stainless steel, *Surf. Coatings Technol.* 201 (2007) 5102–5107. doi:10.1016/j.surfcoat.2006.07.127.
 - [88] W. Li, X. Li, H. Dong, Effect of tensile stress on the formation of S-phase during low-temperature plasma carburizing of 316L foil, *Acta Mater.* 59 (2011) 5765–5774. doi:10.1016/j.actamat.2011.05.053.
 - [89] J. Baranowska, K. Szczeciński, M. Wysiecki, Increasing of gas nitriding kinetics via surface pre-treatment, *Surf. Coatings Technol.* 151–152 (2002) 534–539. doi:10.1016/S0257-8972(01)01598-5.
 - [90] a. N. Allenstein, C.M. Lepienski, a. J. a. Buschinelli, S.F. Brunatto, Plasma nitriding using high H₂ content gas mixtures for a cavitation erosion resistant steel, *Appl. Surf. Sci.* 277 (2013) 15–24. doi:10.1016/j.apsusc.2013.03.055.
 - [91] C. Tromas, J.C. Stinville, C. Templier, P. Villechaise, Hardness and elastic modulus

- gradients in plasma-nitrided 316L polycrystalline stainless steel investigated by nanoindentation tomography, *Acta Mater.* 60 (2012) 1965–1973. doi:10.1016/j.actamat.2011.12.012.
- [92] B. Sartowska, J. Piekoszewski, L. Waliś, J. Stanisławski, L. Nowicki, R. Ratajczak, M. Kopcewicz, J. Senatorski, Thermal stability of the phases formed in the near surface layers of unalloyed steels by nitrogen pulsed plasma treatment, *Vacuum.* 81 (2007) 1188–1190. doi:10.1016/j.vacuum.2007.01.013.
- [93] X.Y. Li, S. Thaiwatthana, H. Dong, T. Bell, Thermal Stability of Carbon S Phase in 316 Stainless Steel, *Surf. Eng.* 18 (2002) 448–452. doi:doi 10.1179/026708402225006259.
- [94] L. Wang, Y. Li, Y.Z. Wang, Thermal Stability of Nitrogen Expanded Austenite Formed by Plasma Nitriding on AISI304 Austenitic Stainless Steels, *Key Eng. Mater.* 373–374 (2008) 308–311. doi:10.4028/www.scientific.net/KEM.373-374.308.
- [95] L. Nosei, M. Avalos, B.J. Gómez, L. Nachez, J. Feugeas, Stability under temperature of expanded austenite developed on stainless steel AISI 316L by ion nitriding, *Thin Solid Films.* 468 (2004) 134–141. doi:10.1016/j.tsf.2004.06.094.
- [96] T. Christiansen, M. a J. Somers, Decomposition kinetics of expanded austenite with high nitrogen contents, *Int. J. Mater. Res.* 97 (2006) 79–88.
- [97] S. Thaiwatthana, X.Y. Li, H. Dong, T. Bell, Comparison studies on properties of nitrogen and carbon S phase on low temperature plasma alloyed AISI 316 stainless steel, *Surf. Eng.* 18 (2002) 433–437. doi:10.1179/026708402225010083.
- [98] O. Celik, M. Baydogan, E. Atar, E.S. Kayali, H. Cimenoglu, Materials Science & Engineering A Fatigue performance of low temperature nitrided AISI 321 grade austenitic stainless steel, *Mater. Sci. Eng. A.* 565 (2013) 38–43. doi:10.1016/j.msea.2012.11.122.
- [99] K.S. Wang, H.L. Che, M.K. Lei, Corrosion-fatigue properties of plasma-based low-energy nitrogen ion implanted AISI 304 L austenitic stainless steel in borate buffer solution, *Surf. Coatings Technol.* 288 (2016) 30–35. doi:10.1016/j.surfcoat.2016.01.010.
- [100] K. Tokaji, K. Kohyama, M. Akita, Fatigue behaviour and fracture mechanism of a 316 stainless steel hardened by carburizing, *Int. J. Fatigue.* 26 (2004) 543–551. doi:10.1016/j.ijfatigue.2003.08.024.
- [101] M.K. Lei, X.M. Zhu, Plasma-based low-energy ion implantation of austenitic stainless steel for improvement in wear and corrosion resistance, *Surf. Coatings Technol.* 193 (2005) 22–28. doi:10.1016/j.surfcoat.2004.08.139.
- [102] Y. Sun, T. Bell, Dry sliding wear resistance of low temperature plasma carburised austenitic stainless steel, *Wear.* 253 (2002) 689–693. doi:10.1016/S0043-1648(02)00170-9.
- [103] Y. Sun, T. Bell, Effect of layer thickness on the rolling-sliding wear behavior of low-temperature plasma-carburized austenitic stainless steel, *Tribol. Lett.* 13 (2002) 29–34.
- [104] Y. Zhao, B. Yu, L. Dong, H. Du, J. Xiao, Low-pressure arc plasma-assisted nitriding of AISI 304 stainless steel, *Surf. Coatings Technol.* 210 (2012) 90–96. doi:10.1016/j.surfcoat.2012.08.070.
- [105] E. Menthe, K.-T. Rie, J.W. Schultze, S. Simson, Structure and properties of plasma-nitrided stainless steel, *Surf. Coatings Technol.* 74–75 (1995) 412–416. doi:10.1016/0257-8972(95)08246-8.
- [106] L. Ceschini, C. Chiavari, E. Lanzoni, C. Martini, Low-temperature carburised AISI 316L austenitic stainless steel: Wear and corrosion behaviour, *Mater. Des.* 38 (2012) 154–160. doi:10.1016/j.matdes.2012.02.019.
- [107] J.P. Lebrun, Applications of low-temperature surface hardening of stainless steels, in: *Thermochem. Surf. Eng. Steels*, Woodhead Publishing Limited, 2015: pp. 633–647. doi:10.1533/9780857096524.4.633.

- [108] S. Collins, P. Williams, Low-Temperature Colossal Supersaturation, *Adv. Mater. Process.* (2006) 32–33.
- [109] J. Buhagiar, L. Qian, H. Dong, Surface property enhancement of Ni-free medical grade austenitic stainless steel by low-temperature plasma carburising, *Surf. Coatings Technol.* 205 (2010) 388–395. doi:10.1016/j.surfcoat.2010.06.062.
- [110] J. Buhagiar, X. Li, H. Dong, Formation and microstructural characterisation of S-phase layers in Ni-free austenitic stainless steels by low-temperature plasma surface alloying, *Surf. Coatings Technol.* 204 (2009) 330–335. doi:10.1016/j.surfcoat.2009.07.030.
- [111] EUROPEAN STANDARD BS EN 10088 2:2005. Stainless steels - Part 2 : Technical delivery conditions for sheet / plate and strip of corrosion resisting steels for general purposes, 2005.
- [112] J. Goldstein, D. Newbury, D. Joy, C. Lyman, P. Echlin, E. Lifshin, L. Sawyer, J. Michael, *Scanning Electron Microscopy and X-ray Microanalysis*, 2003.
- [113] T. Maitland, S. Sitzman, EBSD Technique and Materials Characterization Examples, in: W. Zhou, Z.L. Wang (Eds.), *Scanning Microsc. Nanotechnol.*, 2007: pp. 41–76.
- [114] S.I. Wright, M.M. Nowell, D.P. Field, A Review of Strain Analysis Using Electron Backscatter Diffraction, *Microsc. Microanal.* 17 (2011) 316–329. doi:10.1017/S1431927611000055.
- [115] T.B. Britton, J. Jiang, Y. Guo, A. Vilalta-Clemente, D. Wallis, L.N. Hansen, A. Winkelmann, A.J. Wilkinson, Tutorial: Crystal orientations and EBSD - Or which way is up?, *Mater. Charact.* 117 (2016) 113–126. doi:10.1016/j.matchar.2016.04.008.
- [116] A. Kelly, G.W. Groves, P. Kidd, *Crystallography and Crystal Defects*, 2. Ed., Wiley, New York, 2000.
- [117] D. Briggs, M.P. Seah, *Practical surface analysis. Vol. 1, Auger and X-ray photoelectron spectroscopy*, 2. ed., Wiley, Frankfurt am Main, 1990.
- [118] I. Tilinin, A. Jablonski, W.S.M. Werner, Quantitative surface analysis by Auger and x-ray photoelectron spectroscopy, *Prog. Surf. Sci.* 52 (1996) 193–335. doi:10.1016/0079-6816(96)00008-1.
- [119] J.F. Watts, J. Wolstenholme, *An Introduction to Surface Analysis by XPS and AES*, John Wiley & Sons, Ltd, Chichester, UK, 2003. doi:10.1002/0470867930.
- [120] S. Karimi, N. Fraser, B. Roberts, F.R. Foulkes, A review of metallic bipolar plates for proton exchange membrane fuel cells: Materials and fabrication methods, *Adv. Mater. Sci. Eng.* 2012 (2012). doi:10.1155/2012/828070.
- [121] H. Wang, M.A. Sweikart, J.A. Turner, Stainless steel as bipolar plate material for polymer electrolyte membrane fuel cells, *J. Power Sources.* 115 (2003) 243–251. doi:10.1016/S0378-7753(03)00023-5.
- [122] S. Kante, Low-temperature carburizing of austenitic stainless steels - Characterization of carbon supersaturated SS2343, 254SMO and 353MA - Expanded austenite, Chalmers University of Technology, 2016.
- [123] M. Tsujikawa, M. Egawa, N. Ueda, A. Okamoto, T. Sone, K. Nakata, Effect of molybdenum and copper on S-phase layer thickness of low-temperature carburized austenitic stainless steel, *Surf. Coatings Technol.* 202 (2008) 5488–5492. doi:10.1016/j.surfcoat.2008.06.096.
- [124] K.H. Jack, The Iron-Nitrogen System: the Preparation and the Crystal Structures of Nitrogen-austenite (γ) and Nitrogen-martensite (α'), *Proc. R. Soc. A.* 208 (1951) 200–215. doi:10.1098/rspa.1951.0154.
- [125] P.G. Ranaware, M.J. Rathod, Synergetic effect of thicker nanocrystalline structure with high amount of strain induced martensite on surface characteristics of plasma nitrided austenitic stainless steel, *Surf. Coatings Technol.* 302 (2016) 265–274. doi:10.1016/j.surfcoat.2016.05.085.

- [126] J.. Riviere, P. Meheust, J.. Villain, C. Templier, M. Cahoreau, G. Abrasonis, L. Pranevicius, High current density nitrogen implantation of an austenitic stainless steel, *Surf. Coatings Technol.* 158–159 (2002) 99–104. doi:10.1016/S0257-8972(02)00227-X.
- [127] H.E. Du Plessis, The crystal structures of the iron carbides, University of the Free State (South Africa), 2006.
- [128] T.L. Christiansen, K. Ståhl, B.K. Brink, M.A.J. Somers, On the Carbon Solubility in Expanded Austenite and Formation of Hägg Carbide in AISI 316 Stainless Steel, *Steel Res. Int.* 87 (2016) 1–11. doi:10.1002/srin.201500415.
- [129] F. Ernst, D. Li, H. Kahn, G.M. Michal, A.H. Heuer, The carbide M7C3 in low-temperature-carburized austenitic stainless steel, *Acta Mater.* 59 (2011) 2268–2276. doi:10.1016/j.actamat.2010.11.058.
- [130] Y. Peng, J. Gong, Y. Jiang, M. Fu, D. Rong, The effect of plastic pre-strain on low-temperature surface carburization of AISI 304 austenitic stainless steel, *Surf. Coatings Technol.* 304 (2016) 16–22. doi:10.1016/j.surfcoat.2016.05.047.
- [131] H. Ferkel, M. Glatzer, Y. Estrin, R.Z. Valiev, RF plasma nitriding of a severely deformed high alloyed steel, *Scr. Mater.* 46 (2002) 623–628. doi:10.1016/S1359-6462(02)00031-3.
- [132] F. Bottoli, T.L. Christiansen, G. Winther, M.A.J. Somers, Effect of Plastic Pre-straining on Residual Stress and Composition Profiles in Low-Temperature Surface-Hardened Austenitic Stainless Steel, *Metall. Mater. Trans. A.* 47 (2016) 4001–4011. doi:10.1007/s11661-016-3586-4.
- [133] H. Kahn, G.M. Michal, F. Ernst, a. H. Heuer, Poisson Effects on X-Ray Diffraction Patterns in Low-Temperature-Carburized Austenitic Stainless Steel, *Metall. Mater. Trans. A.* 40 (2009) 1799–1804. doi:10.1007/s11661-009-9814-4.
- [134] P.D. Southwick, R.W.K. Honeycombe, Precipitation of M₂₃C₆ at austenite/ferrite interfaces in duplex stainless steel, *Met. Sci.* 16 (1982) 475–482. doi:10.1179/msc.1982.16.10.475.
- [135] H.U. Hong, B.S. Rho, S.W. Nam, Correlation of the M₂₃C₆ precipitation morphology with grain boundary characteristics in austenitic stainless steel, *Mater. Sci. Eng. A.* 318 (2001) 285–292. doi:10.1016/S0921-5093(01)01254-0.
- [136] J. Wang, Z. Li, D. Wang, S. Qiu, F. Ernst, Thermal stability of low-temperature-carburized austenitic stainless steel, *Acta Mater.* 128 (2017) 235–240. doi:10.1016/j.actamat.2017.02.018.
- [137] U.S. Doe, Fuel cell technologies office multi-year research, development and demonstration plan, 2016. https://energy.gov/sites/prod/files/2017/05/f34/fcto_myrrdd_fuel_cells.pdf.